Nanostructured Complex Light Metal Hydrides Based on Li, Na, B, N and Al for Solid State Hydrogen Storage

by

Roozbeh Parviz

A thesis

presented to the University of Waterloo

in fulfilment of the

thesis requirement for the degree of

Doctor of Philosophy

in

Mechanical Engineering

Waterloo, Ontario, Canada, 2013

© Roozbeh Parviz 2013

Author's Declaration

I hereby declare that I am the sole author of this thesis. This is a true copy of the thesis, including any required final revisions, as accepted by my examiners.

I understand that my thesis may be made electronically available to the public

Abstract

The present work reports a study of the effects of the compositions, and various catalytic additives and nanostructuring by high-energy ball milling, on the hydrogen storage properties of $LiBH_4$, $NaBH_4$, $LiNH_2$ and $LiAlH_4$ complex hydrides and their composites. The hydrides have been systematically investigated using X-ray diffraction (XRD), Fourier transform infrared spectroscopy (FTIR), scanning electron microscopy (SEM), differential scanning calorimetry (DSC) and a Sieverts-type apparatus.

The composites of ($NaBH_4$+2$Mg(OH)_2$) and ($LiBH_4$+2$Mg(OH)_2$) without and with nanometric nickel (n-Ni) added as a potential catalyst were synthesized by high energy ball milling. The ball milled $NaBH_4$-based composite desorbs hydrogen in one exothermic reaction in contrast to its $LiBH_4$-based counterpart, which dehydrogenates in two reactions: an exothermic and endothermic. XRD phase studies after volumetric isothermal dehydrogenation tests show the presence of $NaBO_2$ and MgO for the $NaBH_4$-based composite. For the $LiBH_4$- based composite the phases such as MgO, Li_3BO_3, MgB_2, MgB_6 are the products of the first exothermic reaction, which has a theoretical H_2 capacity of 8.1 wt.%. However, for reasons that are not quite clear, the first reaction never goes to full completion even at 300°C desorbing ~ 4.5 wt.% H_2 at this temperature. The products of the second endothermic reaction for the $LiBH_4$-based composite are MgO, MgB_6, B and $LiMgBO_3$ and the reaction has a theoretical H_2 capacity of 2.26 wt.%. The effect of the addition of 5 wt.% nanometric Ni on the dehydrogenation behavior of both the $NaBH_4$-and $LiBH_4$-based composites is rather

negligible. The n-Ni additive may not be the optimal catalyst for these hydride composite systems although more tests are required since only one n-Ni content was examined.

In the ($LiNH_2$+$nMgH_2$) system, the phase transformations occurring as a function of the ball milling energy injected into the hydride system ($LiNH_2$+$nMgH_2$), having molar ratios n=0.5 to 2.0, have been thoroughly studied. The milling energy in a magneto-mill is estimated by a semi-empirical method. X-ray diffraction (XRD) and Fourier Transform Infrared (FTIR) measurements show that for the molar ratios n<1.0 three new phases such as LiH, amorphous $Mg(NH_2)_2$ (a-$Mg(NH_2)_2$) and $Li_2Mg(NH)_2$ are formed during ball milling depending on the injected quantity of milling energy. Hydrogen is not released during milling when the LiH and a-$Mg(NH_2)_2$ hydrides are being formed whereas the formation of the $Li_2Mg(NH)_2$ hydride phase is always accompanied by a profound release of hydrogen. For the molar ratios n≥1.0 the new phase of MgNH forms whose formation is accompanied by a profound release of hydrogen. Based on the experimental data we established an approximate hydride phase-injected milling energy diagram for various levels of injected milling energy and the molar ratios. Addition of 5 %wt. KH can improve desorption rate of the $LiNH_2$+0.5 MgH_2 system. Furthermore this hydride system can be nearly fully rehydrogenated at 200°C and 50 bar H_2 pressure.

$LiAlH_4$ containing 5 wt.% of nanometric Fe (n-Fe) shows a profound mechanical dehydrogenation by continuously desorbing hydrogen (H_2) during high energy ball milling. In contrast, no H_2 desorption is observed during low energy milling of $LiAlH_4$

containing n-Fe and the system with micrometric Fe (m-Fe). X-ray diffraction studies show that ball milling results in a varying degree of the lattice expansion of $LiAlH_4$. A volumetric lattice expansion larger than 1% results in the profound destabilization of lattice. The Fe and Ni ions dissolve in the lattice, replacing the Al ions and forming a substitutional solid solution. The quantity of dissolved metal ions depends primarily on the total energy of milling per unit mass of powder generated within a prescribed milling time, the type of additive ion e.g. Fe vs. Ni and on the particle size (micrometric vs. nanometric) of metal additive.

Both Fe and Ni decrease the apparent activation energies of stage I $\rightarrow$ and II $\rightarrow$, but stage I is more sensitive to the particle size of additives. Ball milled ($LiAlH_4$+5 wt.% n-Fe) slowly self-discharges during storage at room temperature (RT), 40 and 80ºC. Fully dehydrogenated ($LiAlH_4$+5 wt.% n-Fe) can be partially rehydrogenated, however, the rehydrogenation parameters are not optimized yet.

The influence of the addition of 5 wt.% nano-size "interstitial compound" (n-TiC, n-TiN and n-ZrC) on stability and the dehydrogenation properties of $LiAlH_4$ were also investigated. A continuous desorption of H_2 is observed during high energy milling. Mechanical dehydrogenation rate of the doped samples increases noticeably during high-energy ball milling in the order of TiN > TiC > ZrC. XRD shows that a gradual decomposition of $LiAlH_4$ to Li_3AlH_6 and Al (Stage I) occurs during high energy milling of nanocomposites. The interstitial compound additives are able to strongly reduce the apparent activation energy of Stage II dehydrogenation (63-80 kJ/mol) but do not

substantially affect the apparent activation energy of Stage I (87-96 kJ/mol). These systems are also able to self-discharge slowly large quantities of H_2 during storage at 40ºC.

Acknowledgements

I would like to express my sincere gratitude to my supervisors, Prof. R. A. Varin and for his guidance, tireless support and continual encouragement throughout this work. I would also like to thank Prof. J. Huot, Prof. E. Croiset, Prof. M. Mayer and Prof. J. Wen for their constructive criticism.

Dedication

I would like to dedicate this work to my parents and my love, Maryam, whose unending supports and encouragements during my graduate study. There is no doubt in my mind that without their love and support I could complete this process.

Table of Contents

List of Tables

List of Figures

1. Introduction

The current interest in hydrogen is primarily due to environmental concerns about harmful emissions from the widespread use of fossil fuels [1]. Today, approximately 87% of worldwide energy use is in the form of fossil fuels, which are responsible for 57% of the annual global carbon dioxide emissions [2]. Since fossil fuels are not renewable, and are rapidly being depleted, many industrial, governmental and scientific groups believe that hydrogen's physical and chemical advantages will make it an important synthetic fuel in the future (Table 1.1) [3].

Table 1.1 Physical and chemical properties of hydrogen, methanol and gasoline [3].

Properties	**Hydrogen (H_2)**	**Methanol (CH_4)**	**Gasoline (-CH2-)**
Lower heating value (kWh kg^{-1})	33.33	13.9	12.4
Self-ignition temperature (°C)	585	540	228-501
Flame temperature(°C)	2045	1875	2200
Ignition Limits in air (Vol%)	4-75	5.3-15	1.0-7.6
Minimal ignition energy (mWs)	0.02	0.29	0.24
Flame propagation in air (ms^{-1})	2.65	0.4	0.4
Diffusion coefficient in air (cm^2s^{-1})	0.61	0.16	0.05
Toxicity	No	No	High

Hydrogen is an attractive option, as the chemical energy per mass of hydrogen (142 MJ/kg) is at least three times larger than that of other chemical fuels (for example, the equivalent value for liquid hydrocarbons is 47 MJ/kg) [3]. Another advantage of turning to hydrogen fuel as an alternative energy source is that when it burns with oxygen from air—whether in an external combustion engine or in a fuel cell—the oxidation product is only water according to the following reaction:

$$H_2+½O_2 \rightarrow H_2O + \text{Heat} \qquad (1.1)$$

While hydrogen has many obvious advantages, there remains a problem with safe storage and transportation [1].

1.1. Hydrogen Storage Methods

In order for there to be a transition from a fossil fuel to a hydrogen-based economy, hydrogen storage is a key issue that must be solved. Since the volumetric density at standard conditions is very low, one needs to pack the hydrogen as close as possible. To achieve this goal, additional materials and energy are required since hydrogen is merely an energy carrier [4]. Hydrogen can be stored as: (i) pressurized gas, (ii) cryogenic liquid, and (iii) solid fuel in a chemical or physical combination with materials, such as metal hydrides, complex hydrides and carbon materials (see Table 1.2) [5].

With the newly developed light weight composite cylinders that support pressure up to 80 MPa, hydrogen volumetric density can reach 30-40 kg m^{-3} [3]. However, there remains a safety concern in respect to the proper use of these pressurized cylinders,

especially in high population regions [5]. As well, the expensive cost of pressurization is another issue that needs addressing.

Table 1.2 Comparison of the major hydrogen storage methods [3].

Storage system	**Volumetric density (kg H_2 m^{-3})**	**Drawbacks**
Compressed hydrogen gas under 80 MPa pressure	~30-40	Safety problems (enormous pressures required)
Liquid hydrogen at cryogenic tank at -252°C (21K):	~71	Large thermal losses (open system)
Solid metal/intermetallic hydrides	~80-150	None of above two

Liquid hydrogen is stored in cryogenic tanks at -252°C and ambient pressure. The volumetric density of liquid hydrogen is ~71 kg m^{-3} [3]. Due to the low critical temperature of hydrogen (-241°C [3]; hydrogen is gaseous above this temperature), liquid hydrogen can only be stored in open systems to prevent strong overpressure. In this system of storage, thermal loss is still a concern. The cost of liquification is about 50% of the liquid H_2.

Solid state hydrides, which include metal / intermetallic and complex hydrides, are characterized by their highest volumetric capacities (~80-150 kg m^{-3} [3]) and they do not suffer the same drawbacks as those experienced by compressed and liquid hydrogen. Because of the low pressures involved in metal hydride technologies, and the fact that the release of hydrogen takes place, in a number of hydrides, via an endothermic process, this method of hydrogen storage is the safest of the three options. Moreover, the hydrogen released from a metal hydride is of very high purity

and, therefore, can be used directly to feed a PEM fuel cell [6]. However, there are two main constrains for using solid-state hydrides in stationary and mobile applications.

The first constraint is related to the technical specifications for a certain type of fuel cell. High-power density proton exchange membrane fuel cell (PEMFC) is the most common type of fuel cells, which is proper for most of the applications such as automotive, portable electronic devices, stationary auxiliary power systems, off-road vehicles etc [6]. The operation condition of these fuel cells are constrained to 1bar pressure and less than 100ºC temperature. These technical specifications require that the suitable hydrogen storage material must desorb hydrogen in an H_2 pressure of 1 bar and exhibit desorption temperature at that pressure not higher than 100ºC.

The second constraint is man-made and depends on the required travel distance for hydrogen-fuelled transportation vehicles. The US Department of Energy (DOE) requires a distance of 300 miles (480 km). Based on this, the US Department of Energy (DOE) introduced a number of long-term targets for automobile hydrogen-storage applications while considering the economic and environmental parameters for 2015. Some of these targets have been listed in Table 1.3 [4]. For commercial viability, the predicted minimum hydrogen-storage capacity should be 5.5 wt.% for the entire storage system, which includes storage medium, tank, and some auxiliary devices. This translates into roughly ~10-11 wt% H_2 capacity for the solid hydride-based storage material.

Table 1.3 DOE Hydrogen Storage System Targets (has been adopted from [4]).

Target	2015 (old)	2015 (new)	Ultimate (new)
System gravimetric density [wt.%]	9	5.5	7.5
System volumetric density [g/L]	81	40	70
System fill time for 5-kg fill [min]	2.5	3.3	2.5
System cost [$/kgH2] ($/kWhnet)	67	TBD	TBD
Operating tempreture range [°C]	**Approx. -20°C to 100°C**		

In summary, these two important constraints, technical and man-made, require the potential hydrogen storage material for fuelling a PEMFC in automotive to desorb at <100ºC under

1 bar H_2, have a minimum practical achievable capacity ~10 wt% H_2, exhibit reversibility under reasonable conditions of pressure/temperature, desorb/absorb rapidly, and be relatively inexpensive. It is to be pointed out that the storage materials for non-automotive /non-transportation application do not necessarily meet H_2 capacities exceeding 10wt.%

1.2. Solid state hydrides

1.2.1. Fundamental mechanisms of reactions

Hydrogen dissociation and its subsequent bond formation to form bulk hydrides provides the basis for a substantial number of hydrogen storage materials. Metal hydrides can be formed reversibly by direct interaction of metals/intermetallics with hydrogen at the appropriate temperature and pressure according to the general reaction [7]:

$$M\,(s) + xH_2\,(g) \rightarrow MHx(s)+Heat \qquad (1.2)$$

The reaction between the gas phase of H_2 and a metal surface can be depicted using a simple two-dimensional set of potential energy curves (see Fig. 1.1 [3,8]). The surface the two curves are separated by the dissociation energy of 218 kJ/mol H, which represents the amount of energy required to split H_2 into two hydrogen molecules. A hydrogen molecule moves towards the surface because of van der Waals attractive forces in the range of approx. 0-20 kJ/mol H_2 (molecular physisorption) (point 1 in Fig. 1.1). If the molecule moves closer to the surface, the potential energy will increase due to repulsion. At some point, the potential energy of the H_2 molecule will intersect with the potential energy of the H atom. After this happens, it is energetically more favourable for the two H atoms to be separated and bonded to the metal surface rather than bonded to each other. Hence dissociation will occur in this process.

If the potential energy curves intersect above the zero energy level, positive activation energy is required for hydrogen dissociation (activated dissociation- point 2). If the intersection is located at approximately zero potential energy (non-

activated- dissociation-point 3), however, dissociation is energetically favourable and occurs spontaneously. The height of intersection points determines the activation barrier and only the fraction of H_2 molecules with energy larger than the activation barrier will be able to dissociate. After dissociation, the potential energy of hydrogen in the material reaches its minimum value, which corresponds to the H atoms being bonded to the metal surface (heat of chemisorption, $E_C \approx$ 50kJ/molH). If the H-M bond is stronger than the H-H bond, chemisorption is said to be exothermic. Likewise, if the H-H bond is the strongest, chemisorption is said to be endothermic [3,8].

Figure 1.2 schematically shows the mechanism of metal hydride formation. The formation of the metal hydride can be divided into the following steps [9,10]:

Dissociation/adsorption: The first step is the dissociative adsorption of hydrogen on the metal/hydride surface. This is shown as point 1 in Fig. 1.2.

Surface penetration: From the surface, the hydrogen atoms can penetrate into the subsurface (point 3).

Bulk diffusion: From the sub-surface, the hydrogen atoms can diffuse into the bulk or from the bulk and further inwards (point 4).

Hydride formation: Hydrogen atoms in the bulk (corresponding to a solid solution) can create a hydride nuclei that can grow to larger hydride grains by trapping of additional 8 hydrogen atoms (point 6). The formation of a hydride phase complicates the picture slightly, as hydrogen diffusion can also take place through the hydride (point 5). For dehydrogenation, the process is the reverse.

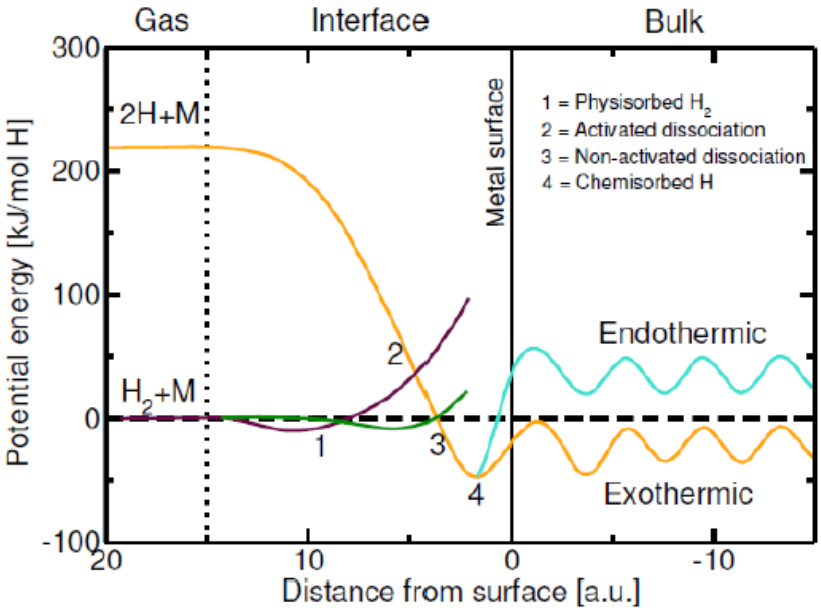

Fig. 1.1 Potential energy curves for activated or non-activated dissociation and chemisorption of hydrogen on a metal surface, followed by the endothermic or exothermic solution of atomic hydrogen into the bulk [3,8].

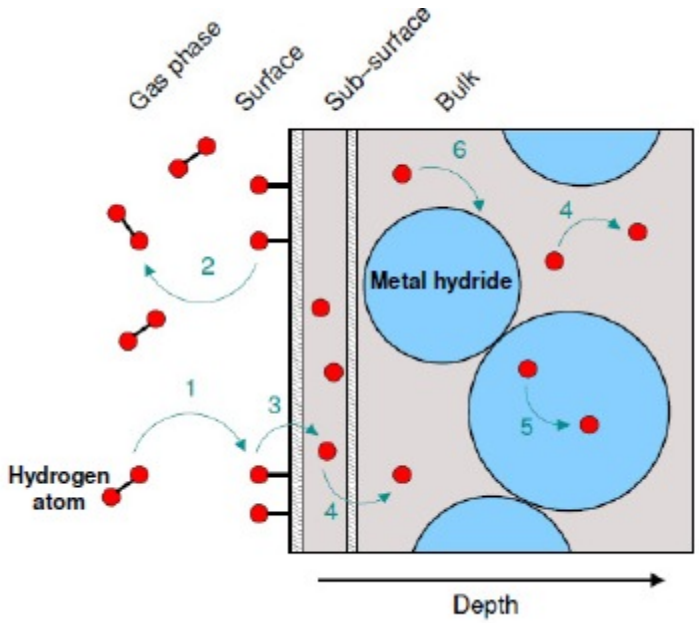

Fig.1.2 Schematic illustration of the different mechanisms involved in the formation of a metal hydride [9,10].

1.2.2.Requirements for solid state hydrogen storage materials

Figure 1.3 illustrates the gravimetric and volumetric energy densities of hydrogen stored using various storage methods. Solid state hydrogen storage that uses ionic-covalent hydrides of light elements, such as lithium, boron, sodium, magnesium and aluminum (or some combination of these elements), is becoming increasingly accepted as the only method that achieves the necessary gravimetric and volumetric target densities.

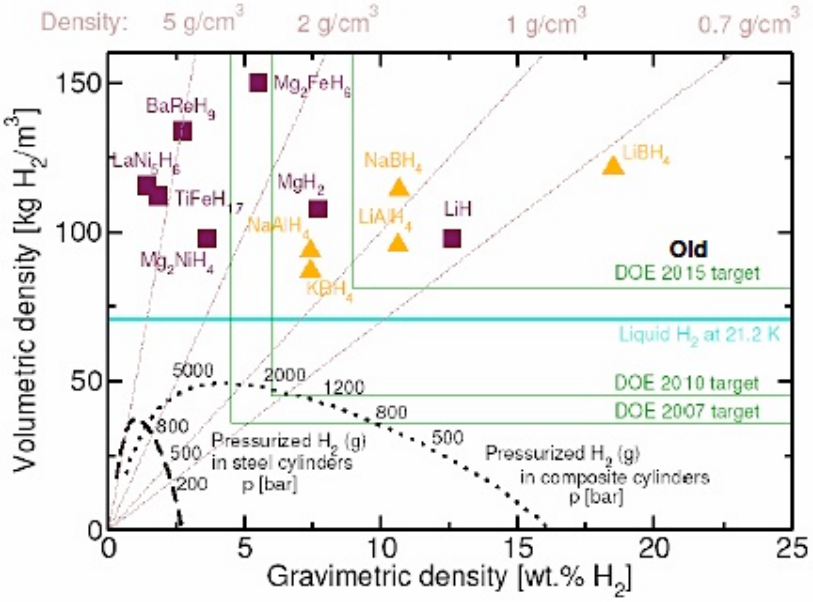

Fig.1.3 Volumetric and gravimetric hydrogen storage densities of different hydrogen storage methods [6].

Although these compounds demonstrate a good capacity, there are still some problems to be solved. The chemical bonds in light-element based hydrides are predominately covalent or ionic, causing unacceptably high thermodynamic stability and, consequently, low equilibrium hydrogen pressures. In addition, the high directionality of the covalent/ionic bonds in these systems leads to the large activation barriers for atomic motion that result in slow hydrogen sorption kinetics and

limited reversibility [12]. Furthermore, hydrogen storage in metal hydrides requires that the alloys exhibit reversibility of hydride formation and decomposition under practical conditions.

1.2.2.1. Kinetics

In order to provide a scientific foundation for the improvement of reaction kinetics, it is important to understand the reaction mechanism and the rate-limiting steps for hydrides [13]. It was reported that the rate of absorption is controlled by the following factors: (1) the rate of hydrogen dissociation at the surface, (2) the capability of hydrogen to penetrate from the surface typically covered by an oxide layer into metal, and (3) the rate of hydrogen diffusion into the bulk metal and through the hydride already formed [5]. Based on these factors, there are two approaches being pursued to improve the reaction kinetics. The first approach involves alloying hydrogen storage materials with catalysts and/or other foreign substances. Catalysts help to provide active sites for the dissociation of hydrogen at the gas/material interface and allow for more rapid diffusion of atomic hydrogen into the bulk, which consequently decreases the activation energy of the dehydrogenation reaction. There is intensive research about finding a proper catalyst to enhance the hydriding / dehydriding properties of hydrogen. A common technique used to increase the efficiency of hydrogen dissociation at the surface of chemisorbing materials is doping with metal catalysts [8,14]. For example, hydrogen molecules have a strong affinity for nickel and readily dissociate and adsorb onto surface-layer nickel clusters [15]. Through the addition of 1 at% of nickel to magnesium, Holtz and Imam [16] achieved a 50% increase in hydrogen amount, a decrease in the temperature for the onset of

hydrogenation from 275 to 175°C, and a lowering of the dehydrogenation onset temperature from 350 to 275°C. A considerable number of investigations at the materials development and fundamental mechanism levels seek to maximize the ability of a material to dissociate hydrogen through doping and surface texturing [17,18]. Metal hydrides can also be blended together to manipulate the thermodynamic and kinetic properties of the base material.

The second approach is nanostructuring. Nanostructured and nanoscale materials strongly influence the thermodynamics and kinetics of hydrogen absorption and desorption by increasing the diffusion rate, as well as by decreasing the required diffusion length. Specially, in contrast to bulk materials, the nano-scale materials can offer several advantages for the physicochemical reactions, such as surface interactions, adsorption in addition to bulk absorption, rapid kinetics, low temperature desorption, hydrogen atom dissociation, and molecular diffusion via the surface [19,20]. Section 4 discusses this approach in more detail.

1.2.2.2. Thermodynamics

The formation reactions of number of metal hydrides are exothermic and somewhat stable when below their dissociation temperatures. This means that, under suitable activation conditions, the formation reaction will be spontaneous, and the hydrogen will be stored within the material until a certain desorption temperature is reached [8]. Hydrogen absorption in metal hydrides may include a multiple-step mechanism. At first, molecular H_2 dissociate at the surface and then atomic hydrogen diffuses into the crystal metal lattice. At a certain hydrogen pressure, the host metal initially dissolves some hydrogen atoms (<0.3 wt.%) as a solid solution (α phase) and, as the

hydrogen concentration increases and the pressure rises, the metal hydride phase (β phase) nucleates and grows [6,21]. Fig 1.4 illustrates the sequential steps of hydride formation.

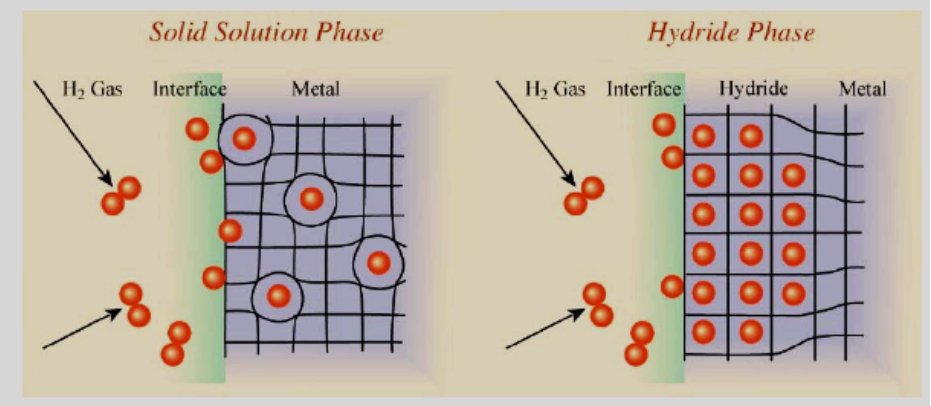

Fig.1.4 Potential energy curves for the activated or non-activated dissociation and chemisorption of hydrogen on a clean metal surface, followed by the endothermic or exothermic solution of atomic hydrogen into the bulk [8].

The thermodynamic conditions that a metal hydride can absorb and desorb hydrogen depend on its plateau pressure (or equilibrium pressure), which is determined by PCT (pressure-composition-temperature) curve (Fig. 1.5 a) [21].

In the plateau region there exists a mixture of α and β phases. The length of this region determines the reversible hydrogen capacity of the metal. Thus, by applying a pressure above the plateau pressure at a given temperature, hydrogen can be stored within the metal (hydriding reaction). Below the plateau pressure, the β phase is unstable and hydrogen can be released from the metal (dehydriding reaction). As it can be seen in Fig. 1.5a, increasing the temperature increases plateau pressure; beyond the critical temperature T_C, the plateau region disappears and the α phase converts to the β phase continuously [21].

The relation between plateau pressure P and temperature T is given by the well-known Van't Hoff equation:

$$\ln(P/Po) = -\Delta H/RT + \Delta S/R \quad (1.3)$$

Where P_o is atmospheric pressure, ΔH and ΔS are enthalpy and entropy changes of the hydriding / dehydriding reaction, respectively, T is the absolute temperature, and R is the gas constant. Since the entropy term corresponds mostly to the change from molecular hydrogen gas to dissolved atomic hydrogen, and is roughly similar for most metal-hydrogen systems (~130 kJ/mol K), the thermodynamic properties of metal-hydrogen systems are usually characterized by the strength of the metal-hydrogen bond and thus the enthalpy of the (de)hydriding reaction [6]. The enthalpy of absorption and desorption process, ΔH, can be determined from the slope of the Van't Hoff plot (ln P vs. 1/T) presented in Fig.1.5 b. For the practical use of hydrogen storage materials to assure dehydrogenation/rehydrogenation temperature lower than 100^{o}C, the metal-hydrogen bond strength should correspond to an enthalpy of around 30 - 50 kJ/mol H_2 [6].

Two primary advances are being used to address the thermodynamic limitations imposed by the high bond strengths in light-element based hydrides. The first focuses on the discovery of new single phase materials in which atomic substitution or alloying is used to decrease the thermodynamic stability. This work includes a wide range of ternary and quaternary compounds whose thermodynamic properties make them potentially acceptable as practical hydrogen storage media [22,23]. The

second approach utilizes existing binary and complex hydrides in combinations to form new compounds or alloys upon dehydrogenation [24]. This lowers the overall enthalpy for dehydrogenation, increases equilibrium hydrogen pressures, and effectively destabilizes the component hydrides. Although alloy formation in the dehydrogenated state can be used to reduce the overall reaction enthalpy, this approach does not solve the problems of slow hydrogen exchange kinetics in light-element based hydrides [22-24].

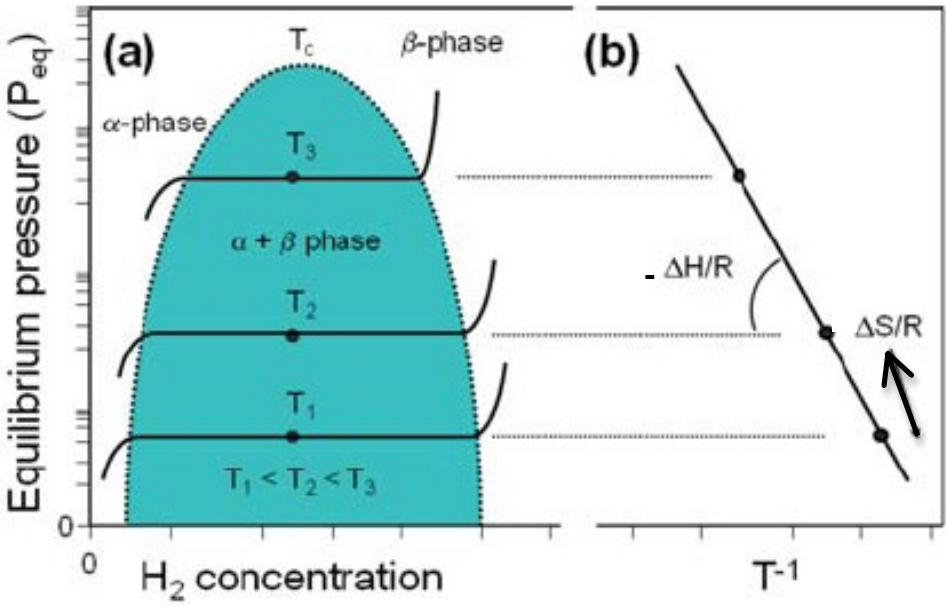

Fig.1.5 (a) Pressure composition isotherm (PCT) plot of hydrogen-metal systems, (b) van't Hoff plot related to the (de)hydriding reaction [21].

1.2.2.3. Reversibility

Among the known metal hydrides, because of high stability or instability of these materials, only a few show properties suitable for reversible hydrogen storage at moderately elevated temperature [13]. The rehydrogenation of stable metal hydrides,

such as LiH (which melts at 680°C but decomposes at 720°C), TiH_2, CaH_2, ZrH_2 or MgH_2 (which have to be heated up to 650, 600 and 880°C, respectively, in order to release hydrogen), is easy and they absorb hydrogen readily (even under low hydrogen pressures and at much lower temperatures than for desorption [13]).

On the other side, the group of unstable metal hydrides, such as $LiAlH_4$, readily decompose at low temperature (between 100 and 160°C) with relatively good kinetics. These hydrides have such a high pressure in equilibrium with the gas phase, however, they cannot, in practice, be formed from gaseous phase, and require a chemical reaction for their formation [1-3]. The same applies to other hydrides based on the AlH-complex, such as $LiAl_2H_7$, $NaAlH_4$, $Mg(AlH_4)$, $Be(AlH_4)$, $Zr(AlH_4)_2$, $Ca(AlH_4)_2$. All these hydrides offer very high gravimetric hydrogen capacities (between 5.6 and 12 wt.%) and easily desorb hydrogen at temperatures between 100°C and 180°C, but they normally cannot be rehydrogenated at hydrogen pressures lower than 100 atm [14,25]. Over the years, the search for practical metal hydrides has been focused on reducing the stability (i.e., on reducing desorption temperature) of stable metal hydrides such as MgH_2, or Mg_2NiH_4. Alternatively, un-stable metal hydrides could be modified in order to improve their absorption characteristics, which is the main difficulty preventing practical, reversible performance.

From a thermodynamics point of view, hydrogen generation can be endothermic or exothermic. Endothermic reactions are thermodynamically directly reversible if there is a sufficient hydrogen overpressure. These reactions are reversible because the reverse H_2 absorption reaction is exothermic and the heat released compensates for

the entropy loss; hence, the free energy gain that accompanies incorporation of H_2 into a condensed phase. Exothermic hydrogen-generating reactions are much more difficult to reverse [26]. Slightly exothermic reactions can be reversed by application of extreme hydrogen pressures that reduces the H_2 gas entropy. However, most exothermic reactions, in which hydrogen absorption is endothermic, are not directly reversible and require coupling to at least one additional exothermic reaction to compensate for the entropy loss. Although not directly reversible, exothermic reactions have been investigated for hydrogen-generating applications [26]. Despite the many surveys on solving this problem, the reversible solid start storage of hydrogen in hydrides remains one of the biggest challenges for widespread use of hydrogen as a fuel.

1.3. Nanostructuring

The nanostructuring process is one promising candidate of nano-technologies for application in hydrogen storage. Nanostructured materials are single/multi-phase polycrystals with grain crystallite sizes from a few nanometers to 100 nm [6,27]. Recently, researchers have focused on nanocrystalline materials, expecting to find applications based on their improved mechanical, magnetic, and other useful properties. Given that dehydriding and hydriding reactions are diffusion-controlled, it is fair to conclude that the effective methods for enhancing kinetics are those that can enhance the diffusion process [15]. Nano-engineering is one such process that can be used to reduce the diffusion distance and provide a new surface for reaction. This will increase the diffusion coefficient via doping or mechanical activation to introduce internal strains and vacancies, as well as micro-alloying to induce spallation

or extensive cracking of the reaction product layer [28-30].

It is believed that nanostructuring influences the thermodynamic as well as the kinetic properties of hydrogen storage materials. These effects have been assessed by theory, but are difficult to confirm by experiments due to the extremely small sizes required (sometimes smaller than 2 nm before significant effects are predicted) [8]. There are multiple mechanisms by which nanoscale can change the thermodynamics of hydrogen storage, such as increasing surface area and adding strain at grain boundaries. It was shown in section 1.2.2.1 that increasing grain boundaries do enhance the kinetics of hydrogen storage materials. When grain sizes reach the nanoscale, many theories predict that there can be some thermodynamic improvement as well. The strain present because of mismatched crystal orientation at the grain boundaries can lead to extra volume in the sample, which, in turn, creates excess energy in the material [31]. An alternative explanation is to treat the grain boundaries as an enhanced surface area [32]. To date, there is lack of experimental evidence, however, to support these concepts.

High-energy ball milling is the only nanotechnology top-down approach for the synthesis of both nanoparticles (increasing the surface area) and nanograins (increasing grain boundaries). It is a most interesting technique for improving diffusion-controlled reactions as it is a well-known method for making nanostructured particles and producing high defect concentrations such as: vacancies, dislocations, stacking faults besides the grain boundaries in solids [6]. The former reduces the diffusion distance, while the latter increases the diffusion coefficient [5,13,22]. Furthermore, these defects can raise the free energy of the system and make it

accessible to the formation of thermodynamically metastable phases. In addition, defects can lower the activation energy of reactions limited by poor kinetics [6]. There are many experiments that indicate the kinetics of both absorption and desorption can be improved by reducing the grain size of the compound [14]. For example Zaluska et al. [33] reported the improvement of the decomposition kinetics of $NaAlH_4$ by mechanical milling (as shown in Fig.1.6). Therefore, nanocrystalline materials have properties markedly different from their conventional crystalline counterparts and can be promising candidates for hydrogen storage in solid state hydrides.

High-energy ball milling is the only nanotechnology top-down approach for the synthesis of both nanoparticles (increasing the surface area) and nanograins (Increasing grain boundaries) and a most interesting technique for improving diffusion- controlled reactions because it is a well-known method for making nanostructured particles and producing high defect concentrations such as vacancies, dislocations, stacking faults besides the grains and grain boundaries in solids [6]. The former reduces the diffusion distance, while the latter increases the diffusion coefficient [5,13,22].

Furtheremore, these defects can raise the free energy of the system making it accessible to formation of thermodynamically metastable phases. Also, defects can lower the activation energy of reactions limited by poor kinetics [6]. There are many experiments indicate that the kinetics of both absorption and desorption can be improved by reducing the grain size of the compound [14].

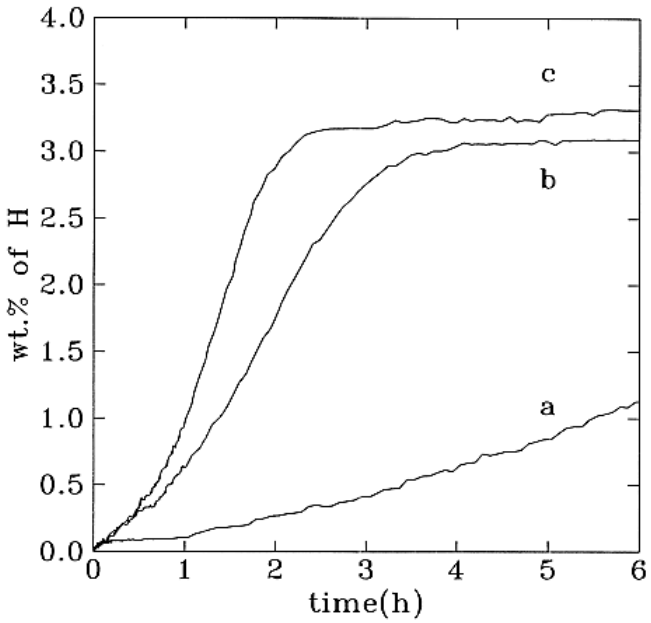

Fig. 1.6. Rates of decomposition (first hydrogen desorption) for $NaAlH_4$ ball-milled for various periods of time at: (a) 15 min (b) 1 h (c) 2 hdesorption at 1608C.[33].

There are many different designs of ball mills that can be used for the processing of advanced materials. In conventional ball mills (planetary or shakers), the trajectories of the grinding balls are rather chaotic (Fig. 1.7). This behaviour creates a continuous and erratic change of various mechanical modes of milling, from shearing to impact, during the same milling cycle. However, in the magneto-mill, Uni-Ball-Mill Model 5, the trajectories of the balls are controlled by the magnetic field created by strong FeNdB permanent magnet (Fig. 1.8). The milling mode can be then adjusted from shearing to impact by changing the angular position of the external magnets (as shown in Fig. 1.8).

Ball milling is a complex process that involves the optimization of milling parameters to achieve the desired product microstructure and properties. The important parameters are [6]:

(1) Milling mode

(2) Number of balls used for milling

(3) Milling speed

(4) Milling time

(5) Milling atmosphere

(6) Ball-to-powder-ratio

(7) Working distance (WD)

Note that the above process variables are not completely independent. For example, in Uni-Ball-Mill, the milling mode depends on the milling speed and working distance. Also, the milling time depends on the milling mode and ball-to-powder-ratio.

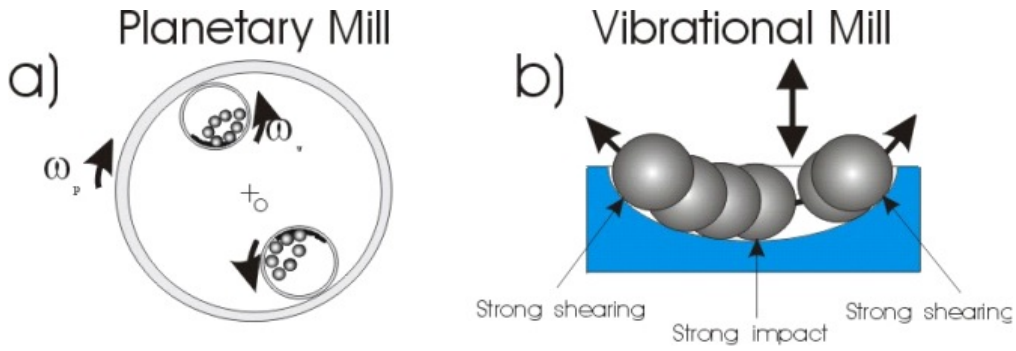

Fig.1.7 Motion of balls in (a) a planetary and (b) a vibrational mill [6].

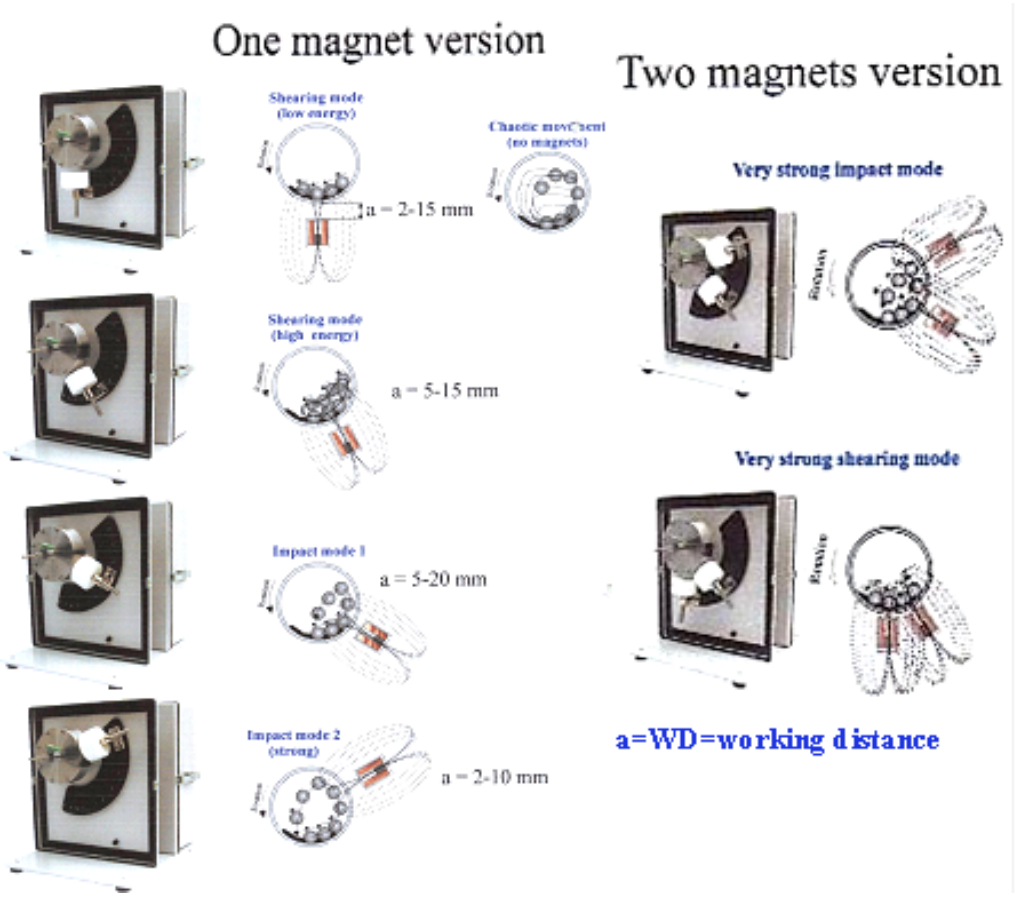

Fig.1.8 Various controlled modes of milling available in the Uni-Ball-Mill 5 [6].

1.4. Complex hydrides

There are three general types of metal hydrides: interstitial metal hydrides, covalent metal hydrides, and covalent complex metal hydrides. Interstitial metal hydrides are materials such as $LaNi_5Hx$, where hydrogen atoms are found in interstitial sites within the metal atom substructure. The hydrogen bonding is often complex, but relatively weak, involving multicenter bonding between hydrogen and the metal. Covalent metal hydrides are discrete compounds such as MgH_2, AlH_3, among others, where the bonding between hydrogen and metal is very covalent localized and strong.

Complex hydrides generally release and absorb hydrogen through bond-breaking decomposition and recombination reactions, as well as sometimes through discreet intermediate phases [11]. Complex covalent hydrides are compounds such as metal borohydrides, metal amides, and metal alanates, in which bonding between hydrogen and either B or N, etc., is highly covalent and strong. Due to the reversibility of interstitial metal hydrides and covalent complex metal hydrides, and to the high capacity of these hydrides, they have received the most research focus over the last few decades.

New directions in the research on materials for hydrogen storage have focused on low weight complex metal hydrides, such as alanates $[AlH_4]^-$, amides $[NH_2]^-$, imides and borohydrides $[BH_4]^-$, which are based on light weight elements such as Li, Na, B, Al and Mg. They are of interest because of their high volumetric and gravimetric densities up to 18 wt. % H_2 for $LiBH_4$ (see Table 1.4 and Fig.1.3) [5,14,34]. The use of complex metal hydrides for hydrogen storage, however, is challenging because of the kinetic, thermodynamic and reversibility limitations. In 1996, for the first time, Bogdanovic and Schwickardi showed that reversible hydrogenation cycling is feasible in complex sodium alanates when using a titanium-based catalyst [34]. This breakthrough has led to a worldwide effort to develop doped alanates as practical hydrogen storage materials, and research that has been quickly expanded to include amides and borohydrides.

Table 1.4 Material Properties of Complex Hydrides (adopted from [26]).

Material	Density (g/cm^3)	Theoretical maximum H_2 capacity (wt.%)
$LiAlH_4$	0.917	10.54
$NaAlH_4$	1.28	7.41
$LiNH_2$	1.18	8.78
$NaNH_2$	1.39	5.15
KNH_2	1.62	3.66
$Mg(NH_2)_2$	1.39	7.15
$Ca(NH_2)_2$	1.74	5.59
$LiBH_4$	0.166	18.36
$NaBH_4$	1.07	10.57
KBH_4	1.17	7.42
$Mg(BH_4)_2$	0.989	14.82
$AlBH_4$	0.7866	16.78

1.4.1. Li-B-H system

Metal borohydrides are particularly interesting potential solid state hydrogen storage materials due to their very high theoretical capacities of hydrogen. Among them, sodium borohydride ($NaBH_4$) and lithium borohydride ($LiBH_4$) are easily commercially available and have a theoretical gravimetric hydrogen capacity of 10.6 and 18.4 wt.%, respectively [35-37]. The first report of a pure lithium borohydride was reported by Schlesinger and Brown in 1940 [38]. They synthesized lithium borohydride ($LiBH_4$) by reacting ethyl lithium with diborane (B_2H_6) according to the following reaction:

$$2LiH + B_2H_6 \rightarrow 2LiBH_4 \quad (1.4)$$

Also, a direct synthesis from lithium, boron, and hydrogen (reaction. 5.2) at 550-700°C and 3-15 MPa H_2 has been reported [37,38]:

$$Li + B + 2H_2 \rightarrow LiBH_4 \quad (1.5)$$

Lithium brohydrides consists of Li^+ ion surrounded by four $[BH_4]^-$ ions in a tetrahedral configuration. $LiBH_4$ releases three of the four hydrogen atoms from the compound upon melting at 280°C and decomposes into LiH and boron according to the following reaction [6,38]:

$$LiBH_4 \rightarrow LiH + B + 3/2\ H_2 \quad (1.6)$$

The thermal desorption spectrum exhibits four endothermic peaks. The peaks are attributed to: a polymorphic transformation from orthorhombic to hexagnal around 110°C, which is accompanied by a small release of hydrogen (~ 0.3 wt.% H_2); the melting of hexagonal structure at 280°C; and the first and second hydrogen desorption at around 490°C and 680°C respectively [38].

The addition of metal catalysts, for example, Ni [39] and nonmetal ones such as, metal chlorides ($FeCl_2$, $CoCl_2$ and $NiCl_2$ [41]), accelerates the dehydrogenation rate of $LiBH_4$ but does not seem to change its unfavourable thermodynamics. Also, it is reported in [41] that $CoCl_2$ led to the formation of diborane gas (B_2H_6) in contrast to both $NiCl_2$ and $FeCl_2$, which enabled complete hydrogen desorption without diborane.

The authors suggested [41] that, the stronger the binding between the metal and boron, the less possible diborane is produced. Züttel et al. [35] showed that the addition of SiO_2 lowered the hydrogen desorption temperature (Fig. 1.9). Apparently, the SiO_2 additive acted in a sort of catalytic way, but the improvement was still insufficient.

The idea of producing a composite of thermally stable hydride and a second ingredient, either hydride or an intermetallic compound, in order to destabilize the hydride was introduced by Vajo et al. [24]. They showed that the production of $LiBH_4$ /MgH_2 composite, by means of ball milling, decreased the enthalpy change of the reaction (1.6) to the value of ΔH = 46 kJ/molH_2 at the temperature and pressure of 170°C and 1 bar, respectively, by formation of MgB_2 phase according to the following reaction:

$$2LiBH_4 + MgH_2 \rightarrow 2LiH + MgB_2 + 4H_2 \qquad (1.7)$$

The destabilization of $LiBH_4$ with MgH_2 is shown in Fig. 1.10.

Vajo et al. [24] also developed several systems based on $LiBH_4$ destabilized by compositing with MgH_2, MgF_2, MgS and MgSe. In each case, MgB_2 is formed as a destabilizing intermetallic compound. [Recently, it was discovered that the kinetic barrier for the formation of borohydrides is drastically reduced if metal-boron compounds (e.g., MgB_2) are used instead of pure boron as starting materials [43].

Many surveys have been done to find a way to synthesize $LiBH_4$ and study the reversibility of dehydrogenation reaction. The successful rehydroganation of LiH / B mixture of powders to $LiBH_4$ under 35 MPa of hydrogen at 600°C or at 690°C under

20 MPa have been reported by Orimo et al. [36] and Züttel et al. [35] respectively. An investigation of the interaction among these borates, hydrogen, and lithium hydride might provide us with further information to unravel the rehydrogenation mechanism of borohydrides. The scientific understanding of the mechanism of the thermal hydrogen desorption from $LiBH_4$ and the hydrogen absorption reaction remains a challenge and requires additional study.

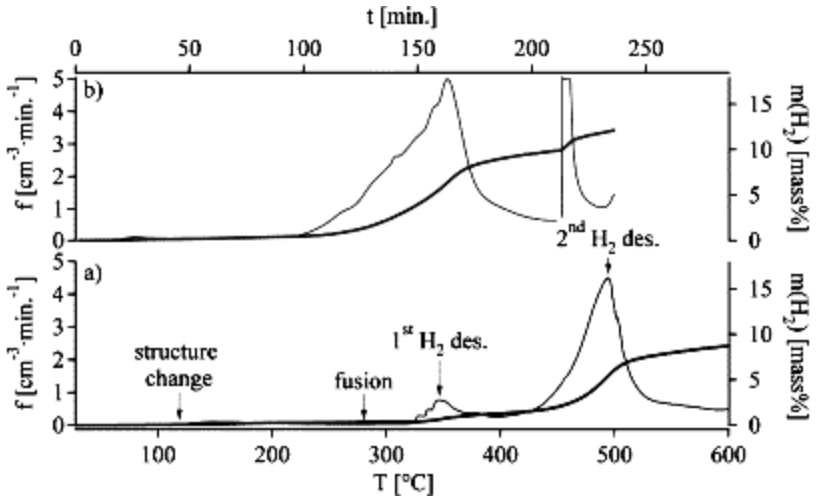

Fig.1.9 Thermal desorption spectra of LiBH4. The sample was heated after evacuation at room temperature with a heating rate of 2 K/min. The gas flow was measured as a function of time and the desorbed hydrogen was computed from the integrated gas flow (a) pure $LiBH_4$ and (b) $LiBH_4$ mixed with SiO_2 as catalyst [35].

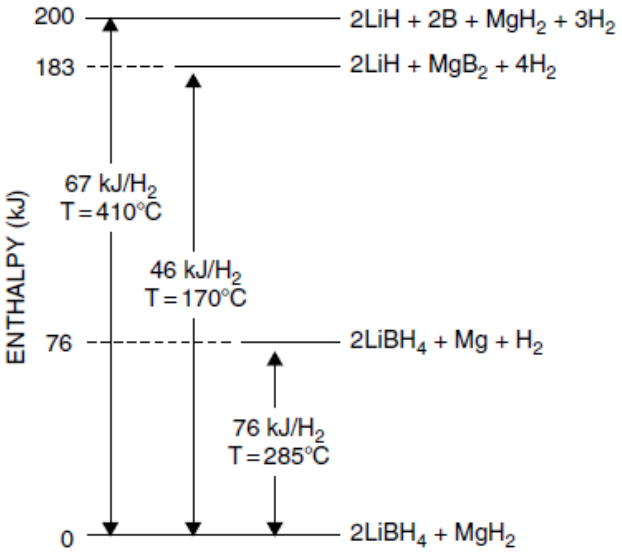

Fig.1.10 Enthalpy diagram for the destabilization of $LiBH_4$ by MgH_2. Addition of MgH_2 reduces the enthalpy for dehydrogenation of $LiBH_4$ through the formation of MgB_2. Dehydrogenation of MgH_2 without $LiBH_4$ decomposition is shown as a possible intermediate step [24].

1.4.2. Li-Al-H system

One of the most interesting hydrides for solid state hydrogen storage is a complex metal hydride $LiAlH_4$ (lithium alanate) [6]. $LiAlH_4$ was first prepared from the reaction between lithium hydride and aluminum chloride according to following reaction [44]:

$$4\ LiH + AlCl_3 \rightarrow LiAlH_4 + 3\ LiCl \qquad (1.8)$$

In addition to this method, the industrial synthesis entails the initial preparation of sodium aluminium hydride from the elements under high pressure and temperature [44].

$$Na + Al + 2\ H_2 \rightarrow NaAlH_4 \qquad (1.9)$$

$LiAlH_4$ is then prepared by metathesis reaction according to:

$$NaAlH_4 + LiCl \rightarrow LiAlH_4 + NaCl \qquad (1.10)$$

which proceeds to produce a high yield of $LiAlH_4$. LiCl is removed by filtration from an ethereal solution of $LiAlH_4$, with a subsequent precipitation of $LiAlH_4$ to yield a product containing around 1 wt.% LiCl [44]. The structure consists of Li atoms surrounded by five AlH_{-4} tetrahedra. The Li^+ centers are bonded to one hydrogen atom from each of the surrounding tetrahedra, creating a bipyramid arrangement [45]. Graetz and Reilly [53] classified $LiAlH_4$ as belonging to a group of hydrides called "kinetically stabilized metal hydrides," which also include AlH_3, $Mg(AlH_4)_2$ and $Ca(AlH_4)_2$ among others. All of these hydrides are characterized by an equilibrium H_2 pressure of their respective PCT curves at room temperature (298K) much higher than 1 bar, which creates a large driving force for decomposition. They are quite stable at near room temperature, though, most likely due to kinetic limitations (as their name indicates). The mechanisms responsible for their stable behaviour are not well understood, although it is quite likely because of slow/hydrogen metal diffusion and surface barriers that hinder the easy formation of molecular H_2 [53].

It is well established [6] that $LiAlH_4$ decomposes and releases H_2 as shown in the steps that follow:

$$LiAlH_4(s) \rightarrow LiAlH_4(l) \quad (1.11)$$

$$LiAlH_4(l) \rightarrow 1/3Li_3AlH_6(s)+2/3Al(s)+H_2(g) \quad (1.12)$$

$$1/3Li_3AlH_6(s) \rightarrow LiH+1/3Al+0.5H_2 \quad (1.13)$$

$$LiH \rightarrow Li+0.5H_2 \quad \text{or} \quad LiH+Al \rightarrow LiAl+0.5H_2 \quad (1.14)$$

(where s=solid, l=liquid and g=gas). Reaction (1.10) is endothermic, (1.11) or (1.12) is exothermic, and (1.13) and (1.14) are both endothermic reactions. (1.11) or (1.12),

(1.12) and (1.13) proceed with a theoretical hydrogen release of 5.3, 2.6 and 2.6 wt.%, respectively [6]. However, LiH is so stable that it only releases the hydrogen thermally at temperatures exceeding 400-450^{o}C —a temperature that is too high for practical hydrogen storage applications [47]—while the reactions (1.11) and (1.12) occur around 112-220^{o}C and 127-260^{o}C respectively. Therefore, the useful theoretical hydrogen capacity is about 7.9 wt.% H_2 from reactions (1.11) and (1.12).

Fig. 1.11 shows the DSC trace of $LiAlH_4$ with the heating rate of 10^{o} C/min, where the first and second peaks are exothermic and endothermic reaction, respectively, and are related to the interaction of $LiAlH_4$ with hydroxyl impurities, and the melting of $LiAlH_4$ respectively [6]. Endothermic peak 2 is due to the melting of $LiAlH_4$. Regarding exothermic peak 3, it was reported in [24] that, in reality, it is a superposition of three events: (a) the decomposition of molten $LiAlH_4$; (b) the initial decomposition of Li_3AlH_6 according to the reaction (1.11); and (c) the solidification of Li_3AlH_6. Finally, the broad endothermic peak 4 is due to the final decomposition of remaining Li_3AlH_6 in solid state according to reaction (1.12). The endothermic peak 5 at around 400°C is usually ascribed to the decomposition of LiH that was formed as a result of decomposition of Li_3AlH_6 in reaction (1.13) or reaction of LiH with Al as shown in reaction (1.14).

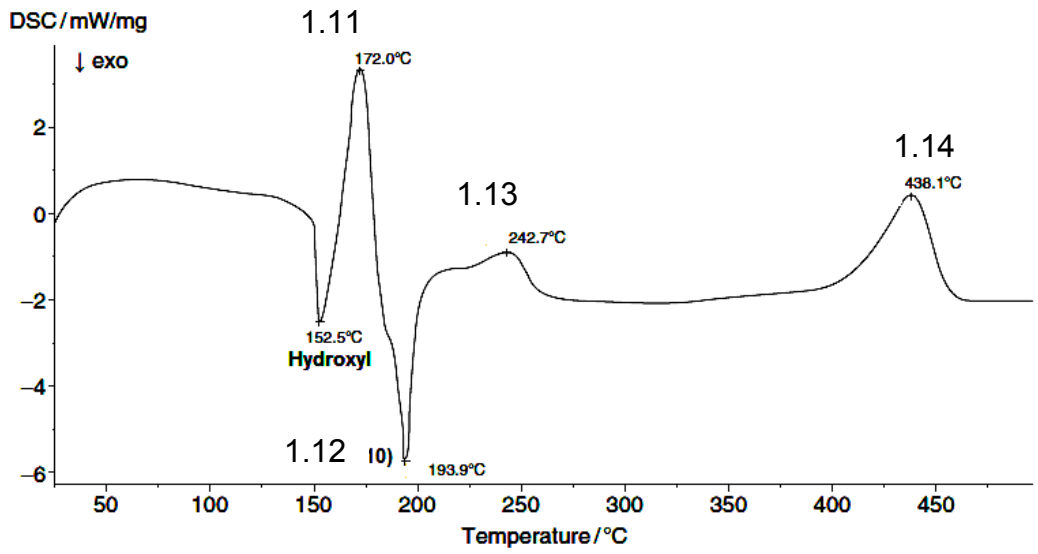

Fig.1.11. DSC trace of as received $LiAlH_4$ (97% purity) [7].

The experimentally observed enthalpy of reaction (1.11) was reported as being equal to -14 kJ/mol H_2 (exothermic) [54] and -10 kJ/mol H_2 (exothermic) [55, 56]. The calculated values of 9.79 and 15.72 kJ/mol H_2, both endothermic, were reported for reaction (1.11) and (1.12) respectively [45].

The PCT equilibrium plateau pressure for the decomposition of $LiAlH_4$ was reported as very high, which could make $LiAlH_4$ irreversible under practical conditions of temperature/pressure. The plateau pressure for Stage I dehydrogenation reaction of $LiAlD_4$, containing a catalytic precursor TiF_3, into Li_3AlD_6, Al and H_2 ((1.11) or (1.12)) was reported by Brinks et al. [52] to be higher than 99 and 87 bar at 53 and 80°C, respectively. Furthermore, Mulana and Nishimiya [57] estimated the enthalpy (ΔH) and entropy (ΔS) for Stage I dehydrogenation (1.11) and the Stage II dehydrogenation reaction (1.12) as being equal to ΔH=17.5 kJ/molH_2 and ΔS=121.6 J/molH_2 K, and ΔH=11.1 kJ/molH_2 and ΔS=62.6 J/molH_2 K, respectively. Assuming ΔH=17.5 kJ/molH_2 and ΔS=121.6 J/molH_2K, the equilibrium pressure for Stage I

dehydrogenation calculated from Eq. (1.3) would amount to 1.88×10^3 and 19.6×10^3 atm at room temperature (24°C=297K) and 170°C (443K), respectively.

Apparently, the first dehydrogenation reaction appears to be completely irreversible due to extremely high pressures required for rehydrogenation. Assuming ΔH=11.5 kJ/molH_2 and ΔS=62.6 J/molH_2 K for Stage II in Eq. (1.3), it is calculated that at 170°C the equilibrium H_2 pressure is around 82 atm. This pressure level, although still relatively high, can be achieved for realizing reversibility under more practical conditions. On the other hand, the computed stability diagrams for $LiAlH_4$/Li_3AlH_6/LiH show very high pressures on the order of 10^3 atm at 170°C needed for the rehydrogenation of LiH/Al into Li_3AlH_6 [6, 58, 59].

The results of the investigations by Andreasen et al. [30] show that the dehydrogenation reaction (1.11) is limited by mass transfer process. For example, the diffusion of Al while the dehydrogenation of Li_3AlH_6 to LiH (reaction 1.12) is controlled by intrinsic kinetics. They showed that ball milling effectively leads to faster kinetics for Stage I function of milling time, while Stage II is more insensitive to ball milling at the isothermal condition (see Fig. 1.12).

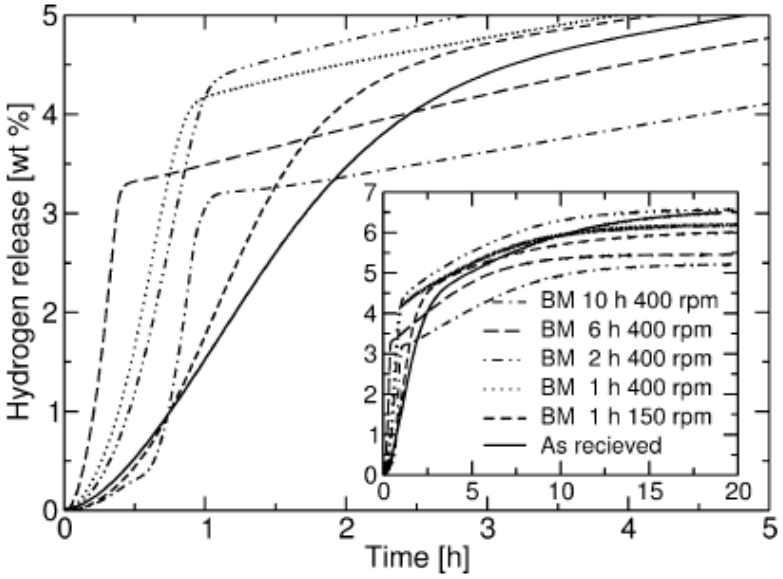

Fig.1.12 Isothermal dehydrogenation curves for ball-milled samples. The isothermal temperature is ~130°C. Dehydrogenation curve for un-milled as-received LiAlH4 at 132oC is included for comparison [30].

A reduction of dehydrogenation temperature for $LiAlH_4$ accompanied by increasing dehydrogenation rate can be achieved by incorporating catalytic precursors or catalytic additives. Catalytic precursors are mostly various halides, such as the metal chlorides $AlCl_3$, $NiCl_2$, $TiCl_3$, $TiCl_3$•1/3$AlCl_3$, $TiCl_4$, VCl_3, $ZrCl_4$, $ZnCl_2$ and bromides VBr_3 [6, 60]. Metal fluorides, such as TiF_3 [52, 61] and NbF_5 [62], were also tried as catalysts for $LiAlH_4$. The mechanism by means of which they act as catalytic additives is not fully elucidated. Most papers, however, report that they locally react with $LiAlH_4$ and form metal salts and free elemental metals, or intermetallic compounds of nanometric sizes, which most likely act as effective nano-metal catalysts [6, 45, 60-61]. A disadvantage of using metal halides is the formation of a

metal salt by-product that constitutes unnecessary ballast (dead-weight) for the microstructure and reduces the total available hydrogen capacity.

The rehydrogenation attempts of $LiAlH_4$ with catalytic precursors and catalytic additives have been reported. Chen et al. [46] investigated $LiAlH_4$ ball milled with the $TiCl_3$•1/3$AlCl_3$ additive and showed reversibility of (LiH+Al) into Li_3AlH_6 at 40 bar and ~175°C with the achieved reversible H_2 capacity of 1.8 wt.%. Wang et al. [63] reported the hydrogen absorption of $LiAlH_4$ doped with $TiCl_3$ and TFH about 44-90 % at 4.5-60 bar of hydrogen pressure by means of a five steps cyclic mechanochemical method. Liu et al. [64] have demonstrated that Ti-doped $LiAlH_4$ can operate as a reversible hydrogen storage material that can release up to 7 wt.% hydrogen commencing at temperatures as low as 80°C, and that the material can be recharged almost quantitatively under remarkably mild conditions by employing liquid Me_2O (dimethylether) as a solvent up to 6 wt.% H_2.

Recently, Rafi-ud-din et al. [65] reported that ball milled $LiAlH_4$ with 5 mol % TiC, dehydrogenated to (LiH+Al) (Stage II), could be successfully rehydrogenated to Li_3AlH_6 at 165°C and 95 bar H_2 pressure with the achieved reversible H_2 capacity of 1.9 wt.%. These experimental results indicate that there is still a possibility of achieving at least a partial reversibility for $LiAlH_4$ containing catalytic additives using an appropriate window of temperature/pressure/time. It must also be mentioned that it has recently been shown that $LiAlH_4$ doped with $TiCl_3$, TiN and $LaNi_5$, and dehydrogenated to the (LiH+Al) mixture can be almost fully rehydrogenated back to $LiAlH_4$ at room temperature in low-boiling dimethyl ether in 100 bar H_2 pressure [64-67].

The addition of metallic and especially nanometric size metal catalysts to $LiAlH_4$ has not been investigated so extensively. Balema et al. [68] reported that the elemental Fe as a catalytic additive was much less effective than $TiCl_4$, Al_3Ti, $Al_{22}Fe_3Ti_8$ and Al_3Fe. They also reported that ball milling of $LiAlH_4$ with 3 mol% $TiCl_4$ for 5 min caused decomposition of $LiAlH_4$ into Li_3AlH_6, Al and H_2 by a rapid reduction of $TiCl_4$ by $LiAlH_4$, forming a LiCl salt. They did not observe any accelerated decomposition of $LiAlH_4$ during ball milling with Fe [68-69]. A partial decomposition of $LiAlH_4$ during ball milling was also observed with the TiF_3 [57] and $NiCl_2$ [70] additives. Resan et al. [71] concluded that the addition of elemental Ti, Fe and Ni did not cause the decomposition of $LiAlH_4$ during ball milling (as did metal chlorides). Kojima et al. [72], besides metal chlorides and intermetallics, also added nanometric Ni as a catalyst to $LiAlH_4$. They found that both chlorides and nanometric Ni led to the decomposition of $LiAlH_4$ during ball milling for 24h. More recently, Zheng et al. [73] reported the thermal behavior of $LiAlH_4$ with unspecified, and most likely, micrometric-sized iron (Fe) and titanium (Ti) additives. They noticed slightly improved dehydrogenation properties, although no isothermal dehydrogenation was carried out.

Varin et al. investigated the thermal behavior and volumetric dehydrogenation of ball milled $LiAlH_4$ with various metallic and non-metallic. They found that an addition of 5 wt.% of nanometric Ni (n-Ni) [75, 76] can improve the desorption properties of $LiAlH_4$. They also demonstrated that this mixture is capable of slowly desorbing large quantities of hydrogen at RT, 40 and 80°C, owing to the strong catalytic action of n-Ni.

1.4.3. Li-N-H system

Lithium nitrides are considered to be one of the most promising hydrogen storage materials for practical hydrogen storage due to their high theoretical capacity (10.4 wt.% H_2) and relatively low decomposition temperature [78]. Chen et al. reported that Li_3N can absorb and desorb hydrogen by the following a two step reversible reaction [78, 79]:

$$Li_3N + H_2 \rightarrow Li_2NH + LiH \quad (1.15)$$

$$Li_2NH + H_2 \rightarrow LiNH_2 + LiH \quad (1.16)$$

These two reaction steps correspond to a total hydrogen storage potential of 10.4 wt.% H_2. While this maximum storage capacity has been demonstrated by several groups, its practical application is limited since full desorption to Li_3N from Li_2NH (reaction (1.15)) requires temperatures greater than 320°C in a dynamic vacuum. Only reaction (1.16) is considered to be suitable for a hydrogen storage system because the latter reaction has a smaller enthalpy change and still possesses a large amount of 6.5 wt.% H_2 [79-86]. The desorption enthalpy change of reaction (1.16) has been calculated to be -44.5 kJ/mol H_2 [78, 79], but a recent measurement [87] suggests that it might be -65.6 kJ/mol H_2, which is higher than the previous theoretical value.

Although this system seems to be relatively ideal for hydrogen storage application, two problems still exist. The first issue is the evolution of ammonia (NH_3) as a transient gas, which is formed through the decomposition of $LiNH_2$. Ammonia gas quickly reacts with LiH to form $LiNH_2$ and H_2 according to the following reactions with the enthalpy change of +84 kJ/molNH_3 and −42 kJ/molH_2, respectively [6,19,88-90]:

$2LiNH_2 \rightarrow Li_2NH + NH_3$ (1.17)

$NH_3 + LiH \rightarrow LiNH_2 + H_2$ (1.18)

This release of NH_3 during the desorption can be poisonous for the membrane of a conventional PEM fuel cell, even at trace levels, therefore, at present, even the smallest release of ammonia in the hydrogen gas cannot be tolerated in the system [6]. The newly formed $LiNH_2$ decomposes again and repeats the cycle of reactions (1.17) and (1.18). Such successive reactions continue until all $LiNH_2$ and LiH completely transform to Li_2NH and H_2. It has been shown that reaction (1.18) takes place extremely quickly (in the order of the microseconds). Even with such high reaction rates, the escaping of NH_3 from the hydrogen storage system has been reported and used as the evidence to support the mechanism as defined by reaction (1.17) and (1.18). The second problem of this particular process is the high operational temperature for the hydrogen absorption/desorption. This barrier may come from both thermodynamic and kinetic issues.

A lot of effort has been devoted to address these problems such as: (i) partial substitution of Li with elements that have larger electro-negativity, such as Mg [82-84, 92,93]; (ii) searching for effective catalysts [83, 86,89]; and (iii) using high energy ball milling [6]. The first approach has been shown to be effective in reducing the hydriding and dehydriding temperature to around 200°C with a hydrogen pressure of 30 bars [94-97]. However, the second approach has not yielded many positive results, even though a wide range of catalysts, such as Ni, Fe, Co, VCl_3, $TiCl_3$, TiO_2, Ti, Mn, MnO_2, V, and V_2O_5, have been investigated [83,86,88,89]. The best result appears to show less than 50°C reduction in the peak temperature for hydrogen

desorption when the $LiNH_2$ and LiH mixture, with and without catalysts, are compared [83,86,88,89]. The third approach exhibits some promising results, such as showing a decrease in the peak temperature for desorption reaction from 350 to 270°C, without and with ball milling respectively [88,89].

Recently, as shown by Yao et al [89], the release of NH_3 can be prevented by high energy ball milling. In spite of this advance, several other groups [79,88] have reported the presence of NH_3 in the emission gas from the $LiNH_2$/LiH mixture. The differences found between the different groups has not yet been explained, but it might be due to different ball milling designs. Another issue is the mechanism of reaction (1.16), which has not been clearly understood. Some reports suggest that $LiNH_2$ may directly react with LiH to produce H_2 according to reaction (1.16), while others propose that NH_3 is involved as a transient gas by reactions (1.17) and (1.18) [28,19,88-91].

Another new approach has been reported by Xie et al. to improve the kinetic properties and remove NH_3 release [98]. They synthesized Li_2NH hollow nanospheres to decrease the diffusion distance to nanometers and increase the specific surface area. These hollow nanospheres have diameters ranging from 100 to 400 nm and 20 nm shell thickness. In addition, the specific surface area is 79.4 m2/g and the crystallite sizes are about 15 nm. They have shown that the desorption onset and peak temperature of the reaction (1.16), as measured by Differential Scanning Calorimetry (DSC), is reduced to 179 and 230°C, respectively. Furthermore, they have reported that the activation energy for the hydrogen absorption in the reaction (1.16) is reduced to 106 kJ/mol due to the large specific

surface area and shorter diffusion distance of the nanometric hollow structure. In spite of the short diffusion distance, this newly designed Li_2NH hollow nanospheres don't show significantly improved hydrogen storage kinetics compared to the nano-structured ($LiNH_2$+LiH) mixture processed by the high energy ball milling.

1.4.5. Li-N-Mg-H system

The kinetic and thermodynamic properties of Li-N-H system require further improvement for practical applications [78-89]. The strongly endothermic nature of the reactions mentioned above requires high operation temperatures, and the thermodynamic properties of the reaction must be improved in order to lower the desorption/absorption temperatures. As mentioned before, Nakamori et al. [99] noted that the dehydrogenation reaction of $LiNH_2$ can be promoted by substituting Li with Mg (which is the element with larger electronegativity). As an alternative to the ($LiNH_2$-LiH) system the ($LiNH_2$-MgH_2) system was proposed by Luo et al. [97,100,101] and Ichikawa et al. [102]. The research on the ($LiNH_2$-MgH_2) system was then pursued vigorously by other researchers [97, 103-111]. These studies revealed that the Li-Mg-N-H ternary system has improved thermodynamic properties compared to the $LiNH_2$-LiH system. It was found that $2LiNH_2/MgH_2$ and $Mg(NH_2)_2$/2LiH systems could reversibly store 5.5 wt.% H_2 at 180°C by the following reactions [94, 97, 100, 101, 112]:

$$LiNH_2+0.5MgH_2 \rightarrow 0.5Li_2Mg(NH)_2+H_2 \quad (1.19)$$

$$0.5Li_2Mg(NH)_2+H_2 \rightarrow 0.5Mg(NH_2)_2+LiH \quad (1.20)$$

After an initial dehydrogenation, the 2:1 $LiNH_2/MgH_2$ mixture was transformed into a new phase with a suggested composition of $Li_2Mg(NH)_2$. In the subsequent

rehydrogenation process, this phase was hydrogenated to $Mg(NH_2)_2$ and LiH, than the initial $LiNH_2/MgH_2$ mixture. Therefore, the reversible reaction is actually processed between ($Li_2Mg(NH)_2+2H_2$) and ($Mg(NH_2)_2+2LiH$) as shown in equation (5-18). The heat of the endothermic hydrogen desorption reaction, measured by differential scanning calorimetry, has been reported to be 44.1 kJ/mol H_2, which is suitable for PEM Fuel Cell application. The relatively high activation energy (102 kJ/mol) still remains an issue [95, 100].

Further efforts have been devoted to the composition adjustments for obtaining higher hydrogen capacities. Leng et al. reported that the $3Mg(NH_2)_2/8LiH$ mixture absorbed/desorbed reversibly 6.9 wt.% of hydrogen through the following reaction [113]:

$$Mg(NH_2)_2+8/3\ LiH \rightarrow 4/3\ Li_2NH+1/3Mg_3N_2+8/3H_2 \quad (1.21)$$

When the molar ratio of $Mg(NH_2)_2$ to LiH was adjusted to 1:4, the hydrogen storage capacity of the mixture was increased to 9.1 wt.% H_2 as shown below [99]:

$$Mg(NH_2)_2+4\ LiH \rightarrow 4/3\ Li_2NH+1/3Mg_3N_2+4H_2 \quad (1.22)$$

These results indicate that the composition changes can enhance the hydrogen-storage capacity of the Li-Mg-N-H system due to the change of dehydrogenation/hydrogenation reaction pathways. Recently, even more interest in this system was attracted by a paper by Alapati et al. [114], which theoretically predicted a direct reaction between $LiNH_2$ and MgH_2, with a 1:1 molar ratio and formation of new LiMgN phase, as shown in reaction (1.23). They calculated the

reaction enthalpy of 29.7kJ/molH_2 at 0 K for this system, which is an acceptable value for on-board hydrogen-storage applications.

$$LiNH_2+MgH_2 \rightarrow LiMgN+2H_2 \quad (1.23)$$

Further first-principles calculations showed that the reaction between $LiNH_2$ and MgH_2 at this molar ratio might be a multistep reaction as follows (Eq. (1.24))[115]:

$$\begin{aligned} &LiNH_2+MgH_2 \rightarrow 0.5\ Mg(NH_2)_2 + LiH+0.5\ MgH_2 \\ &\rightarrow LiH+0.25\ Mg(NH_2)_2 + 0.25\ Mg_3H_2 + H_2 \\ &\rightarrow 0.5LiH + 0.25Li_2Mg(NH)_2+0.25Mg_3H_2+1.5H_2 \\ &\rightarrow LiMgN+2H_2 \end{aligned} \quad (1.24)$$

Osborn et al. [116] showed that the $LiNH_2/MgH_2$ (1:1) mixture milled for 3h followed a new reaction pathway at 210°C instead of the originally predicted reaction in Equations (1.23) and (1.24) as described below (Eq. (1.25)):

$$LiNH_2+MgH_2 \rightarrow 1/3\ Li_2Mg_2(NH)_3 + 1/3MgH_2+1/3LiH+H_2 \quad (1.25)$$

Although Lu et al. [104] reported that approximately 8.1 wt.% H_2, a theoretical value of hydrogen desorption for the reaction in Equation (1.23), was observed by means of thermogravimetric analysis (TGA) from the sample milled for 24 h, the effects of the co-product of NH_3 have not been eliminated. Therefore, the details of the structural information of the solid products needs to be further ascertained. Unlike the previous investigations cited, Liang et al. [106, 117] reported that four sequential reactions proceeded during 36 h of ball milling and the subsequent heating process for the $LiNH_2/MgH_2$ (1:1) mixture (Eq. (1-26)):

$LiNH_2+MgH_2 \rightarrow 0.5\ Mg(NH_2)_2 + LiH+0.5\ MgH_2$ (milled for 12 h)

$\rightarrow LiH+0.25\ Mg(NH_2)_2 + 0.5\ MgNH + 0.25\ MgH_2+0.5H_2$ (milled for 36h) (1.26)

$\rightarrow 0.5LiH + 0.25Li_2Mg(NH)_2+0.5MgNH+0.25\ MgH_2+H_2$ (heated to 220°C)

$\rightarrow 0.25Mg_3N_2+0.25Li_2Mg(NH)_2+0.5LiH+1.5H_2$ (heated to 390°C)

The ternary nitride product, LiMgN, which was predicted by Alapati et al. and Akbarzaelh et al. [114, 115], has not been obtained, even though the sample was heated up to 390°C. Therefore, the above theoretical and experimental findings have not reached an agreement on the dehydrogenation reaction pathways of $LiNH_2/MgH_2$ (1:1) system due to its complexity and sensitivity to experimental conditions, specifically those related to ball milling. The problem that clearly appears from the reviewing of all these relevant studies is that there is a strong influence of various ball milling conditions on the phase transformations occurring during ball milling. This is evident in the conflicting results of the various hydride phases and their mixtures reported after ball milling by various authors. Obviously, the initial phase composition obtained after milling has a substantial influence on subsequent dehydrogenation at elevated temperatures.

2. Objectives

The previous chapter has shown that the area of complex metal hydrides, especially lithium based complex hydrides, has not been fully investigated. In this thesis the nanostructured lithium complex hydrides are investigated in order to develop a breakthrough material in the field of solid-state hydrogen storage. The primary motivation for studying Li complex hydrides is their potential ability to store large amounts of hydrogen. There are still thermodynamic and kinetic barriers, however, to the practical utilization of these materials. To address these two critical barriers, the present study investigates the dependence of the thermodynamic and kinetic properties of Li complex hydrides on their chemical composition and degree of mechanical activation. To accomplish these objectives, the goal of each topic is outlined below.

2.1. Nanostructured M – B – H – O system (M = Li and Na)

As mentioned earlier, the results of investigations in the literatures show that formation of an intermediate phase of Mg-B, such as MgB_2, can destabilize $LiBH_4$ and consequently cause a decrease of enthalpy change of reaction and decomposition temperature. Many surveys have been done to destabilize $LiBH_4$ by means of a Mg based component such as MgH_2, MgF_2, MgS and MgSe. Although these compounds can improve the enthalpy of the reaction to some extent, all of these systems exhibit rates of hydrogen desorption that are much too slow for practical applications. In this study, magnesium hydroxide $Mg(OH)_2$ has been used as a destabilizing agent for $LiBH_4$ for the first time. In addition, the effect of $Mg(OH)_2$ on the hydriding and dehydriding properties of $NaBH_4$ was also investigated. The later system was

analyzed by Drozd et al. [118]. However we repeated the experiments on this system in order to study if it is reproducible. Furthermore, the effect of nanometric nickel (n-Ni) on the desorption properties of M-B-Mg-H (M=Li and Na) systems was also investigated.

2.2. Nanostructured Li-N-Mg-H system

The effect of the milling energy on the phase transformations (reaction path ways), which occur as a function of the ball milling energy injected into the hydride system ($LiNH_2$+$nMgH_2$), systematically has been studied for molar ratios from 0.5 to 2.0. The various ball milling conditions have strong influence on the phase transformations in this system. Using theoretical approaches and experimental observations of the movement trajectories of steel balls in a milling cylinder/vial, the total energy of milling was calculated for each mode of milling (as described in Chapter 9). Milling energy is recommended as a key parameter to compare the results of ball milling of varying hydride systems.

2.3 Nanostructured Li-Al-H system

Research on this hydride focuses on the effect of ball milling with various nanometric additives on the dehydrogenation/rehydrogenation behavior of $LiAlH_4$. The role of nanostructuring and the influence of chemical composition on mechanical and thermal dehydrogenation properties are systematically investigated by comparing their apparent activation energies. Reversibility and reaction pathways at various temperatures are also explored.

3. Experimental

3.1. Materials

The used starting hydrides and additives in this work were listed in the Table 3.1.

Table 3.1 Chemical hydrides and additives materials used in this work.

Material	**Purity (%)/ particle size (nm)**	**Provider**
$LiBH_4$	95	Alfa Aesar
$NaBH_4$	98	Alfa Aesar
$LiNH_2$	95	Sigma–Aldrich
$LiAlH_4$	97	Alfa Aesar
MgH_2	98	ABCR GmbH & Co.KG
KH	30 wt% suspension in mineral oil	Sigma–Aldrich
NaH	95	Sigma–Aldrich
$Mg(OH)_2$	95	Alfa Aesar
Nano TiC	99/40 nm	Hefei Kaier Nanometer Energy and Technology Co. Ltd.
Nano TiN	97/20 nm	Hefei Kaier Nanometer Energy and Technology Co. Ltd.
Nano ZrC	97/40 nm	Hefei Kaier Nanometer Energy and Technology Co. Ltd.
Nano Ni (9.5,17.9 85 g/m^2)	0.46 - 0.61 C wt.% 0.1 - 17.7 O wt.%	Vale Inco Ltd
Nano Fe	98	Nano Iron, s.r.o., The Czech Republic
Micro Fe	99.5	Alfa Aesar

3.2. Synthesis of nanostructure hydride composites

3.2.1. Chemical compositions

The starting materials compositions for synthesizing composites have been listed in table 3.2.

Table 3.2. Chemical composition of the studied systems

System	n	Additive
$LiBH_2+nMg(OH)_2$	2	-
$LiBH_2+nMg(OH)_2$	2	5wt.% n-Ni
$NaBH_2+nMg(OH)_2$	2	-
$NaBH_2+nMg(OH)_2$	2	5wt.% n-Ni
$LiNH_2+nMgH_2$	0.5,0.7,1,2	-
$LiNH_2+0.5MgH_2$	-	5wt.%KH
$LiNH_2+0.5MgH_2$	-	5wt.%NaH
$LiAlH_4$	-	5wt.% n-Ni
$LiAlH_4$	-	5wt.% n-Fe
$LiAlH_4$	-	5wt.% m-Fe
$LiAlH_4$	-	5wt.% n-TiC
$LiAlH_4$	-	5wt.% n-TiN
$LiAlH_4$	-	5wt.% n-ZrC

3.2.2. Milling procedure

Syntheses of nanostructured hydrides were implemented by means of controlled mechanical milling (CMM) in the magneto-mill, Uni-Ball-Mill 5 manufactured by A.O.C. Scientific Engineering Pty Ltd, Australia [6]. In this particular ball mill the milling modes with varying milling energy can be achieved by using one or two strong NdFeB magnets, changing their angular positions and changing the number of hard steel balls (25mm in diameter each) in a milling vial.

Milling tests were performed under two different milling modes, low energy shearing mode (LES) and high energy impact mode (IMP), at 200 rpm. Hereafter, the different milling modes are identified by IMP/LES followed by numbers such as IMP68-4B. The first two numbers refer to the positions of the magnets (6 and 8 o'clock) and the last number shows the number of steel balls in the vial (4B=4 balls etc.). The ball-to-powder mass ratios (R) used in this work were 40 (R40), 60 (R60) and 132 (R132). The distances of magnets to vial, work distance (WD), were 10 and 2 mm for magnet at 6 and 8 o'clock respectively in all the tests. Fig. 3.1 shows schematically a set up for a strong impact mode with two magnets positioned at 6 and 8 o'clock, After loading with powder, an air-tight milling vial with an O-ring, equipped with a pressure valve mounted in the lid, was always first evacuated and then purged several times with ultra-high purity argon (Ar) gas (99.999% purity) before final pressurization with H_2. The pressure of high purity hydrogen (purity 99.999%: O_2< 2 ppm; H_2O< 3 ppm; CO_2< 1 ppm; N_2< 6 ppm; CO< 1 ppm; THC< 1 ppm) in the vial was always kept constant at ~ 600 kPa during the entire milling process. Through the entire milling process the milling vial was continuously cooled with an air fan. All the powder

handlings before and after milling were performed in a purged glove box under overpressure of high purity argon (purity 99.999%) in order to minimize any possible contamination by moisture or oxygen from air. Additionally, pressure changes during milling were recorded to estimate the amount of hydrogen loss. A volumetric method was used to calculate the amount of hydrogen absorbed during milling. The details of calculation are given in Appendix A-1. The composition of powders and the processing parameters applied during controlled milling are shown in Table 3.3

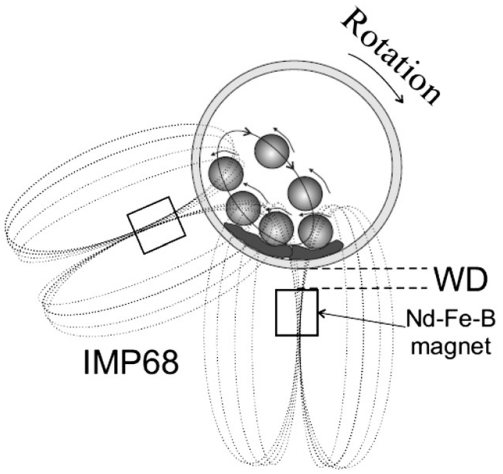

Fig. 3.1 A schematic showing the angular position of magnets at 6 and 8 o'clock for ball milling under high energy impact mode (Q_{TR}=72.6 kJ/gh) in the Uni-Ball-Mill 5 [6].

Table 3.3 Composition of powders and Milling parameters

System	Composition	Milling mode	R	# of balls	BM time (h)
Li-B-Mg-H	$LiBH_4$+2$Mg(OH)_2$	IMP68	40	4	0.5
	$LiBH_4$+2$Mg(OH)_2$ +5wt.%n-Ni	IMP68	40	4	0.5
Na-B-Mg-H	$NaBH_4$+2$Mg(OH)_2$	IMP68	40	4	0.5
	$NaBH_4$+2$Mg(OH)_2$ +5wt.%n-Ni	IMP68	40	4	0.5
Li-N-Mg-H	$LiNH_2$+0.5MgH_2	IMP68	40,60132	4	21, 25, 50
	$LiNH_2$+0.7MgH_2	IMP68	40,60,132	4	21,25,50
		LES6	40,60,132	3	21,25
	$LiNH_2$+0.85MgH_2	LES6	60	4	25
	$LiNH_2$+0.9MgH_2	IMP68	60	4	12
		LES6	60	4	24
	$LiNH_2$+1MgH_2	IMP67	40	4	1,4,6,25
		LES6	40	4	21
	$LiNH_2$+1.5MgH_2	IMP67	40	4	1,4,6,25
	$LiNH_2$+2MgH_2	IMP68	40	4	21
		LES6	40	3	21
		LES6	40	2	21
	$LiNH_2$+0.5MgH_2 +5wt.% KH	IMP68	40	4	0.25,15,25
	$LiNH_2$+0.5MgH_2 +5wt.% NaH	IMP68	40	4	0.25
Li-Al-H	$LiAlH_4$+5wt.% µFe	IMP68	132	4	0.25
	$LiAlH_4$+5wt.% n-Fe	IMP68	132	4	0.25,1,5
		IMP68	132	2	0.25
		LES6	132	4	0.25,1,5
	$LiAlH_4$+5wt.% n-Ni (SSA 9.5 g/m2)	IMP68	132	4	0.25
	$LiAlH_4$+5wt.% n-Ni (SSA 17.9g/m2)	IMP68	132	4	0.25
	$LiAlH_4$+5wt.% n-Ni (SSA 85g/m2)	IMP68	132	4	0.25
	$LiAlH_4$+5wt.% n-TiC	IMP68	132	4	0.25
	$LiAlH_4$+5wt.% n-TiN	IMP68	132	4	0.25
	$LiAlH_4$+5wt.% n-ZrC	IMP68	132	4	0.25

3.3. Analysis of powder morphology

3.3.1. X-Ray diffraction

The crystal structure of powders was characterized with a Bruker D8 powder diffractometer using monochromated CuKα1 radiation at an accelerating voltage of 40 kV and a current of 30 mA. One powder sample was placed on a home-made environmental brass holder with a Cu plate for powder support which was loaded in a glove box filled with Ar. Upper and lower part of the environmental holder is sealed through a soft-rubber O-ring and tightened using threaded steel bolts with nuts. The scan range was from 2θ = 10° to 90° and the rate was 1.2° min^{-1} with a step size of 0.02°. The nanograin size of phases was calculated from the broadening of their respective X-ray diffraction peaks. Since the Bragg peak broadening in an XRD patterns is due to a combination of grain size and lattice strains, it is customary to use computing techniques by means of which one can separate these two factors. The separation of crystallite size and strain was obtained from a Cauchy/Gaussian approximation by a linear regression plot according to the following equation [119]:

$$\frac{\delta^2(2\theta)}{tan^2\theta} = \frac{K\lambda}{L}\left(\frac{\delta(2\theta)}{tan\theta\ sin\theta}\right) + 16e^2 \qquad (3\text{-}1)$$

where the term K λ/L is the slope, the parameter L is the mean dimension of the crystallite, K is a constant (≈1) and e is the so-called 'maximum' micro-strain (calculated from the intercept), λ is the wavelength and θ is the position of the analyzed peak maximum. The term $\delta(2\theta) = 1-(b^2/B^2)(rad)$ is the instrumental broadening-corrected "pure" XRD peak profile breadth, where B and b are the

breaths in radians of the same Bragg peak from the XRD scans of the experimental and reference powder, respectively. They were automatically calculated by the diffractometer software from the full width at half maximum, FWHM. The powder of the LaB6 compound, the National Institute of Standards and Technology (NIST) standard reference materials (SRM) 660, was used as a reference for subtracting the instrumental broadening.

The unit lattice cell parameters of $LiAlH_4$ were computed using the Materials Data Inc. Jade v. 5 software [120] using the monoclinic crystallographic space group P21/c [69] and unit cell dimensions reported in the ICDD file #12-0473. Fifteen (hkl) diffraction planes at the corresponding range of 2θ=19.8-45.1° were taken for calculations of lattice parameters.

3.3.2. FTIR

The Fourier transform infrared spectroscopy (FTIR) measurements were performed at Mc Master university with a Bruker Tensor 27 at room temperature in the range of 4000-400cm^{-1} to characterize the $LiNH_2$, $Mg(NH_2)_2$, MgNH, LiH and $Li_2Mg(NH)_2$ phases. The powder samples were ground with KBr and pressed into pellets. The sample preparation and test performed under argon atmosphere.

3.3.3. Scanning Electron Microscopy

Morphological examination of iron additive and ball milled composites was conducted with high-resolution, field emission SEM (FE SEM) LEO 1530 under backscattered (BSD) and secondary electron (SE) modes.

3.4. Thermal analysis and hydrogen storage properties

3.4.1. Differential Scanning Calorimeter

The thermal behavior of powders was studied by differential scanning calorimetry (DSC) (Netzsch 404) of ~7 mg samples in an Al_2O_3 crucible. Samples were heated to 500°C at a heating rate of 5, 10 and 15°C/min in Ar atmosphere to find the number and the temperature range of reactions. The powder was transported to a DSC instrument in a glass vial filled with Ar and then quickly loaded into an Al_2O_3 crucible with a lid. This operation took about 1-2 min and for that short period of time the powder could be in contact with air.

3.4.2. Hydrogen storage properties

The hydrogen desorption/absorption was evaluated using a second generation volumetric Sieverts-type apparatus custom-built by A.O.C. Scientific Engineering Pty Ltd., Australia as shown in Fig. 3.2. This apparatus built entirely of austenitic stainless steel allows loading of a powder sample in a glove box under argon and its subsequent transfer to the main unit in a sealed austenitic stainless steel sample reactor without any exposure to the environment. The weight of the powder sample in the ab/desorption experiments was in the range of 20-30 mg.

The calibrated accuracy of desorbed hydrogen capacity is about ±0.1 wt.% H_2 and that of temperature reading ±0.1°C. Before starting the desorption test, the inner tubing of the apparatus and reactor were evacuated and purged 4 times with argon and then two times with hydrogen. The furnace of the apparatus was heated separately to the desired test temperature and subsequently inserted onto a tightly sealed powder sample reactor inside which a pressure of 1 bar H_2 was kept. Hence,

the beginning of the desorption test was in reality pseudo-isothermal before the powder sample temperature reached the desired value. However, the calibrated time interval within which the powder sample in the reactor reaches the furnace temperature is ~400-600 s in the 100-350°C range, which is negligible compared to the desorption completion time especially at temperatures below 200°C. Therefore, one can consider the test as being “isothermal” for any practical purposes at this range of temperatures. After desorption the powder without removal from the reactor was subjected to absorption at pre-selected temperature and pressure. The amount of desorbed/absorbed hydrogen was calculated from the ideal gas law as described in detail in Appendix A-2 [6].

Hydrogen desorption curves were also corrected for the hydrogen gas expansion due to the increase in temperature. The amount of desorbed/absorbed H_2 expressed in wt.% is calculated with respect to a total weight of powder including the additives. To study the rehydrogenation possibility of the hydride systems, they were, first, fully dehydrogenated at the appropriate temperature and subsequently they were rehydrogenated in hydrogen pressure between from 50 to 100 bar for a certain time (depending on the system). This step was followed by second dehydrogenation at selected temperature. All these steps were done sequentially without opening the reactor.

The apparent activation energy for volumetric hydrogen desorption was estimated using the registered dehydrogenation curves by applying a simple Arrhenius equation following Sandrock et al. [121]

$$k = k_0 e^{\frac{-EA}{RT}} \quad (3.2)$$

where k is the rate of hydrogen desorption in convenient engineering terms of wt.% H_2/h measured from the slope of the volumetric hydrogen desorption curves registered by the Sieverts-type apparatus (the selected linear portion of each pertinent dehydrogenation curve was fitted by a linear equation obtaining its slope), EA is the activation energy in kJ/mol, R is the gas constant (8.314472 J/mol K) and T is absolute temperature (K). The measured rates were plotted in the Arrhenius form as ln k vs. 1000/T.

Fig. 3.2 A Sieverts-type apparatus custom-built by A.O.C. Scientific Engineering Pty Ltd., Australia, for evaluating hydrogen storage properties.

4. Semi-empirical study of ball milling energy

In this study we have been tried to estimate the total energy produced during the milling process. This energy can be separated into shearing and impact energies, which are substantially increased by applying the strong magnets on ball mill machine. These two energies were calculated separately based on simple friction and kinetic energies concept. The following simplifying assumptions are used in calculations:

- Friction coefficient between balls and walls is constant
- Each ball imparts the same impact energy on the milled powder
- Both friction and kinetic energies resulting from the gravity force acting on balls are negligible.
- Temperature of vial, balls and hydrogen gas in the vial is the same during ball milling.

Table 4.1 lists the experimental parameters used in the calculations

Table 4.1 The values of different parameters used for calculations.

R_{vial}	75mm
r_{ball}	12.5mm
ω	200rpm
m_{vial}	4030 g
m_{ball}	65 g
$m_{insulation}$	220 g
WD_{mag6}	10mm
WD_{mag8}	2mm
μ [122-125]	0.3
$C_{vial(316)}$ [126]	0.5 (J/g℃)
$C_{balls(420)}$ [126]	0.46 (J/g℃)
$C_{glass\ wool}$ [126]	0.84 (J/g℃)
C_{vH2} [127]	3.33T+27.37 (J/mol℃)
n_{H2}	0.116 mol
m_{R40}	6.5 g
m_{R60}	4.3 g
m_{R132}	1.969 g

4.1. Shear energy

The sliding of steel balls on the layer of milled powder spread on the wall surface of milling vial under a big magnetic force causes to produce a significant amount of shear energy, Q_s, due to friction that is estimated from the following relationships:

$$Q_s = F_f \times S \ (J) \quad (4\text{-}1)$$

$$F_f = F_N \times \mu \ (N) \quad (4\text{-}2)$$

where F_f, S, F_N and μ are the friction force, sliding distance, normal force, and the friction coefficient between ball and wall, respectively. Fig. 4.1 illustrates the variations of magnetic force, as the normal force of friction, with the distance, d, between the magnet and the ball. This plot was achieved by installing the magnet and a steel pin (with the same diameter as the ball) on the upper and lower grips of the tensile test machine and performing a pseudo-tensile test. The magnetic force vs.

d fitted to the experimental data (Fig. 4.1) changes according to the following functional dependence:

F_m=-3.3623d+84.547 (4-3)

where F_m is in N and d is in mm. The energy Q_s per one rotation ($2\pi \times R_{vial}$) can be expressed by substituting the sliding distance (rotation) $S=2\pi \times R_{vial}$ and $F_m=F_N$ in Eq. (4-1) and (4-2), which results in the following equation:

$Q_s=2\pi \times R_{vial} \times F_m \times \mu$(J/rotation) (4-4)

Table 4.2 shows the friction coefficients of some ceramics and oxides against a rotating steel counterpart. One can assume that the friction coefficient between steel ball and the ($LiNH_2$+MgH_2) powder mixture is near the average of these values (~ 0.3). Substituting F_m from Eq. (4-3) and taking R_{vial} and the average μ=0.3 from Table 4.1 one obtains

Q_s= -0.477d+12 (J/rotation) (4-5)

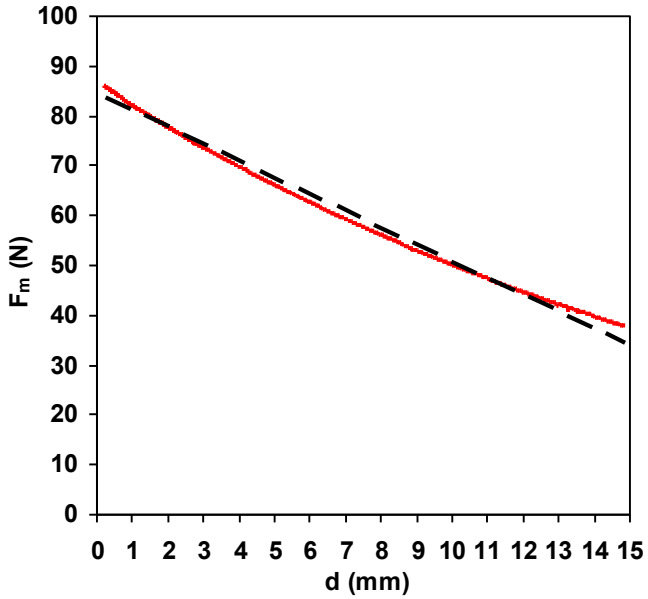

Fig. 4.1. Variations of magnetic force with the distance d between the magnet and the ball. The continuous line is obtained from the experiment and the broken line is a fitted straight line (Eq. (4.3)).

Table 4-2 Friction coefficient of some ceramics and oxide powder against the steel counterpart.

Ceramic	Counterpart	COF
Sialon (grade TCQ)	steel	0.45[122]
β-Sialon	steel	0.22[123]
95 mol.% ZrO_2, 5 mol.% Y_2O_3	hardened steel	0.3[124]
92 mol.% ZrO_2,4 mol.% Y_2O_3, 4 mol.% CeO_2	hardened steel	0.4[124]
Y-TZP ceramics	steel	0.35 [125]

4.2. Impact energy

Direct observations of the ball movement show that in the high-energy impact modes each ball travels from the 6 o'clock to the 9 o'clock position, and then is aggressively attracted by the 6 o'clock magnet and impacts the wall. Eq. (4-3) shows that at the critical distance d_{crit}=25 mm the magnetic force F_m=0. We assume that a steel ball starts falling under gravity forces from the position at the center of the vial (R_{vial}=75 mm) until it reaches to this critical distance d_{crit}=25 mm. At the exact critical distance the kinetic energy of moving ball is very small and negligible. From this point, ball is strongly affected by the magnetic force, which increases by decreasing the distance to the impact point at the bottom of the vial at the working distance WD from the magnet (Fig. 4.2).

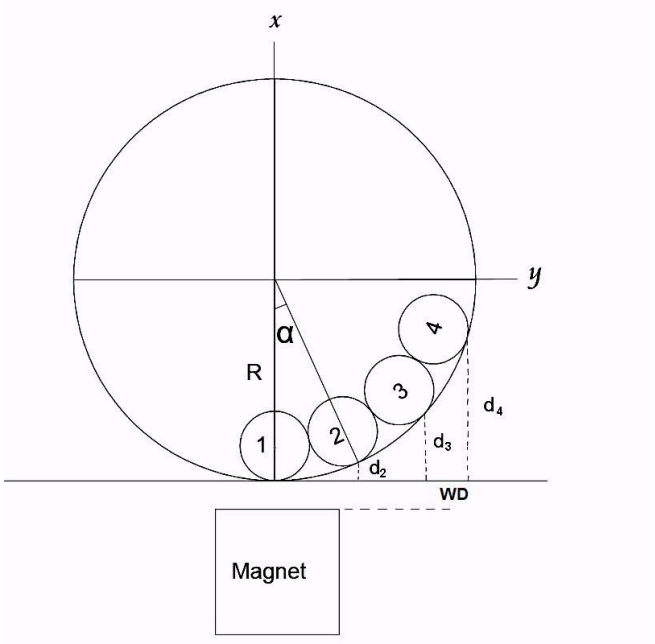

Fig. 4.2. A schematic of ball trajectories in the vial with a 6 o'clock magnet position.

In order to simplify the calculations, it is assumed that the ball is falling under a constant force, which is the average magnetic force between these two points expressed as follows:

$$F_{avg} = \frac{(F_m^{d_{crit}} + F_m^{WD})}{2} \qquad 4\text{-}6)$$

The kinetic energy per impact, Q_i, can be approximated by a general equation for the kinetic energy in the following form:

$Q_i = ½\ m_{ball} \times v^2$ (J/impact) (4-7)

Now substituting the acceleration, a

$a = F_{avg}/m_{ball}$ (4-8)

and the ball velocity, v

$v^2 = 2a \times d$ (4-9)

the final equation for Q_i is obtained in the following form:

$$Q_i = -0.04d+1.05 \text{ (J/impact)} \quad (4\text{-}10)$$

4.3. Ball positions

Since the total number of balls, which can be placed along the total vial circumference is 13, therefore the angle between each two balls is as shown in Fig. 4.2:

$$\alpha = 360°/13 = 27.7°$$

The maximum number of balls, which can stay in contact in equilibrium with the rotating vial during the ball milling is 4 as shown in Fig. 4.2. The distance between these balls and the magnet surface can be calculated by means of angular equation of a circle as follows:

$$y_n = R_{vial} \cos \alpha_n \quad (4\text{-}11)$$

$$x_n = R_{vial} \sin \alpha_n \quad (4\text{-}12)$$

$$\alpha_n = 27.7(n -1) \ (n=1,2,3,4) \quad (4\text{-}13)$$

$$d_n = R_{vial}-y_n+WD \quad (4\text{-}14)$$

where n, α_n and d_n are the ball number in Fig. 4.2, the angle between position 1 and the instant position of ball “n” and the distance from the vial-ball contact point to the magnet surface, respectively. Substituting the values of R_{vial} and WD from Table 4.1 in Eq.(4-14) reveals that the distances of balls 2, 3 and 4 (d_2=28.6 mm, d_3=52 mm and d_4=86 mm) are bigger than the critical distance (d_{crit}=25 mm). This means that these three balls are not affected by the magnetic force of the magnet at the 6 o’clock position and do not contribute to any significant friction on the wall.

4.4. Total energy of ball milling

The number of balls acting in shear (N_s) and the number of impacts per rotation which will be now called "impact factor M" are changed by adding the second magnet to the ball mill. These two parameters, N_s and M, were measured for 5 different milling modes, by means of a transparent epoxy vial lid and a HD video recording camera. Each test was repeated 3 times and the average values used for calculations. The impact factor, M, for each milling mode is given by

$$M= N_{imp}(t_r /t_m)(\text{impacts/rotation}) \quad (4\text{-}15)$$

where N_{imp} (impacts/rotation) is the number of impacts within t_m milling time and t_r is the time per one rotation of vial which equals 0.3 s for 200 rpm.

The visual examination reveals that in the IMP68-4B (Fig. 4.3a) and IMP68-2B (Fig. 4.3b) milling modes, impact and shearing are occurring at the magnet located at the 8 o'clock angular position and the second magnet (at 6 o'clock) is not involved directly in either shearing or impact. Therefore, the total milling energy which is calculated based on the experimental observations and theoretical analysis, is expressed by Eq. (4-16).

$$Q_T = MQ_i+N_sQ_s \ (\text{J/rotation}) \quad (4\text{-}16)$$

Substituting that one rotation takes 0.3s (8.333×10^{-5}h) the calculated values of total milling energy (Q_T) in (kJ/h) for several different milling modes are shown in Table 4.3.

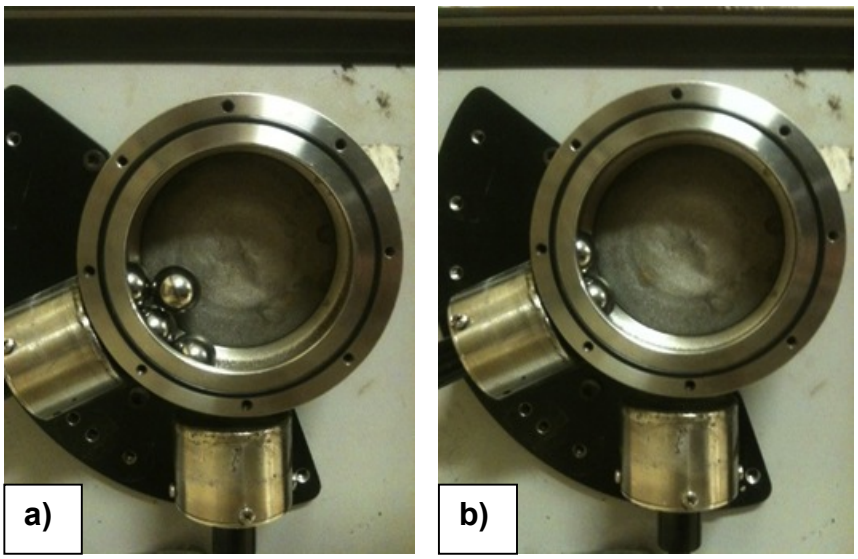

Fig. 4.3. Ball positions in the vial for a) IMP68-4B and b) IMP68-2B milling modes.

Table 4.3 calculated values of impact, shearing and total milling energy for several different milling modes.

Mode	N_{imp}	t_m(s)	M (Imp/rot)	N_s		Q_i (kJ/h)	Q_s (kJ/h)	Q_T (kJ/h)
				Magnet at 6 (WD=10mm)	Magnet at 8 (WD=2mm)			
LES6-2B	84	18	1.5	1	-	11.7	86.76	98.46
	80	16						
	76	14						
LES6-3B	100	17	1.67	1	-	13	86.76	99.76
	106	20						
	90	15						
LES6-4B	128	20	1.92	1	-	14.97	86.76	102.73
	200	30						
	108	18						
IMP68-2B	90	15	1.8	0	1	20.9	132.5	153.4
	120	20						
	120	20						
IMP68-4B	111	9	3.45	0	2	40.16	265	305.16
	162	15						
	138	12						

4.5. Mechanical energy conversion to heat

A considerable fraction of the total milling energy (Q_T) converts to heat and locally increases the temperature during ball milling. By measuring the inside temperature of vial during ball milling we can calculate the amount of energy converted to heat, Q, according to the following general relationship:

$$Q=\Delta T \times C_{material} \quad (4\text{-}17)$$

where ΔT is the temperature difference and $C_{material}$ is the heat capacity of a material (Table 4.1). Therefore, the total amount of heat produced during ball milling can be expressed in the following manner:

$$Q_{heat}=Q_{vial}+Q_{balls}+Q_{H2} \quad (4\text{-}18)$$

where Q_{vial}, Q_{balls} and Q_{H2} is the amount of heat which increases temperature of vial, balls and hydrogen gas inside the vial. Q_{H2} can be calculated from the well-known equation [127]:

$$Q_{N2} = \int_{T_0}^{T} n_{H2}\, Cv_{H2}\, dT \ (\Delta V = 0) \quad (4\text{-}19)$$

where n_{H2} is the number of moles H_2 and C_{VH2} is the thermal capacity of H_2 at a constant volume, which from Table 4.1 equals 0.116 mol and (3.33T+27.37) J/mol•°C, respectively. After substituting these values into Eq. (4-19), solving it and substituting the solution and other pertinent constant values from Table 1 into Eq. (4-18), one obtains :

$$Q_{heat} = 0.193\ (T^2-T_o^2)+2206.48\ (T-T_o)\ (J) \quad (4\text{-}20)$$

where Q_{heat} (J) is the necessary energy to increase the temperature from T_o to T (ΔT). As mentioned before, this energy is a fraction of the total milling energy Q_T. In order to estimate this fraction, the temperature changes inside the vial loaded with the

($LiNH_2$+0.7MgH_2) powder ball milled under IMP68-4B-R40 milling mode were measured. For this propose, the milling vial was fully insulated using a glass wool to keep the produced heat inside the vial. In each measurement, the temperature of three different points of the vial (bottom, middle and top) was measured by entering a NiCr-NiAl (chromel/alumel) thermocouple into the vial from a hole on the vial lid. Table 4.4 shows the values of total mechanical energy and measured heat energy at different milling time.

Table 4.4 experimental values of produced heat inside the vial during ball milling and the fraction of total energy converted to heat.

Milling time (min)	**T_o(°C)**	**T(°C)**	**Q_T (kJ)**	**Q_{heat} (kJ)**	**Fraction (%)**
1	23.7	24.6	4	2.09908971	52.47724
2	23.7	27.1	14	7.93153496	56.65382
3	23.7	29	24	12.36580683	51.5242
4	23.7	36.1	49	28.94831336	59.07819
5	23.7	38.4	73	34.32428391	47.01957
10	23.7	45	98	49.76231883	50.77788

According to these results, on average, at least approximately 53% of total mechanical energy Q_T converts to heat and the rest, that means 47% designated here as Q_P=0.47Q_T, is injected into the powder and consumed for powder

compressing, particle refining (breaking) and microstructural evolution. Since the mass of powder can be changed for each milling mode, it is convenient to express the injected energy, Q_P, as a normalized energy per unit mass of powder which is conveniently expressed by the ball-to-powder mass ratio, R, according to the following equation:

$$Q_{TR}=Q_P/m_R \text{ (kJ/gh)} \quad (4\text{-}21)$$

where m_R is the mass of powder corresponding to a constant ball-to-powder mass ratio, R. Table 4.5 shows the calculated values of the normalized energy, Q_P and corresponding Q_{TR} for various milling modes with a constant ball-to-powder mass ratio R.

Table 4.5 The amount of energy applied into the milling powder which varies by variation of ball to powder weight ratio (R).

Mode	Q_P(kJ/h)	Q_{R40} (kJ/gh)	Q_{R60} (kJ/gh)	Q_{R132} (kJ/gh)
IMP68-4B	143.4	22.1	33.3	72.8
IMP68-2B	72.1	11.1	16.8	36.6
LES6-4B	48.3	7.4	11.2	24.5
LES6-3B	46.9	7.2	11.0	23.8
LES6-2B	46.3	7.1	10.8	23.5

5. Li-N-Mg-H

5.1 The effects of molar ratio and ball milling energy on mechanical dehydrogenation of the ($LiNH_2$+nMgH_2) (n=0.5-2.0)

In general, it is very well documented that ball milling of metal/intermetallic alloys introduces a substantial refinement of their microstructure [126]. This is reflected in a profound size reduction of two principal parameters as mentioned earlier: the size of powder particles and the average size of grains (crystallites) residing within the ball milled powder particles. The research on ball milling of various hydrides and particularly MgH_2 shows that the structural changes observed to occur upon ball milling of hydrides, as reviewed in [6], are remarkably similar to those occurring in metal/intermetallic alloys. The rate of particle size refinement follows closely the rate of grain size refinement up to a certain saturation value [6].

For hydrides, the usual saturation level for an average particle size achieved after prolonged ball milling is about 1μm and it is hard to refine particle size below this value [6]. In contrast, the average size of grains residing within the hydride particles is refined very effectively to true nanometric levels. Customarily, the changes in particle/grain size of hydrides upon ball milling are plotted as a function of milling time as reported for $LiNH_2$ composited with LiH in [129]. However, since this approach does not take into account the mode of milling (number and size of balls, type of milling device etc.) it is correct for the comparative purposes only if the mode of milling remains the same. However, we can now express the changes of the grain size and lattice strain of $LiNH_2$ constituent in the ($LiNH_2$+nMgH_2) nano-composite as a function of one fundamental parameter which is the total injected energy of milling,

Q_{TR} (kJ/g), as shown in Table 5.1. The lattice strain is minimal and approximately constant so it can be neglected. The $LiNH_2$ grain size is plotted as a function of Q_{TR} in Fig. 5.1. It is clearly seen that the grain size decreases rapidly with increasing Q_{TR} reaching the size range 30-50 nm at the Q_{TR}=150-200 kJ/g and subsequently more or less saturates. To the best of our knowledge this type of grain size vs. milling energy plot has never been reported in the literature. It confirms the correctness of our semi-empirical approach for calculating the total energy of milling in chapter 4. It proves that a single energy parameter, Q_{TR}, can be effectively used for characterizing structural changes.

Table 5.1. The estimated grain size and lattice strain of $LiNH_2$ in the ($LiNH_2$+nMgH_2) composite as a function of total milling energy (kJ/g).

Hydride system/ball milling mode and time	Q_{TR}(kJ/g)	Grain size $LiNH_2$ (nm)	Strain (%)
As-received $LiNH_2$	0	200	0.06
$LiNH_2$-IMP68-R40-4B-25h	552	32	0.20
0.5MgH_2-IMP68-R40-4B-25h	552	21	0.42
0.7 MgH_2-LES6-R60-3B-21h	231	53	0.20
0.7 MgH_2-LES6-R132-3B- 21h	500	18	0.34
0.9 MgH_2-LES6-R60-4B-24h	269	14	0.12
0.9 MgH_2-IMP68-R60-4B-12h	400	20	0.40
1.0 MgH_2-LES6-R40-3B-25h	190	30	0.30
2.0 MgH_2-LES6-R40-3B-21h	151	35	0.49

Note: IMP-impact mode; LES-low energy shearing; B-number of steel balls, e.g. 4B=4 steel balls.

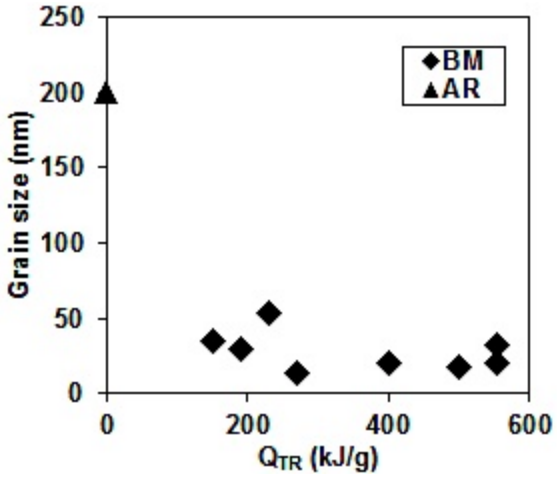

Fig. 5.1 The estimated grain size of $LiNH_2$ in the ($LiNH_2$+nMgH_2) composite as a function of total milling energy Q_{TR} (kJ/g) for n=0.5, 0.7, 0.9, 1.0 and 2.0. AR-as received, BM-ball milled (Adapted from [150]).

A typical example of the milling behavior for the molar ratios n=0.5 and 0.7 is shown in Fig. 5.2. It is observed that large quantities of H_2 are gradually released with increasing milling time (Fig. 5.2 a). However, Fig. 5.2 b clearly shows that the released H_2 quantity is a function of the milling energy injected into a powder, Q_{TR}. It is noticeable that the rate of H_2 release slightly differs depending on the molar ratio n of the mixture. For n=0.5 the H_2 release is slow in the beginning and then accelerates while it is approximately linear for n=0.7 H_2.

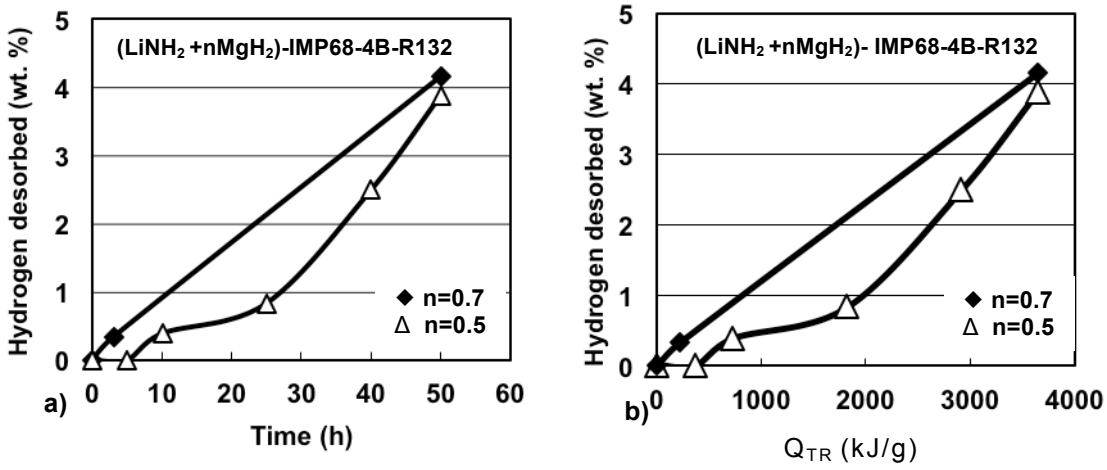

Fig. 5.2 Hydrogen desorbed during milling as a function of (a) milling time and (b) milling energy Q_{TR} for the molar ratio n=0.5 and 0.7 (Adapted from [150]).

The resulting microstructure after milling was investigated by X-ray diffraction (XRD) as shown in Fig. 5.3a and the Fourier Transform Infrared Spectroscopy (FTIR) as shown in Fig. 5.3b for the ($LiNH_2$+nMgH_2) mixture with n=0.5. For the FTIR technique the various phases appearing in the microstructure were identified on the basis of the wave numbers assigned to these phases found in various references dealing with the ($LiNH_2$-MgH_2) system, which are compiled in Table 5.2. Both Fig. 5.3a and b clearly show the evolution of microstructure during milling as a function of Q_{TR}. A low Q_{TR} (464 kJ/g) results in the formation of LiH with $LiNH_2$ and MgH_2 still present in the microstructure (Fig. 5.3a). However, the corresponding FTIR pattern reveals a small hump at around 3270 cm^{-1} wavelength indicating the formation of an amorphous $Mg(NH_2)_2$ hydride (a-$Mg(NH_2)_2$). Since it is amorphous it cannot be observed on the XRD pattern in Fig. 5.3a. With the Q_{TR} increasing to 1820 kJ/g the intensities of XRD peaks for MgH_2 are substantially reduced (Fig.5.3a) which indicates a gradual consumption of MgH_2 in reactions occurring during milling. The corresponding FTIR pattern clearly shows the formation of a new hydride $Li_2Mg(NH)_2$ whose volume fraction increases with Q_{TR} increasing to 3640 kJ/g after 50h of milling as evidenced by increased intensity of the $Li_2Mg(NH)_2$ peaks in Fig. 5.3a and b.

Similar observations of the microstructural evolution with increasing Q_{TR} were carried out by XRD and FTIR for the ($LiNH_2$+nMgH_2) mixture with n=0.7 which are shown in Fig. 5.4a and b. After injection of just 231 kJ/g milling energy the microstructure still consists of an original phase mixture $LiNH_2$ and MgH_2 as shown in the XRD patterns in Fig. 5.4a and in the FTIR patterns in Fig. 5.4b. After injecting of about 699 kJ/g of milling energy the peaks of LiH appear in Fig. 5.4a and the humps/peaks around

3190, 3271 and 3320 cm^{-1} appear in the FTIR pattern in Fig. 5.4b indicating the formation of both the a-$Mg(NH_2)_2$ and $Li_2Mg(NH)_2$ hydride phases. After injecting 1529 kJ/g of milling energy the XRD peaks for $Li_2Mg(NH)_2$ become more pronounced in Fig. 5.4a as well those in the FTIR pattern in Fig. 5.4b. It must also be pointed out that after 50h of milling which corresponds to Q_{TR}=3640 kJ/g the microstructure of the mixtures with n=0.5 and 0.7 is nearly identical as shown in an XRD pattern in Fig. 5.5. The n=0.7 mixture has slightly higher content of MgH_2 as shown by more intense peaks for MgH_2 in the XRD pattern in Fig.5.5. The identical microstructure agrees well with a nearly identical quantity of released H_2 as already shown in Fig. 5.2.

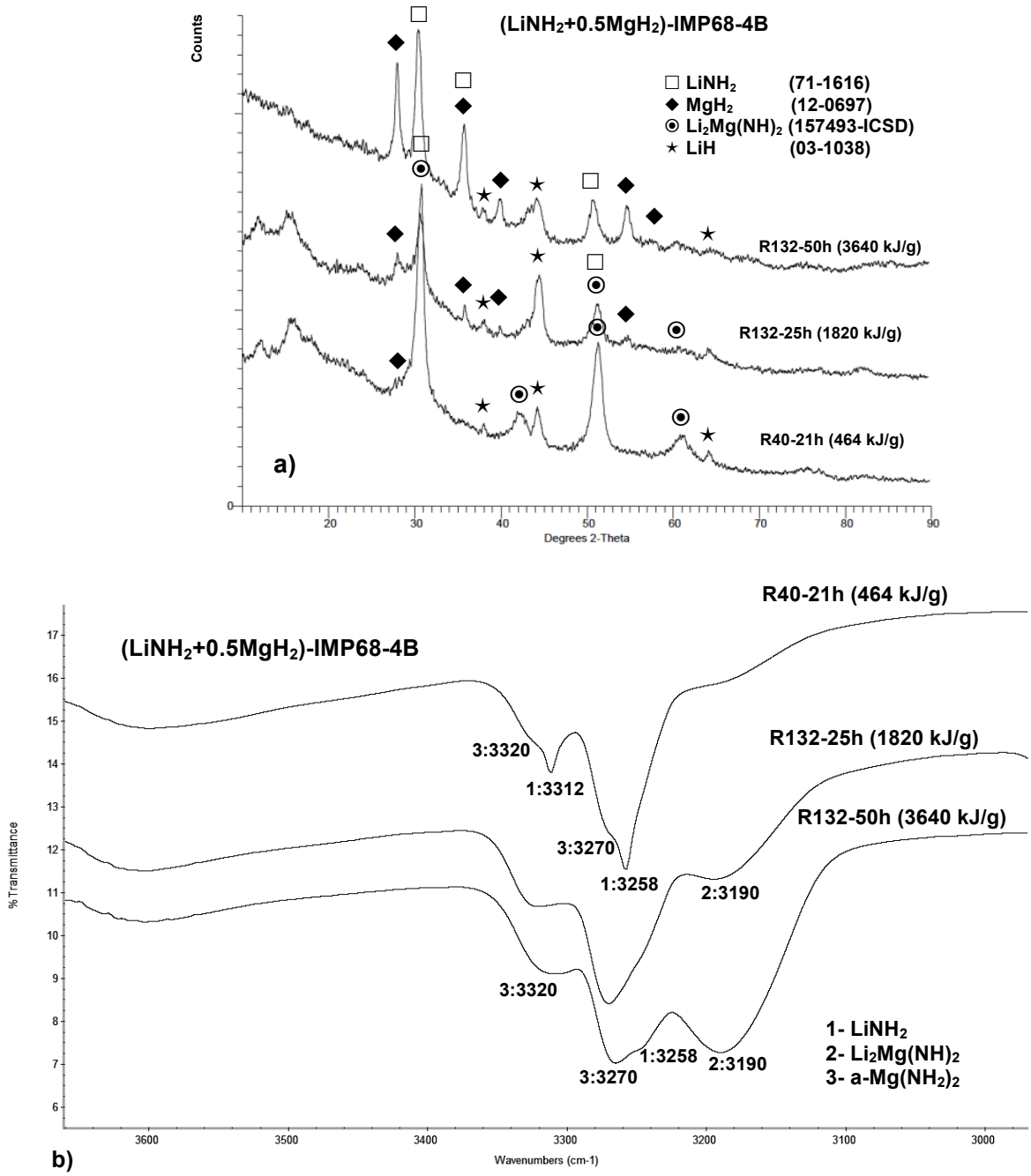

Fig. 5.3 (a) XRD patterns and (b) corresponding FTIR patterns for the ($LiNH_2$+nMgH_2) mixture with the molar ratio n=0.5 showing the evolution of microstructure as a function of the milling energy Q_{TR}. The humps around 2θ~17° in the XRD pattern arise from a Kapton film on the XRD holder (Adapted from [150]).

Table 5.2. FTIR wave numbers for hydrides in the ($LiNH_2$-MgH_2) system observed in the literature.

Hydride	Wave number (cm^{-1})	Reference
$LiNH_2$	3259/3313	[101]
	3259/3313	[130]
	3258/3313	[131]
	3313	[117]
	3259/3313	[104]
	3258/3312	[133]
	3258/3313	[135]
	3258/3312	[136]
Li_2NH	3162	[101]
	3162	[130]
	3162	[104]
a-$Mg(NH_2)_2$	3325	[101]
	3267	[130]
	3272/3326	[131]
	3272/3326	[117]
	3265	[106]
	3274/3326	[104]
	3271/3326	[132]
	3272/3326	[79]
	3272/3326	[133]
	3286/3332	[134]
	3271/3326	[135]
$Li_2Mg(NH)_2$	3150-3200 (broad peak)	[101]
	3174	[131]
	3173; 3174	[106]
	3160-3200 (broad peak)	[133]
	3174; 3170	[135]
	3163/3180; 3166; 3167	[136]
MgNH	3251; 3240; 3197	[101]
	3197	[130]
	3190	[117]
	3178	[106]
	3240; 3251; 3197	[104]
	3196	[132]
	3196	[79]
	3191; 3196	[136]
$Li_2Mg_2(NH)_3$	3163/3198	[117]
$Li_3Na(NH_2)_4$	3239/3295	[135]

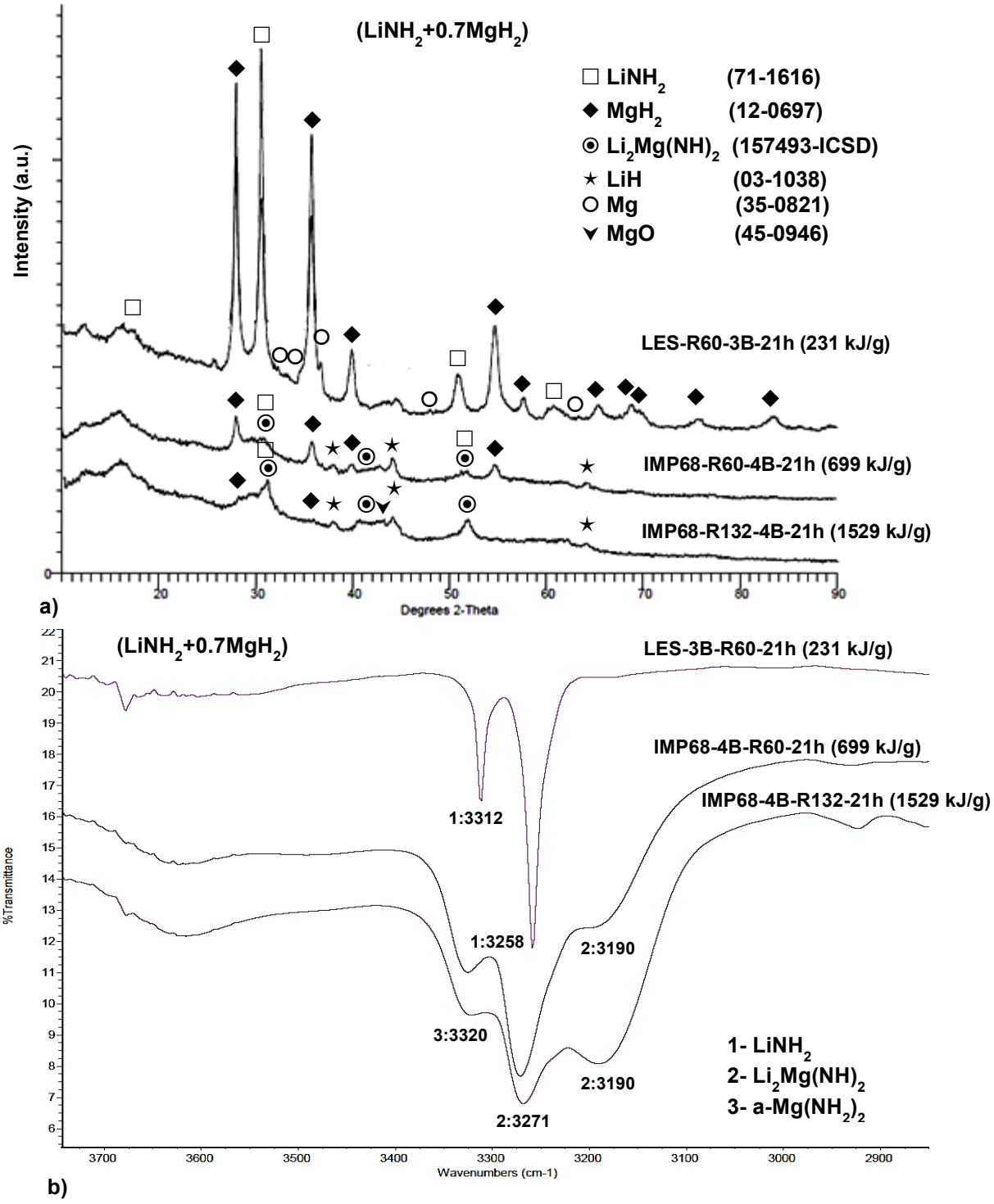

Fig 5.4 (a) XRD patterns and (b) corresponding FTIR patterns for the ($LiNH_2$+nMgH_2) mixture with the molar ratio n=0.7 showing the evolution of microstructure as a function of the milling energy Q_{TR} (Adapted from [150]).

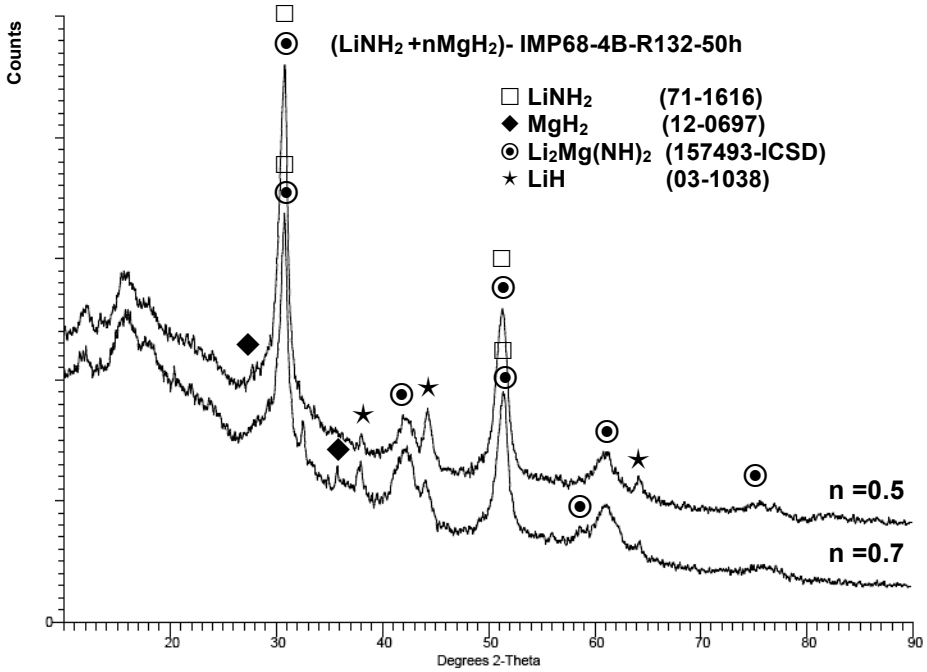

Fig.5.5 XRD patterns for the molar ratios n=0.5 and 0.7 after ball milling for 50h (Q_{TR}=3640 kJ/g) (Adapted from [150]).

However, an XRD pattern for the molar ratio n=0.5 in Fig. 5.3a shows a small peak for MgH_2 still remaining after milling with Q_{TR}=3640 kJ/g (50h) and the corresponding quantity of H_2 desorbed is 4 wt.% (Fig. 5.2). That suggests that any possible reaction of MgH_2 leading to the formation of a new $Li_2Mg(NH)_2$ hydride phase is incomplete. In order to confirm this hypothesis the n=0.5 and 0.7 mixtures ball milled for 50h (Q_{TR}=3640 kJ/g) were isothermally desorbed at 190 and 125°C as shown in Fig. 5.6a and b, respectively. It is clearly seen that the ball milled n=0.5 mixture released isothermally about 1.2 wt.% H_2 which together with 4 wt.% already released during ball milling (Fig. 5.2) makes a total of about 5.2 wt.% H_2. In contrast, the ball milled n=0.7 mixture released isothermally about 0.5 wt.% H_2 for the total of about 4.5 wt.% H_2. Fig. 5.6c shows an XRD pattern for the n=0.5 mixture after desorption at 190°C

compared to a ball milled (BM) pattern. It is clearly seen that after thermal desorption the microstructure primarily consists of a new hydride $Li_2Mg(H)_2$. The peaks of Li_2O and MgO are also seen that could result from an unintentional exposure to air during handling of thermally desorbed powder (e.g. a commercial MgH_2 powder frequently contains some remnants of Mg as can be seen in Fig. 8a that can easily oxidize). A weak remnant (200) 100% intensity peak of LiH is also observed at $2\Theta=44.3°$ in Fig. 5.6c which indicates that LiH was not fully consumed in reaction which led to the formation of $Li_2Mg(H)_2$.

The release of H_2 from the n=0.5 mixture ball milled for 50h (Q_{TR}=3640 kJ/g) is also confirmed by a DSC test shown in Fig. 5.7a. A strong endothermic peak related to H_2 release is clearly observed at around 195°C which correlates very well with the isothermal H_2 desorption curve at 190°C in Fig. 5.6a. Fig. 5.7b shows XRD patterns after thermal sectioning at various temperatures during a DSC test (a test was stopped at temperatures delineated by vertical lines in Fig. 5.7a). It is clear that with temperature increasing to 140 and 220°C there is a gradual disappearance of the LiH peaks and the sharpening of the $Li_2Mg(H)_2$ peaks which is accompanied by a continuous release of H_2. That means that LiH is gradually consumed in reaction leading to the formation of $Li_2Mg(H)_2$ and H_2. Since after ball milling LiH always accompanies a-$Mg(NH_2)_2$ as discussed earlier, there must have occurred reaction between LiH and a-$Mg(NH_2)_2$ to form $Li_2Mg(H)_2$. Fig. 5.7b also shows that there is a change in the character of reaction above 300°C since the XRD pattern at 350°C shows the presence of Mg_3N_2 and a smaller H_2 release peak appears in a DSC pattern around 300°C (Fig. 5.7a). However, since this reaction occurs at high

temperatures it has no practical meaning and will not be discussed here. Furthermore, Fig.5.8 shows DSC curves for the n=0.5 mixture without any ball milling at two heating rates. They show two separate peaks at temperatures above 350°C which correspond to dehydrogenation of MgH_2 and $LiNH_2$, respectively, in the unmilled mixture. These DSC traces are completely different than the ones in Fig. 5.7a for ball milled powders.

For the sake of clarity, it must be pointed out that the preliminary identification of the $Li_2Mg(H)_2$ hydride phase in the present work has been based on information found in the literature and the XRD file 157493-ICSD. However, for the exact identification of the XRD peaks of $Li_2Mg(H)_2$ we have used 2Θ values collected from XRD patterns in Fig. 5.4a (1529 kJ/g), Fig. 5.5 (n=0.7 pattern) and Fig. 5.7b (350°C pattern) which are listed in Table 5.3 and compared with the data from 157493-ICSD. Table 5.3 contains the most exhaustive set of data collected in this work for an unambiguous identification of $Li_2Mg(H)_2$.

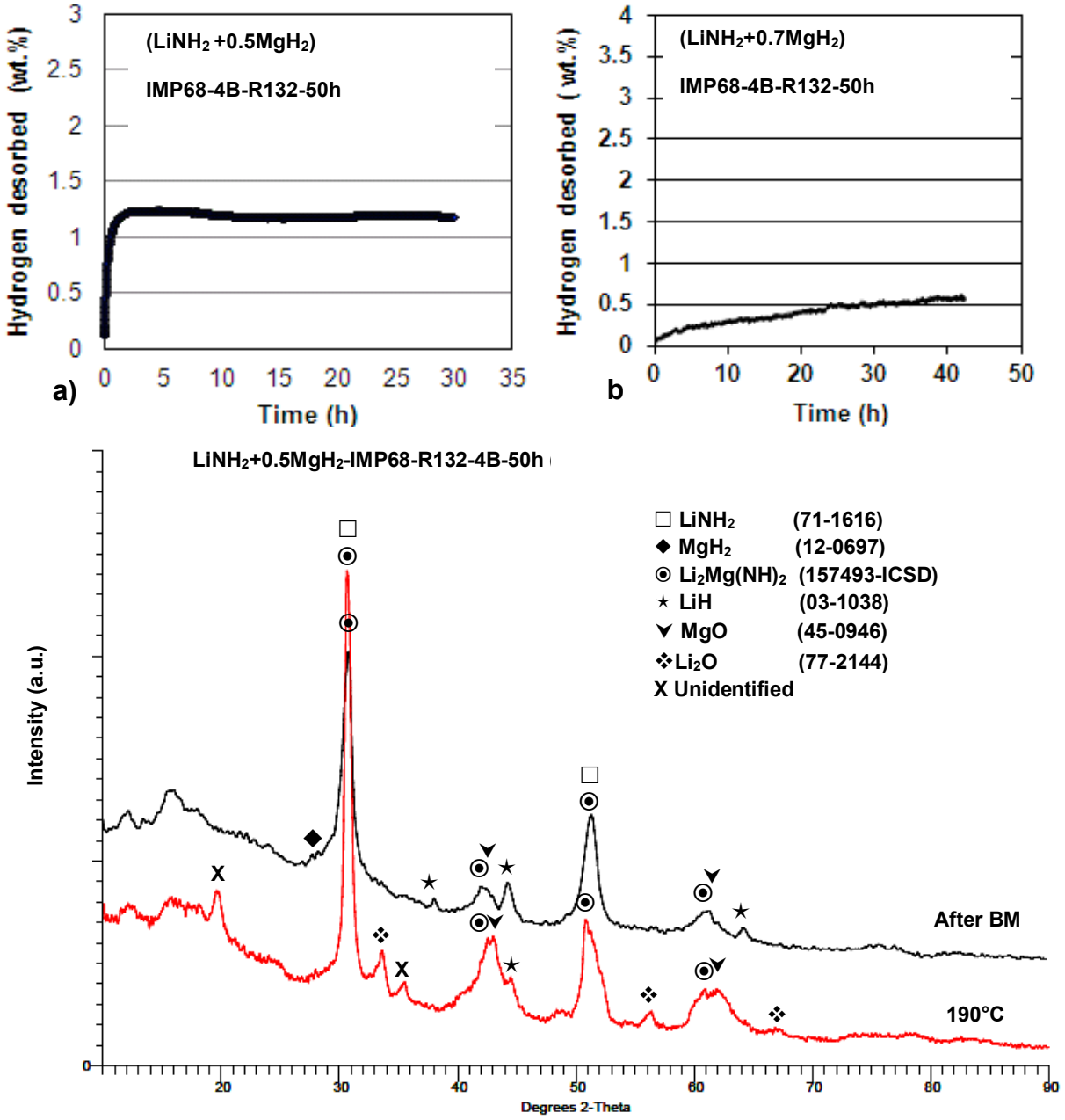

Fig 5.6 Thermal H_2 desorption at 190°C for 50h ball milled (a) ($LiNH_2$+0.5MgH_2) and (b) ($LiNH_2$+0.7MgH_2). (c) XRD patterns after thermal desorption as compared to the XRD pattern after ball milling (Q_{TR}=3640 kJ/g)) (Adapted from [150]).

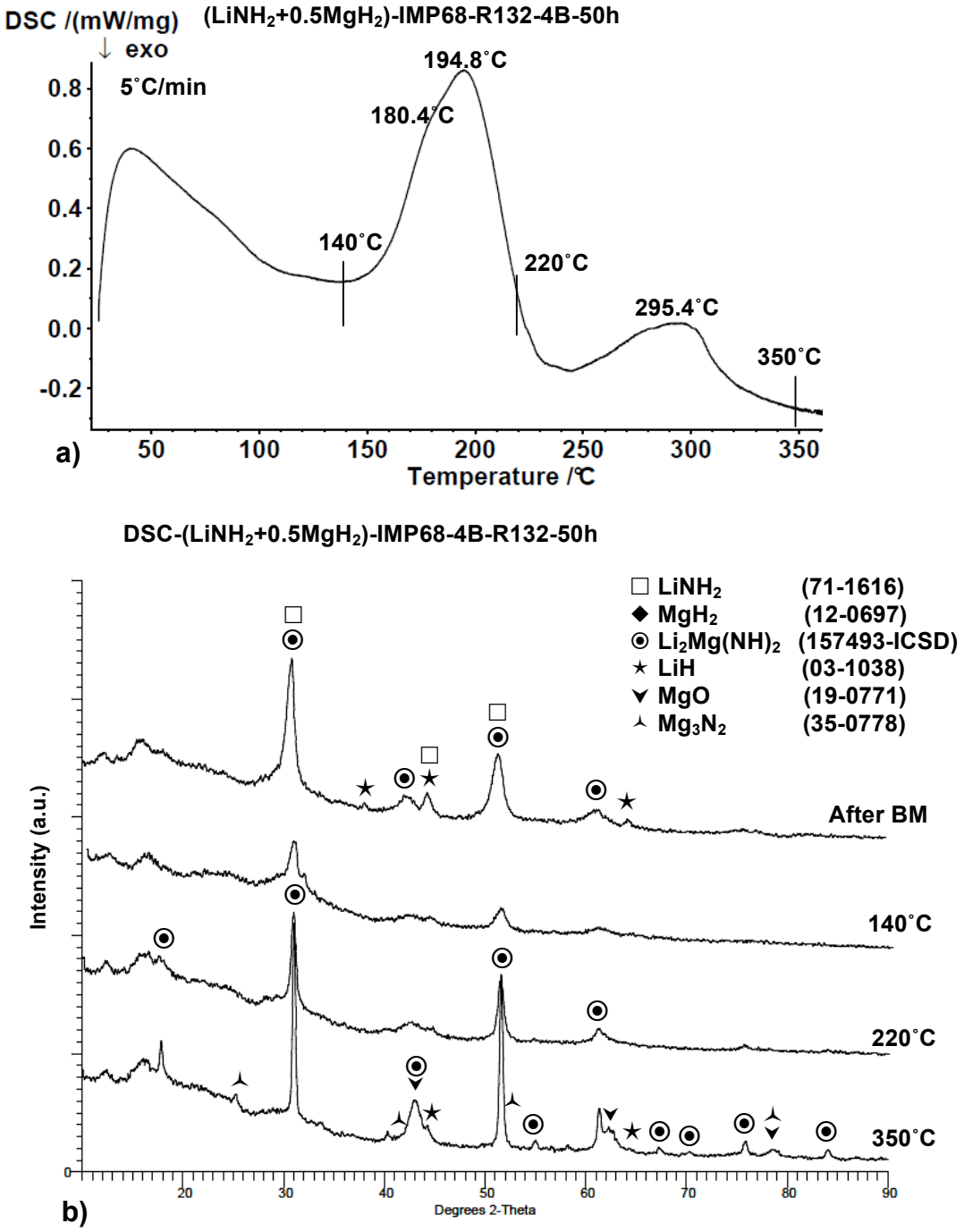

Fig 5.7 (a) DSC curve for 50h ball milled ($LiNH_2$+0.5MgH_2) (Q_{TR}=3640 kJ/g) and (b) corresponding XRD patterns taken at temperatures indicated by vertical lines (Adapted from [150]).

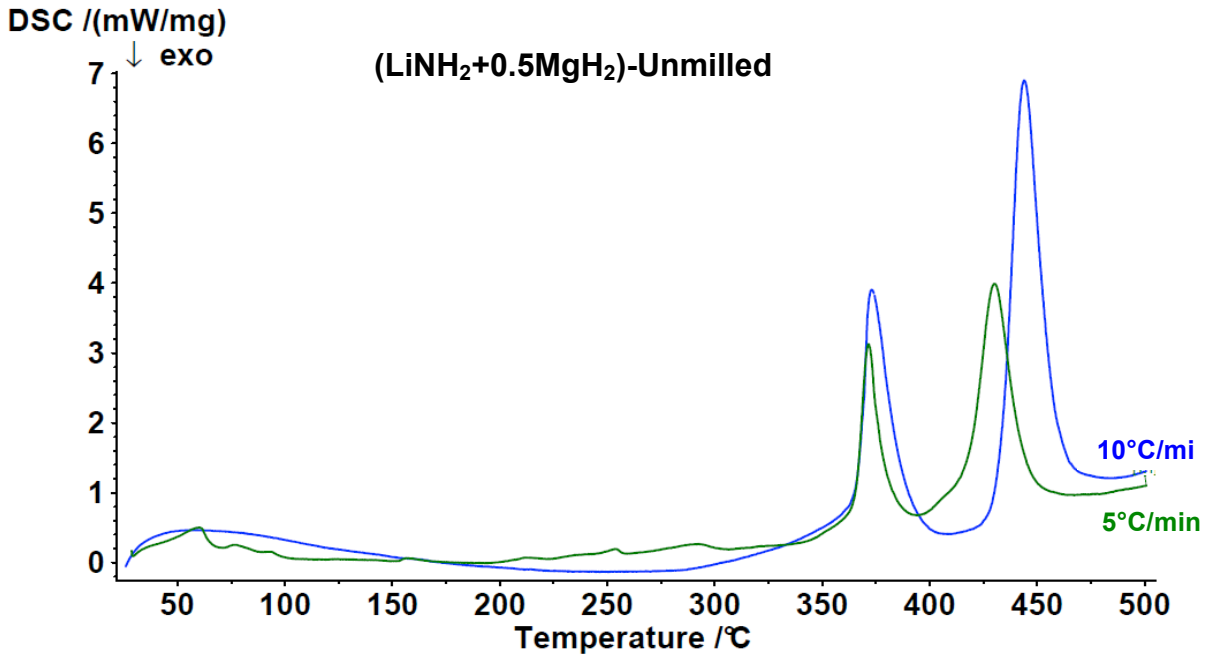

Fig 5.8 DSC curves for the unmilled mixture ($LiNH_2$+0.5MgH_2) at two heating rates.

Table 5.3. Diffraction peak 2θ positions for the unambiguous identification of $Li_2Mg(H)_2$ in this work as compared to the XRD (157493-ICSD) file.

Phase	Experimental			(157493-ICSD)		
	Intensity (%)	2θ (deg)	d (hkl) (Å)	2θ (deg)	Intensity (%)	(hkl)
$Li_2Mg(NH)_2$	15	17.84	4.969	17.917	2.6	200
	1	19.84	4.472	19.907	7	110
	100 100	31.02 31.21	2.881 2.863	30.640	100	211
	14	42.16	2.142	41.074	1.4	121
	88 52	51.60 51.90	1.770 1.760	50.797 52.012	19 17	402 420
	4	54.97	1.669	54.054	1	222
	3	60.97	1.518	61.359	5	231
	2 (50h-190°C) 12	60.97 61.30	1.522 1.511	61.359	5	231
	3	67.26	1.391	67.342	1.4	132
	8	70.25	1.339	70.498	0.15	431
	7	75.85	1.253	75.852	0.5	114
	9	84.04	1.151	-	-	-

We also extended investigations to higher molar ratios. Fig. 5.9a,b show H_2 release during ball milling of the ($LiNH_2$+0.9MgH_2) mixture under two differing milling modes which result in the same quantity of injected energy Q_{TR}= 450 kJ/g. Ball milling under an IMP68 (high energy impact) mode released a small total quantity of ~0.5 wt.% H_2 while ball milling under a LES6 mode (low energy shearing) didn't release any measurable quantity of H_2. Apparently, at small levels of Q_{TR} it is possible that the more energetic mode of milling could lead to a small release of hydrogen as compared with a low energy mode despite that the final quantity of injected energy Q_{TR}=450 kJ/g is the same. However, the difference in behavior is very minimal. The XRD patterns in Fig. 5.9c confirm the formation of LiH and as such also the presence of a-$Mg(NH_2)_2$ after ball milling under an IMP68 mode and a small H_2 release also indicates formation of a small amount of $Li_2Mg(NH)_2$ from reaction between LiH and a-$Mg(NH_2)_2$.

Fig. 5.10a shows the H_2 release observed during ball milling of the high molar ratio ($LiNH_2$+2.0MgH_2) mixture. The maximum quantity of H_2 recorded is 2.9 wt.% after injection of Q_{TR}=464 kJ/g. Fig. 5.10b shows the XRD patterns corresponding to the evolution of microstructure with increasing Q_{TR}. It is clear that the primary phase, at this high molar ratio n=2, is MgNH. This phase was preliminarily identified based on information from the literature [117, 106, 132, 79] but more refined identification was obtained from the 2θ peak positions collected in Table 5.4 from the XRD pattern in Fig. 5.10b which shows very well developed MgNH peaks. The presence of MgNH is additionally confirmed by FTIR in Fig. 5.10c identified according to the data set in Table 5.2.

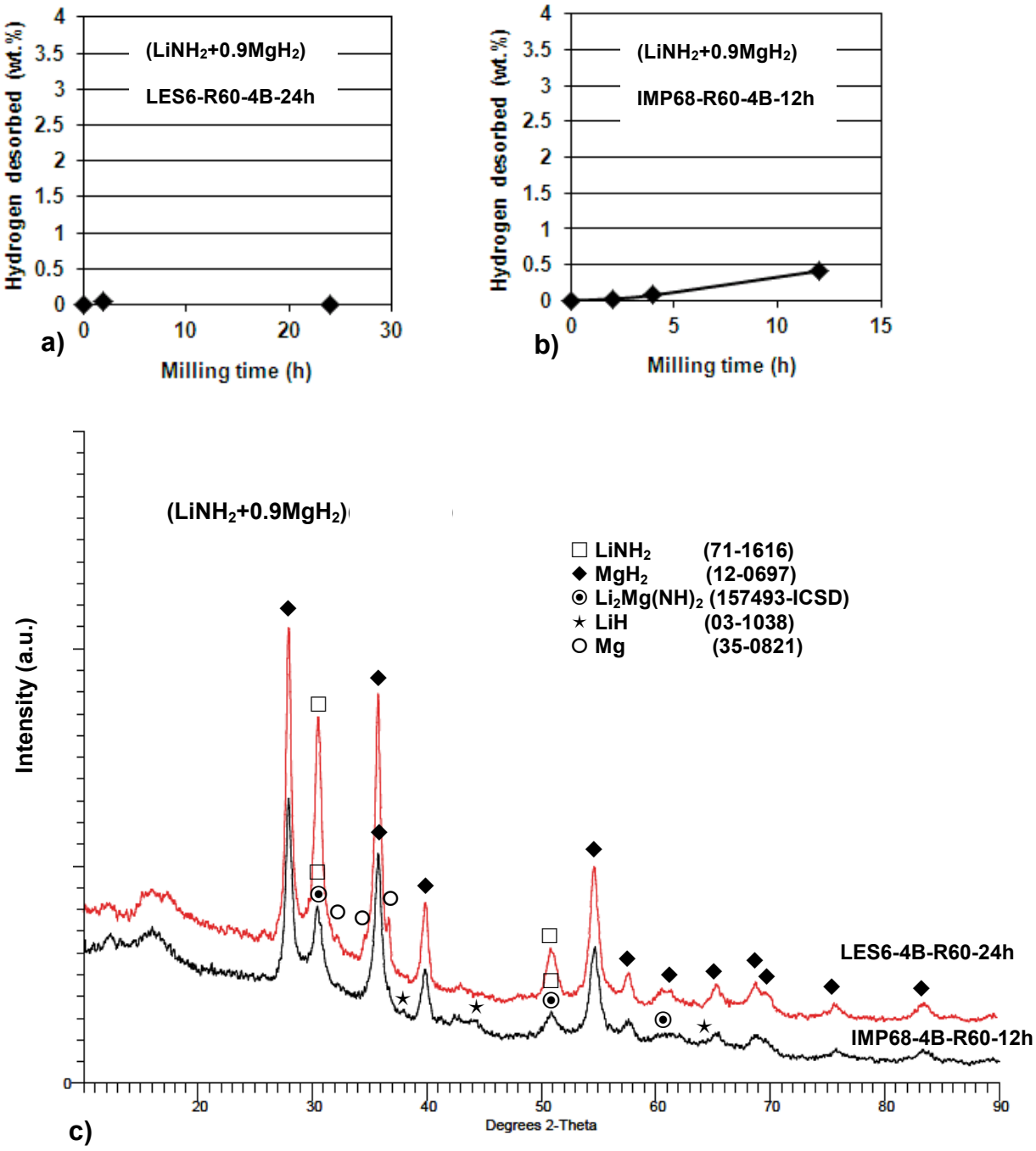

Fig.5.9 Observed H_2 release during ball milling under (a) IMP68 high energy mode and (b) LES6 low energy shearing mode which result in the same total injected milling energy (Q_{TR}=450 kJ/g) XRD patterns after high and low energy ball milling (Adapted from [150]).

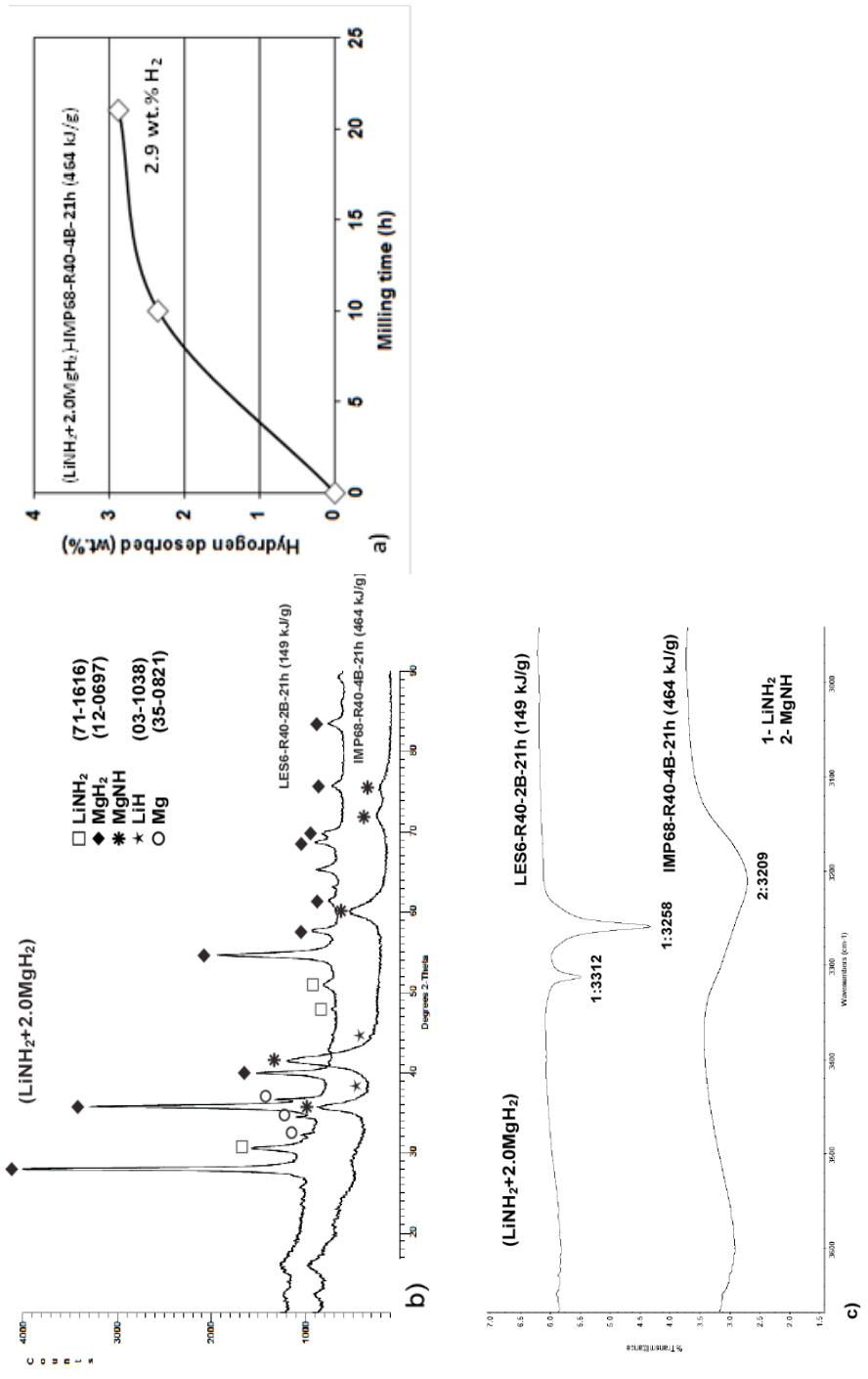

Fig 5.10 (a) Observed H_2 release during ball milling of high molar ratio mixture ($LiNH_2$+2.0MgH_2) and corresponding (b) XRD patterns and (c) FTIR patterns (Adapted from [150]).

Table 5.4. Diffraction peak 2Θ positions for the unambiguous identification of MgNH in this work.

Phase	Intensity (%)	2θ (deg)	$d_{(hkl)}$ (Å)
MgNH	73	35.73	2.513
	100	41.40	2.178
	45	60.03	1.540
	20	72.00	1.311
	18	75.47	1.259

Based on the above microstructural evolution revealed by the XRD and FTIR studies it is clear that the following reactions occur with increasing the total milling energy (Q_{TR}) injected into a powder for the molar ratios n=0.5-0.9 (or in general n<1.0):

$LiNH_2+nMgH_2 \rightarrow 0.5a\text{-}Mg(NH_2)_2+1.0LiH+(n-0.5)MgH_2$ (no H_2 release) (5.1)

$0.5a\text{-}Mg(NH_2)_2+1.0LiH+[(n-0.5)MgH_2] \rightarrow 0.5Li_2Mg(NH)_2+1.0H_2+[(n-0.5)MgH_2]$ (max. 5.6 wt.% H_2) (5.2)

A square bracket represents a retained phase that does not take part in mechano-chemical reaction. At a lower total milling energy Q_{TR} mechano-chemically induced reaction (5.1) during ball milling leads to the formation of two new hydrides, LiH and $a\text{-}Mg(NH_2)_2$ but without any hydrogen release. Further increase of injected energy triggers reaction (5.2) in which the hydrides previously formed in reaction (5.1) start reacting with one another forming a new hydride $Li_2Mg(NH)_2$ which is accompanied by a release of H_2. Also, the above reactions show that with increasing n, more and more of retained (unreacted) MgH_2 should remain in the microstructure. Apparently,

reaction (5.2) must occur, at least partially, in order to observe a release of H_2 during ball milling as shown in Fig. 5.2.

For n≥1 the first reaction during milling is (5.1). Then with increasing milling energy another reaction has been identified which produces a completely new hydride MgNH:

$$0.5a\text{-}Mg(NH_2)_2+0.5MgH_2+[(n\text{-}1)MgH_2]+[1.0LiH]\rightarrow 1.0MgNH+1.0H_2\mathbf{+}[(n\text{-}1)MgH_2]+[1.0LiH] \quad (\text{max } 4.1 \text{ wt.\% } H_2) \qquad (5\text{-}3)$$

Again, a square bracket represents a retained phase that does not take part in mechano-chemical reaction. Table 5.5 shows a summary of milling modes for various molar ratios for the ($LiNH_2$+nMgH_2) mixtures, corresponding values of the total injected milling energy (Q_{TR}), observed hydrogen release (if any) during ball milling (BM) and the hydride phases identified by XRD and FTIR.

Table 5.5 Summary of milling modes for various molar ratios for the ($LiNH_2$+nMgH_2) mixtures, total injected milling energy, observed hydrogen release (if any) during ball milling (BM) and the phases identified by XRD and FTIR. R-ball-to-powder mass ratio.

n	Milling mode	R	BM time (h)	$Q_{TR(R)}$ (kJ/gh)	Q_{TR} (kJ/g)	wt. %H_2 BM	Hydride phases observed after BM
0.5	IMP68-4B	40	21	22.1	464.1	0	$LiNH_2$, MgH_2, LiH, a-$Mg(NH_2)_2$
		60		33.3	699.3	0.4	$LiNH_2$, MgH_2, LiH, a-$Mg(NH_2)_2$, $Li_2Mg(NH)_2$
		132		72.8	1528.8	1.1	$LiNH_2$, MgH_2, LiH, a-$Mg(NH_2)_2$, $Li_2Mg(NH)_2$
		40	25	22.1	552.5	0	$LiNH_2$, MgH_2, LiH, a-
		132	25	72.8	1820	0.88	$LiNH_2$, MgH_2, LiH, a-$Mg(NH_2)_2$, $Li_2Mg(NH)_2$
		132	50	72.8	3640	3.9	$LiNH_2$, MgH_2, LiH, a-$Mg(NH_2)_2$, $Li_2Mg(NH)_2$
0.7	IMP68-4B	40	21	22.1	464.1	0	$LiNH_2$, MgH_2, LiH, a-$Mg(NH_2)_2$
		60		33.3	699.3	0.9	$LiNH_2$, MgH_2, LiH, a-$Mg(NH_2)_2$, $Li_2Mg(NH)_2$
		132		72.8	1528.8	3	$LiNH_2$, MgH_2, LiH, a-$Mg(NH_2)_2$, $Li_2Mg(NH)_2$
		40	25	22.1	552.5	0.5	$LiNH_2$, MgH_2, LiH, a-$Mg(NH_2)_2$, $Li_2Mg(NH)_2$
		132	50	72.8	3640	4.1	$LiNH_2$, MgH_2, LiH, a-$Mg(NH_2)_2$, $Li_2Mg(NH)_2$
	IMP67-4B	40	25	20.8	513	0.29	$LiNH_2$, MgH_2, LiH, a-$Mg(NH_2)_2$, $Li_2Mg(NH)_2$
	LES6-3B	40	21	7.4	155.4	0	$LiNH_2$, MgH_2
		60		11	231	0	$LiNH_2$, MgH_2
		132		23.8	499.8	0	$LiNH_2$, MgH_2, LiH, a-$Mg(NH_2)_2$
0.85	LES6-4B	60	25	11.2	280	0	$LiNH_2$, MgH_2, LiH, a-$Mg(NH_2)_2$
0.9	IMP68-4B	60	12	33.3	399.6	0.4	$LiNH_2$, MgH_2, LiH, a-$Mg(NH_2)_2$, $Li_2Mg(NH)_2$
	LES6-4B	60	24	11.2	268.8	0	$LiNH_2$, MgH_2
1.0	IMP67	40	1	20.8	20.8	0	$LiNH_2$, MgH_2
			4		83.2	0	$LiNH_2$, MgH_2, LiH, a-$Mg(NH_2)_2$
			6		124.8	NA	MgH_2, LiH, a-$Mg(NH_2)_2$, MgNH
			25		513	1.9	LiH, a-$Mg(NH_2)_2$, MgNH
	LES6-3B	40	21	7.2	151.2	0	$LiNH_2$, MgH_2
1.5	IMP67	40	1	20.8	20.8	0	$LiNH_2$, MgH_2
			4		83.2	0	$LiNH_2$, MgH_2,
			6		124.8	NA	MgH_2, LiH, a-$Mg(NH_2)_2$, MgNH
			25		513	3	a-$Mg(NH_2)_2$, LiH, MgNH
2.0	IMP68-4B	40	21	22.1	464.1	2.9	a-$Mg(NH_2)_2$, LiH, MgNH
	LES6-3B			7.2	151.2	0	$LiNH_2$, MgH_2
	LES6-2B			7.1	149.1	0	$LiNH_2$, MgH_2

Based on the data collected in this table we managed to establish a preliminary hydride phase-milling energy diagram (map) for various levels of injected milling energy, Q_{TR}, and molar ratios as shown in Fig. 5.11. The symbols indicate the presence of an initial phase mixture or a newly formed hydride phase either alone or in a mixture with the others. The numbers indicate all phase mixtures present after passing a particular energy level line E_1 or E_2.

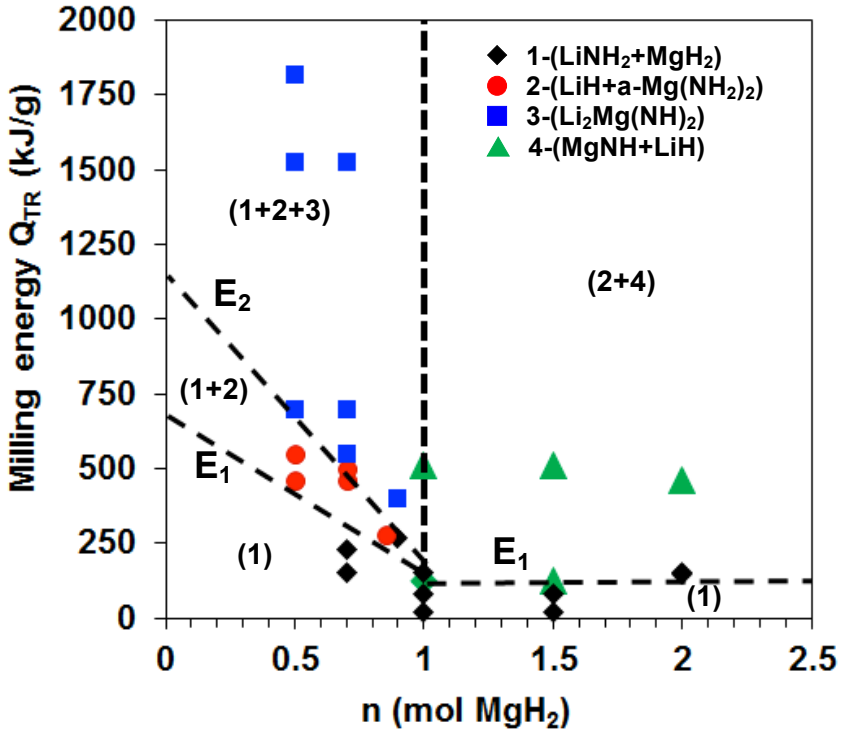

Fig 5.11 Milling energy-phase diagram for the ($LiNH_2$+nMgH_2) system for various molar ratios n=0.5, 0.7, 0.85, 0.9, 1.0 and 2.0. The lines E_1 and E_2 indicate approximate minimum energy levels at which a new hydride phase or the hydride phase mixtures appear during high energy ball milling. The thick vertical broken line delineates the phase fields for n <1.0 and n ≥1.0 (Adapted from [150]).

For all molar ratios n <1.0 the new hydride phases a-$Mg(NH_2)_2$ and LiH start forming at the injected milling energy levels delineated by the line E_1 as described by reaction (5-1). With increasing level of injected milling energy, when it reaches approximately the line E_2, the third new hydride phase, $Li_2Mg(NH)_2$, is formed according to reaction (5-2). However, it must be pointed out that even at the injected energy levels approaching 3640 kJ/g (beyond the energy scale in Fig. 5.11), Fig.5.3, 5.5, 5.6 and 5.7 clearly show that the small quantities of unreacted initial hydride phases such as $LiNH_2$ and MgH_2 still remain in the ball milled microstructure as shown by a phase field (1+2+3). This novel results which has never been reported in the literature clearly shows that for the molar ratios n <1.0, depending on the level of milling energy, the microstructure of powders can be a very complex mixture of various hydride phases, mechanically reacted and still unreacted.

For the molar ratios n ≥1.0, when the injected milling energy passes through the line E_1, the fourth new hydride phase, MgNH, is formed according to reaction (5-3) which requires 0.5 mol of retained MgH_2 already formed from reaction (5-1). However, the mechanical energy input required for the formation of MgNH is rather small. Usually, the MgNH phase exists in a mixture with yet unreacted remnants of LiH and a-$Mg(NH_2)_2$.

Apparently, the above reactions complicate to a large extent interpretation of results published so far on the isothermal dehydrogenation of the ball milled ($LiNH_2$+nMgH_2) composites since their initial structure could have varied widely. Another complicating factor is that the reactions may not come to the completion even after injecting a large energy and hence, mixtures of more than two phases can also exist after ball milling.

All this should be carefully taken into account when analyzing dehydrogenation/rehydrogenation behavior of the ball milled ($LiNH_2$+nMgH_2) nano-composites with varying n values. Furthermore, if the mechanical dehydrogenation phenomenon is left unaccounted for in one of the hydride composite systems discussed above, it will lead to grossly underestimated results of subsequent H_2 thermal desorption which, in turn, could lead to erroneous interpretation of the desorption phenomena/reaction paths.

5.2. The effects of the KH and NaH additives on the dehydrogenation and rehydrogenation behavior of ($LiNH_2$+0.5MgH_2)

In order to increase the surface area of particles and mechanically activate them, the starting chemical compounds, $LiNH_2$ and MgH_2, were pre-ball milled (PBM) for 24 and 2h, respectively, under the IMP68-4B milling mode. For MgH_2 high energy ball milling for 2h is sufficient to obtain a saturation of a particle at about 1μm and grain size about ?? [6]. Fig.5.12 shows the effect of pre-ball milling on the dehydrogenation rate of ($LiNH_2$+0.5MgH_2) at 125°C compared to the nanocomposites which were ball milled under the same milling energy. It is obvious that mechanical treatment on the starting hydrides can improve the kinetics of dehydrogenation reaction compared to just mixing powders by hand (Mix).

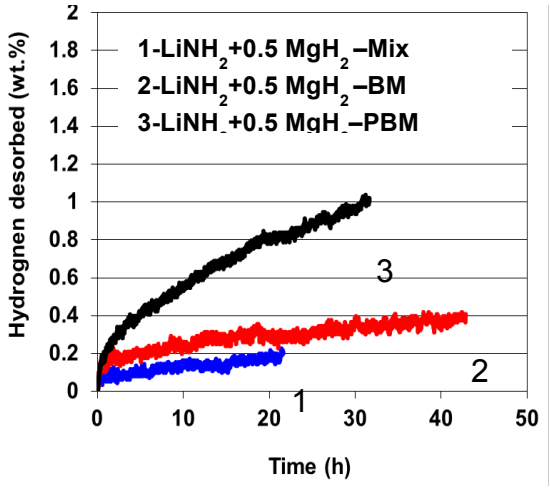

Fig.5.12. A comparison of volumetric dehydrogenation curves at 125°C for the $LiNH_2$+0.5MgH_2 mixture of as mixed hydrides compared to milled (BM) (IMP68-4B R40 25) (Q_{TR40}=552.5 kJ/g). and pre-ball milled (PBM) (LES6-4B R132 15min (Q_{TR}=6.13 kJ/g)) $LiNH_2$+0.5MgH_2.

In order to study the effect of pre ball milling and addition of 5 wt.% KH and NaH on the phase transformations and subsequent thermal behavior of the ($LiNH_2$+0.5MgH_2) system the mixtures of ($LiNH_2$+0.5MgH_2), (BM-($LiNH_2$+0.5MgH_2)+5 %wt. KH) and (PBM-($LiNH_2$+0.5MgH_2)+5%wt. KH/NaH) were subsequently ball milled using a high (IMP68-4B R40 25h) energy milling mode for BM samples and a low (LES6-4B R132 15min) energy milling mode for a PBM sample. These systems did not show any mechanical dehydrogenation during ball milling.

The dehydrogenation behavior was investigated at low and high temperature (125 and 200°C) under 0.1 MPa H_2 (atmospheric pressure). The pertinent dehydrogenation curves are shown in Fig 5.13 a-b.

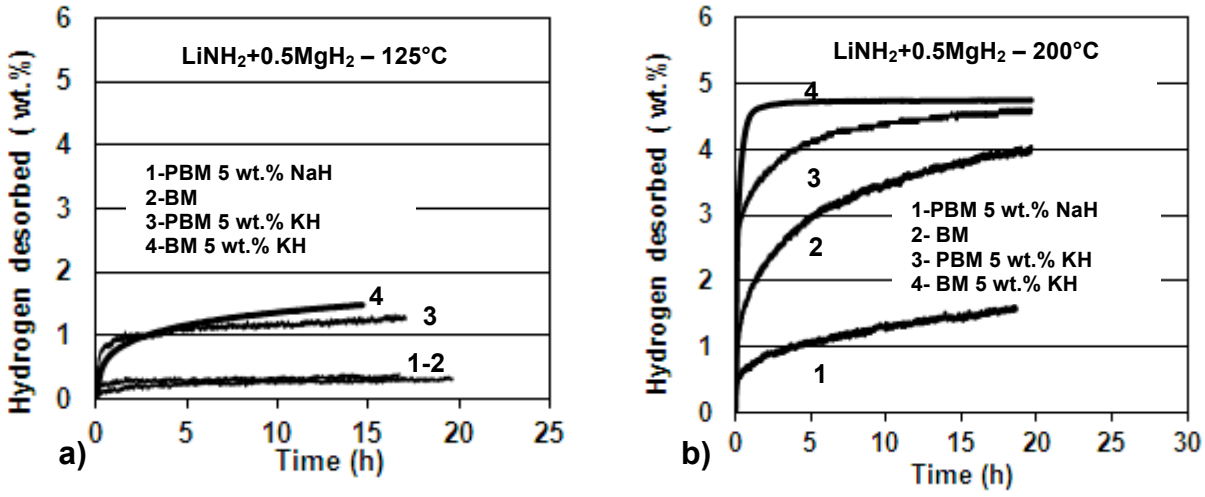

Fig. 5.13. A comparison of volumetric dehydrogenation curves for (BM-($LiNH_2$+0.5MgH_2),(BM-($LiNH_2$+0.5MgH_2)+5wt.%KH), (PBM($LiNH_2$+0.5MgH_2)+ 5wt.%KH) and (PBM($LiNH_2$+0.5MgH_2)+5wt.%NaH) systems at a) 125°C and b) 200°C. Ball milled at IMP68-4B R40 25h (Q_{TR}=552.5 kJ/g).

It is clear in Fig 5.13a that the undoped system (BM-($LiNH_2$+0.5MgH_2)) is able to desorb around 0.5 wt% at 125°C within 15 h, while addition of 5 wt% KH increases desorption kinetics measurably, since ~1.3 wt% H_2 desorbs within the same time. In contrast to KH, NaH does not have a significant effect on hydrogen desorption rate at 125°C. The system with NaH can release ~ 0.4 wt.% H_2 at 125°C after 15 h, which is similar to the nanocomposite without any additive.

A comparison of the desorption curves of the PBM and BM samples containing KH in Fig. 5.13a clearly shows that PBM does not improve the desorption kinetics at 125°C as already observed for the sample without KH (see Fig. 5.12))

By increasing temperature to 200°C dehydrogenation rate increases and the (BM-($LiNH_2$+0.5MgH_2) system desorbs ~3.7 wt.% H_2 within 15 h while the system with KH desorbs 4.8 wt.% H_2. It is also clear in Fig. 5.13 b that PBM for samples containing KH reduces desorption rate at 200°C as compared to the BM samples in contrast to

no improvement of dehydrogenation rate for PBM samples at 125°C containing KH in Fig. 5.13a. Similarly to dehydrogenation at 125°C, at 200°C NaH does not influence the dehydrogenation kinetics significantly and the sample desorbs 1.5 wt% H_2 within 15 h.

In order to understand the nature of the reactions occurring during dehydrogenation, the composite powder samples after completion of each isothermal dehydrogenation were taken for an XRD test and the obtained patterns for the (PBM-($LiNH_2$+0.5MgH_2)+5wt.% KH) system are shown in Fig. 5.14. It can be seen that the ball milled (BM) mixture shows the Bragg peaks of the principal constituents $LiNH_4$, MgH_2 and KH. The lack of any new Bragg peaks due to the formation of some new phases clearly indicates that no reactions between the hydrides occurred during ball milling.

With increasing dehydrogenation temperature from 125 to 200°C, a gradual reduction in the intensity of the principal diffraction peaks for $LiNH_4$, MgH_2 and KH and formation of some new phases are clearly visible in Fig. 5.14.

The XRD pattern of the (PBM-($LiNH_2$+0.5MgH_2)+5wt.% KH) sample, dehydrogenated at 125 and 160°C contains quite strong peaks of $Li_2Mg(NH)_2$, and weak peaks of a new phase identified as $K_2Mg(NH)_2$. In the pattern taken after dehydrogenation at 200°C the KH diffraction peaks are nearly invisible which means that KH has been consumed in one or several reactions. The XRD pattern in Fig.5.14 at 200°C contains the peaks of LiH, $Li_2Mg(NH)_2$ and the weak peaks of new phases identified as $K_2Mg(NH)_2$, KMgN and KN_3.

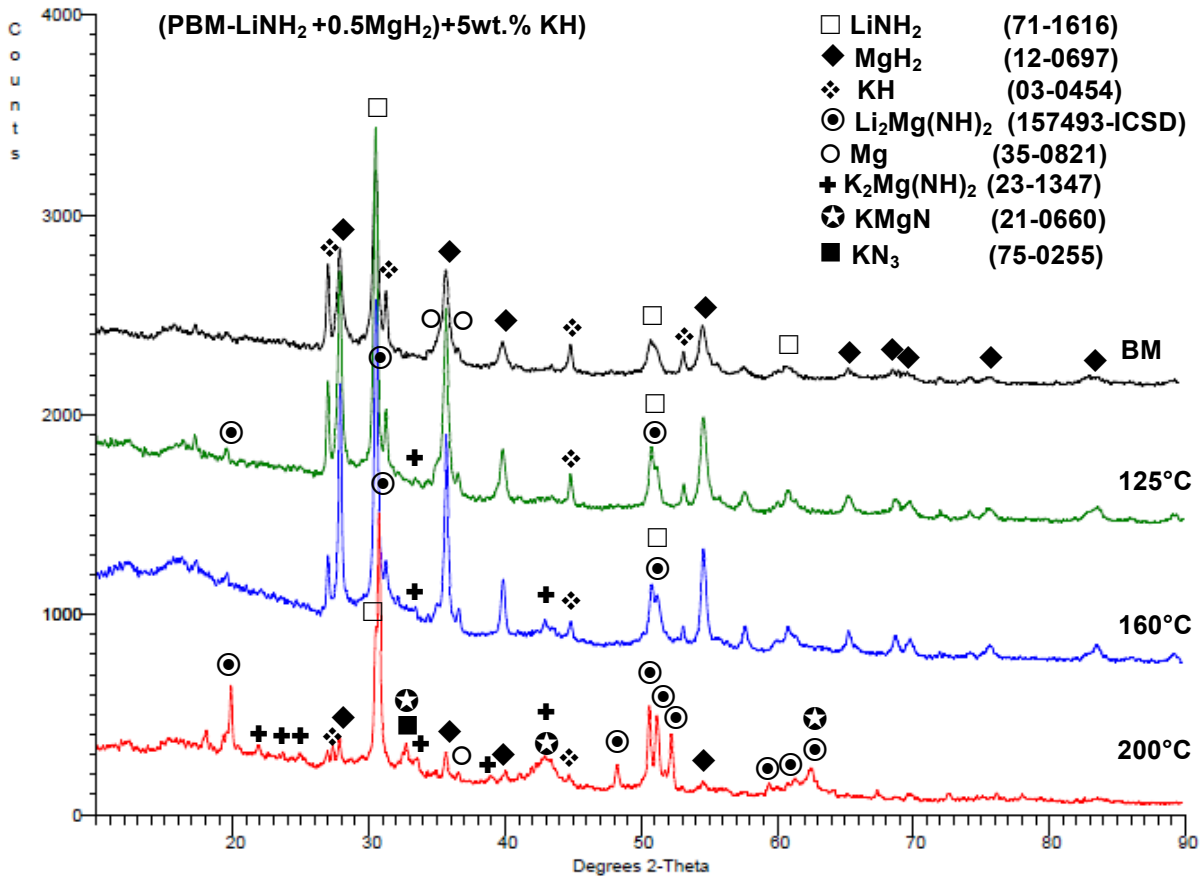

Fig.5.14. The XRD patterns after dehydrogenation at varying temperatures for (PBM($LiNH_2$+0.5MgH_2)+5 wt.% KH) system. ICDD file numbers are shown for peak identification. Ball milled with LES6-4B R132 15min (Q_{TR}=6.13 kJ/g).

The existence of $Li_2Mg(NH)_2$ after both, a low temperature (125-160°C) and high temperature (160-200) dehydrogenation, confirms that principal dehydrogenation reaction can be reaction (5-17), which was discussed thoroughly in the preceding section.

It is clear that $LiNH_2$ must have reacted with MgH_2 and KH producing $K_2Mg(NH)_2$, KMgN and KN_3 according to the following proposed reactions :

125-160°C:

$LiNH_2+0.5MgH_2 \rightarrow 0.5Mg(NH_2)_2 + 1.0LiH \rightarrow 0.5Li_2Mg(NH)_2 + 1.0H_2$ (5.6 wt.%H_2)

$0.5Mg(NH_2)_2 + KH \rightarrow 0.5K_2Mg(NH)_2+H_2$ (2.95 wt.%H_2) (5.4)

200°C:

$KH+MgH_2+6.0LiNH_2 \rightarrow KN_3+Li_2Mg(NH)_2+KMgN+4.0LiH+5.0H_2$ (1.42 wt.%H_2) (5.5)

Postulating any hypothesis about the desorption mechanisms and the effect of KH is premature yet and needs more systematic experiments. The only preliminary hypothesis is that KH does not act like a regular catalyst but instead takes part in reactions. Klebanoff et al. [137] reported similar results somehow but did not discuss the possible mechanisms.

In order to study the rehydrogenation, first the sample of (BM-($LiNH_2$+0.5MgH_2 +5wt.%KH)) was fully dehydrogenated at 200°C at 1 bar H_2 pressure. This was followed by a rehydrogenation step at 200°C at 50 bar H_2 pressure for 5 h and subsequent dehydrogenation at 200°C as shown in Fig. 5.15. It is clear that this system can be nearly fully rehydrogenated at 200°C and 50 bar H_2 pressure.

In addition to these two hydrides (KH and NaH) the effect of some other chemical compounds on dehydrogenation kinetics of ($LiNH_2$+0.5MgH_2) system was studied in this work. Appendix A-3 gives the results for these systems.

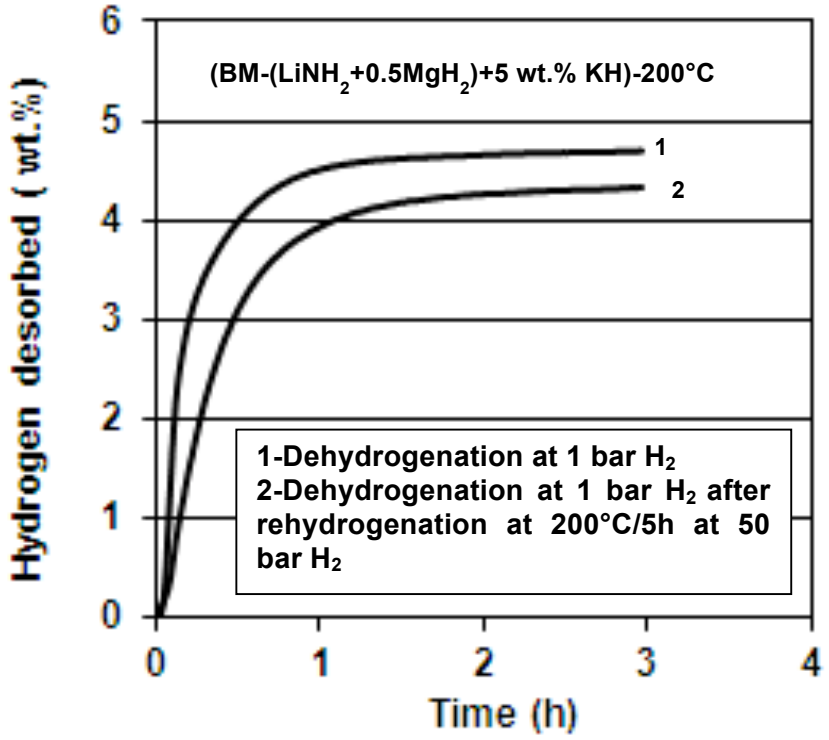

Fig.5.15. Volumetric dehydrogenation/rehydrogenation curves for (BM-($LiNH_2$+0.5MgH_2)+5wt.%KH) ball milled under the IMP-68-4B R40 25h (Q_{TR}=552.5 kJ/g) without H_2 desorption during milling.

5.3. Conclusions

1. A detailed study of the phase transformations occurring as a function of the ball milling energy injected into the hydride system ($LiNH_2$+nMgH_2) for the molar ratios n from 0.5 to 2.0 was carried out. The milling energy is estimated by a semi-empirical method for a specific milling geometry in the magneto-mill Uni Ball Mill 5.

2. X-ray diffraction (XRD) and Fourier Transform Infrared (FTIR) measurements show that for the molar ratios n<1.0 three new hydride phases such as LiH, amorphous $Mg(NH_2)_2$ (a-$Mg(NH_2)_2$) and $Li_2Mg(NH)_2$ are formed during ball milling depending on the injected quantity of milling energy.

3. The formation of the LiH and a-$Mg(NH_2)_2$ hydrides is not accompanied by a hydrogen release during milling while the formation of the $Li_2Mg(NH)_2$ hydride is accompanied by a profound release of hydrogen (mechanical dehydrogenation).

4. For the molar ratios n≥1.0 at a low level of injected milling energy the hydride phases formed are LiH and a-$Mg(NH_2)_2$. The latter reacts with MgH_2 with increasing injected milling energy to form the new phase MgNH which is accompanied by a profound mechanical dehydrogenation.

5. Based on the experimental data we established an approximate hydride phase-energy diagram (map) for various levels of injected milling energy and the molar ratios.

6. Pre ball milling can improve the dehydrogenation kinetics of ($LiNH_2$+0.5 MgH_2) but has negative effect in that of the system containing KH.

7. Addition of 5 %wt. KH can improve the desorption rate of the $LiNH_2$+0.5 MgH_2 system extremely, whether at low temperature range (125-160°C) or at high temperature (200°C).

8. Addition of NaH does not show a positive effect on the dehydrogenation behaviour of $LiNH_2$+0.5 MgH_2 composite.

9. Phase studies by XRD after volumetric isothermal dehydrogenation tests show that $Li_2Mg(NH)_2$, $K_2Mg(NH)_2$, are formed at the temperature range of 125-200°C, and KMgN and KN_3 are formed in 200°C.

6. Na-B-Mg-H and Li-B-Mg-H Systems

6.1. $NaBH_4$+2$Mg(OH)_2$ without and with the addition of nanometric nickel (n-Ni)

Fig. 6.1 shows a DSC curve obtained at a heating rate of 10°C/ min. Clearly only a single exothermic peak with a peak maximum temperature at 331 and 338 °C for the $NaBH_4$-based composite without and with 5 wt.% n-Ni, respectively, observed on the curve. Apparently, the n-Ni additive does not change thermal behavior of the hydride composites in any measurable way.

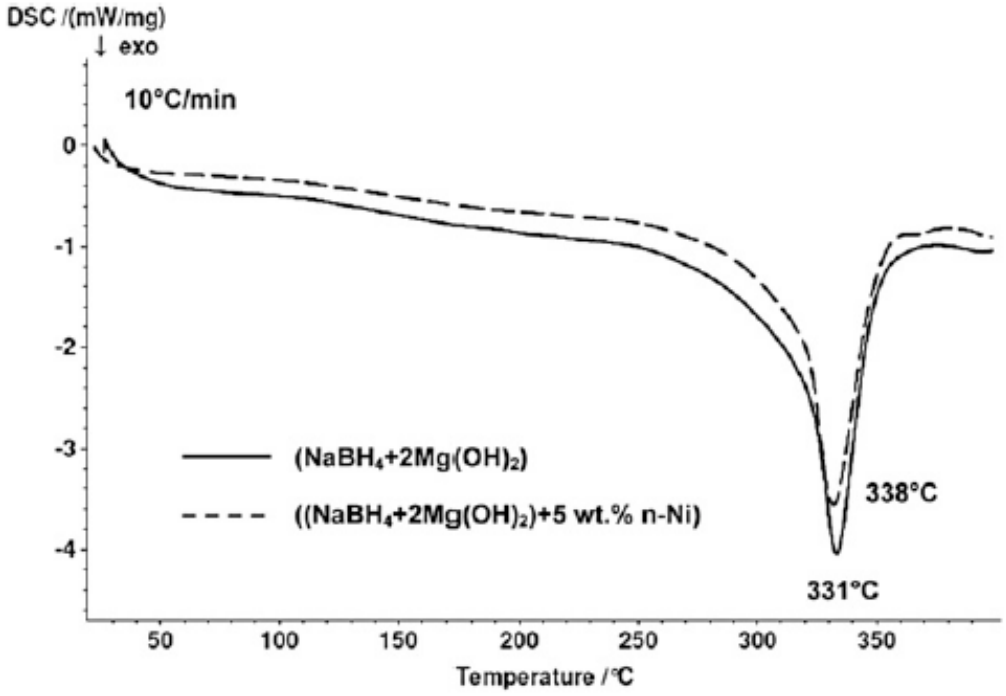

Fig. 6.1 DSC curve for ball milled ($NaBH_4$+2$Mg(OH)_2$) and ($NaBH_4$+2$Mg(OH)_2$)+5 wt.% n-Ni) under IMP68-4B R132 15min milling mode (Q_{TR}=18.2 kJ/g). Heating rate 10°C/min and 100 ml/min argon flow (Adapted from [77]).

Hydrogen volumetric desorption curves registered from ball milled ($NaBH_4$+$Mg(OH)_2$) at several temperatures are shown in Fig. 6.2 No evolution of hydrogen was observed at 200°C. Hydrogen evolution starts at 240°C. For the composite without the n-Ni

additive the quantity of released H_2 approaches ~5 wt.% H_2 after ~6h at 300°C (Fig. 6.2a). The addition of 5 wt.% n-Ni does not seem to accelerate the rate of desorption to any significant extent (Fig. 6.2b). At the first look the hydrogen desorption behavior observed in Fig. 6.2 seems to be similar to the one reported by Drozd et al. [118]. However, it is difficult to make any quantitative comparison with the H_2 desorption curves shown in [118] because the latter used a very uncommon relative scale for reporting the quantity of desorbed H_2 without specifying the amount of hydrogen corresponding to 100% on the scale. Using H_2 desorption curves in Fig. 6.2, we estimated the apparent activation energy from the corresponding Arrhenius-type plots shown in Fig. 6.3. It is clearly seen that the apparent activation energy for the composite without and with the n-Ni additive is ~152 and 157 kJ/mol, respectively. From the possible error in finding slope from somehow arbitrary selected linear portion of the dehydrogenation curves in Fig. 6.2 a,b, which was substituted in Eq. (7.2), the standard error for the apparent activation energy is estimated at about ±2.2 and ±0.9 kJ/mol for the $NaBH_4$-based composite without and with n-Ni, respectively. The apparent activation energy values are quite high. Within the experimental error there is no difference between both apparent activation energies, which clearly indicates that the n-Ni additive is not acting as a potential catalyst in this system. It is to be pointed out that the values of the apparent activation energy obtained in the present work compare very favorably with the apparent activation energy of 155.9 kJ/mol, reported by Drozd et al. [118] for ($NaBH_4$+2$Mg(OH)_2$) without any additives.

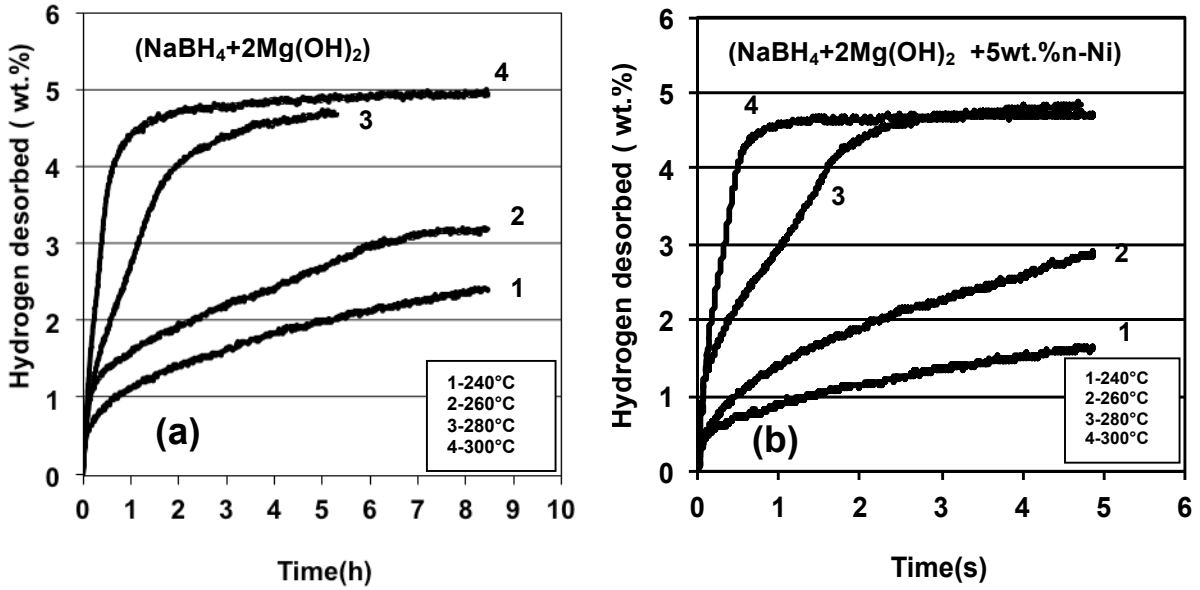

Fig. 11.2 Volumetric hydrogen desorption curves at various temperatures under 1 bar H_2 pressure for ball milled (a) $NaBH_4$+2Mg$(OH)_2$ and (b) ($NaBH_4$+2Mg$(OH)_2$ +5 wt.% n-Ni) Ball milled under IMP68-4B R132 15min milling mode (Q_{TR}=18.2 kJ/g). (Adapted from [77]).

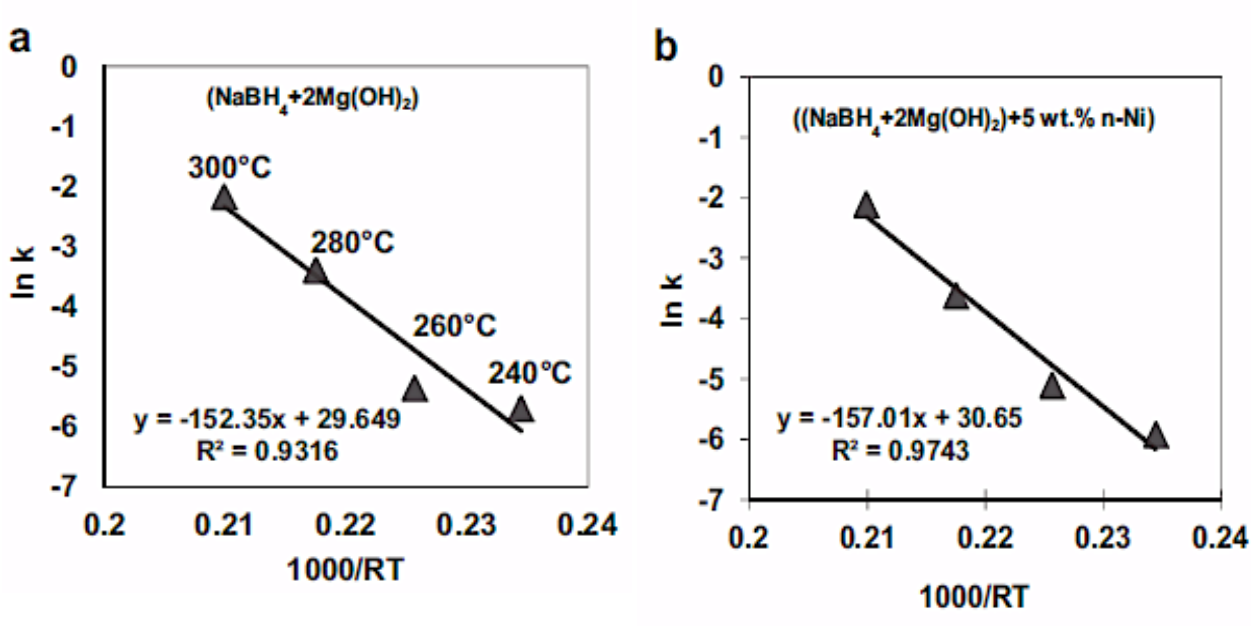

Fig 11.3 The Arrhenius plots for the estimation of the apparent activation energy for hydrogen desorption for ball milled (a) $NaBH_4$+2Mg$(OH)_2$ and (b) $NaBH_4$+2Mg$(OH)_2$)+5 wt.% n-Ni (Adapted from [77]). Ball milled under IMP68-4B R132 15min milling mode (Q_{TR}=18.2 kJ/g).

In order to understand the nature of the reactions occurring during dehydrogenation, the composite powder samples after completion of each isothermal dehydrogenation, corresponding to the total dehydrogenation time in Fig. 6.2a,b, were taken for an XRD test and the obtained patterns for ($NaBH_4$+2$Mg(OH)_2$) are shown in Fig. 6.4. The XRD patterns for the corresponding composite with the n-Ni additive were nearly identical so they are not shown here. It can be seen that the ball milled mixture (BM) shows the Bragg peaks of two principal constituents i.e. $NaBH_4$ and $Mg(OH)_2$ accompanied by relatively weak peaks of MgO which is an impurity found in as-received $Mg(OH)_2$. The BM XRD pattern confirms that the ($NaBH_4$+$Mg(OH)_2$) composite is stable under the conditions of high energy ball milling and no reaction between the constituents occurred during ball milling. We already reported that $NaBH_4$ exhibits high structural stability under severe conditions of mechanical milling [138] so it is expected that its reaction with $Mg(OH)_2$ would be rather difficult during ball milling. With increasing dehydrogenation temperature from 200 to 260°C the XRD patterns in Fig. 6.4 show decreasing intensity of the Bragg peaks of the principal phases $NaBH_4$ and $Mg(OH)_2$ and increasing intensity of MgO. At 260°C new Bragg peaks corresponding to a new phase $NaBO_2$ clearly appear which persist until 300°C. Since the composite starts releasing hydrogen at 240°C (Fig. 6.3a) the following dehydrogenation reaction is proposed which was also mentioned by Drozd et al. [118]

$$NaBH_4+2Mg(OH)_2 \rightarrow NaBO_2 +2MgO+ 4H_2 \quad (6\text{-}1)$$

It has a theoretical hydrogen capacity of 5.2 wt.%. Taking into account the H_2 capacity corrected for the purity of constituents (95%), Fig. 6.2a,b shows that at

300°C the ball milled ($NaBH_4$+$Mg(OH)_2$) composite without or with n-Ni desorbs nearly the entire purity corrected capacity of H_2.

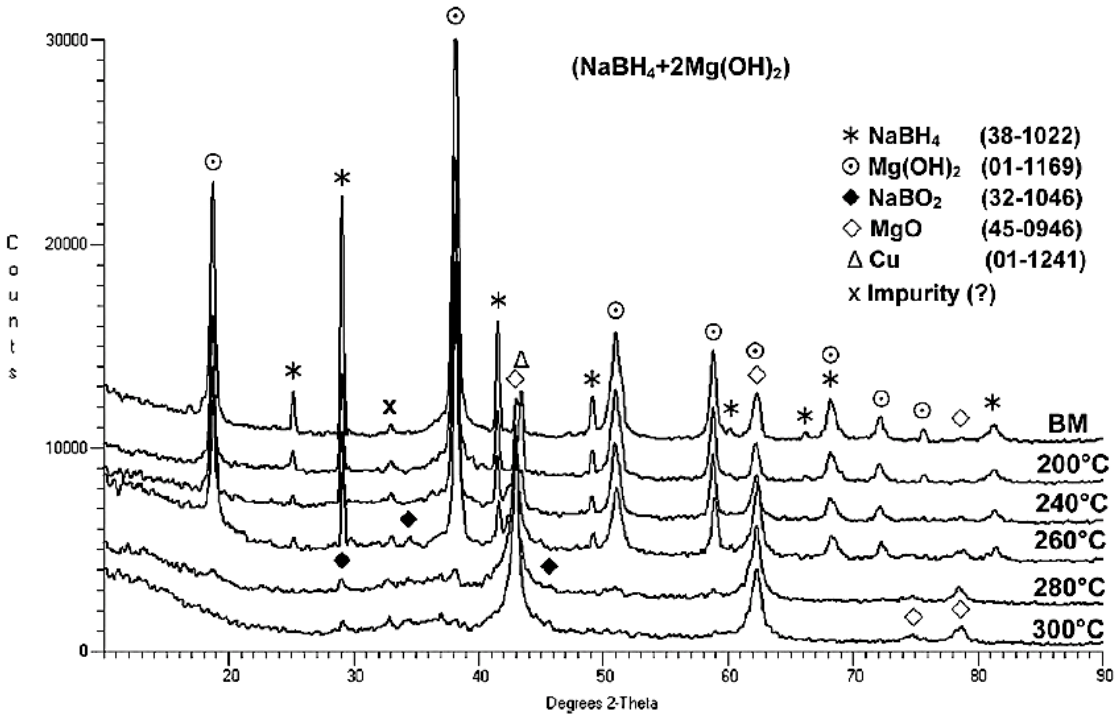

Fig. 6.4 XRD patterns for ball milled ($NaBH_4$+2$Mg(OH)_2$) after dehydrogenation at 200, 240, 260, 280 and 300°C as compared to the XRD pattern just after ball milling (BM). The JCPDS file numbers for phase identification are shown in the legend (Adapted from [77]). Ball milled under IMP68-4B R132 15min milling mode(Q_{TR}=18.2 kJ/g).

6.2. ($LiBH_4$+2$Mg(OH)_2$) without and with the addition of nanometric nickel (n-Ni)

The system based on $LiBH_4$ and $Mg(OH)_2$ has never been investigated before. Fig. 6.5a and b shows the results of DSC tests for the ball milled ($LiBH_4$+2$Mg(OH)_2$) composite without and with the n-Ni additive, respectively. Both DSC traces are nearly identical and show a small exothermic peak 1 with the temperature maximum around 87°C, much larger exothermic peak 2 with the temperature maximum around 200°C and finally, an endothermic peak 3 at around 365-368°C. According to [6, 37-

41,124] $LiBH_4$ undergoes a polymorphic phase transformation from an orthorhombic to hexagonal crystal structure around 100-120°C (depending on the heating rate in DSC) which has an endothermic character. Therefore, the first small peak 1 in Fig. 6.5a is not due to a polymorphic transformation because it is exothermic. However, Mosegaard et al. [139] reported the presence of an exothermic peak in DSC with the broad maximum around 90°C due to a surface reaction of water vapor and $LiBH_4$. Most likely, peak 1 is of the same nature. The powder was transferred to a DSC instrument in a glass vial filled with Ar and then quickly loaded into an Al_2O_3 crucible with a lid. This operation took less than a minute and for that period of time the powder could be in contact with moisture in air. Alternatively, a minutiae amount of retained moisture could have been present in the chamber of a DSC Netzsch 404 apparatus because before the test the apparatus was evacuated only by a rotary pump creating a rather low vacuum. The following thermal test was carried out under a constant flow of high purity argon, which might have not purified fully the atmosphere.

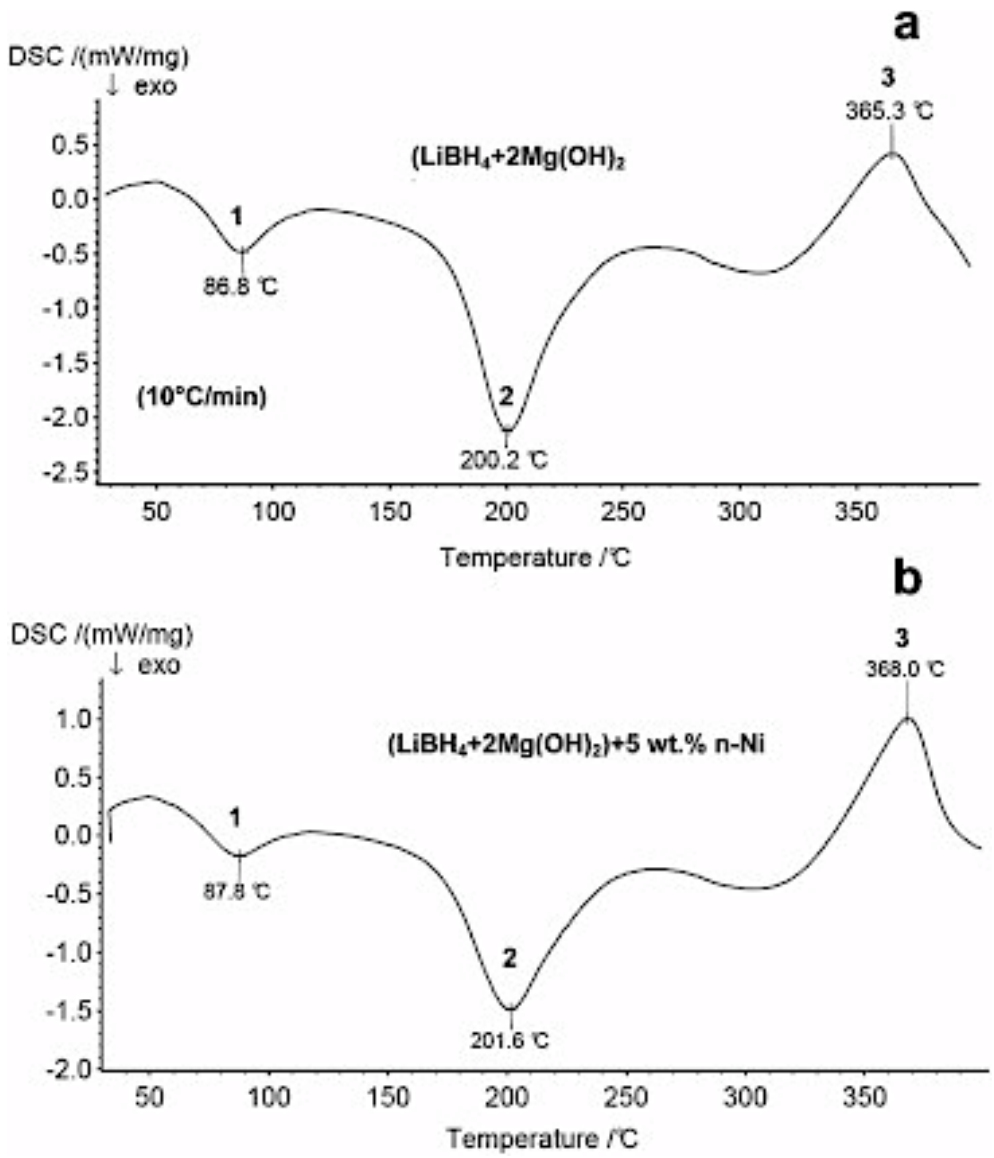

Fig. 6.5 DSC curve for the ball milled ($LiBH_4$+2$Mg(OH)_2$) composite (a) without and (b) with 5 wt.% n-Ni at 10°C/min heating rate and 100 ml/min argon flow (Adapted from [77]). Ball milled under IMP68-4B R132 15min milling mode (Q_{TR}=18.2 kJ/g).

The exothermic thermal event at ~200°C (peak 2) and endothermic one at ~365-368°C (peak 3) clearly indicate that in contrast to the DSC curve for the ($NaBH_4$+2$Mg(OH)_2$) composite in Fig.6.1 the $LiBH_4$-based composite dehydrogenates in two stages with opposite thermodynamics.

The dehydrogenation kinetics were investigated using a volumetric Sieverts-type apparatus and the pertinent dehydrogenation curves at various temperatures for the mechanically milled ($LiBH_4$+2$Mg(OH)_2$) composite without and with the n-Ni additive are shown in Fig. 6.6a and b, respectively. A striking feature seen on the dehydrogenation curves is that the $LiBH_4$-based composite desorbs quite a large amount of ~3.5 wt.% H_2 at 200°C within ~2500 s (0.7h). In contrast, for the $NaBH_4$-based composite the quantity of ~3.5 wt.% H_2 can be barely achieved at ~260°C within a time duration longer than 8.5 h. Apparently, the $LiBH_4$-based composite desorbs H_2 much more rapidly than its NaBH4-based counterpart. However, the maximum quantity of H_2 desorbed at 400°C from ($LiBH_4$+2$Mg(OH)_2$) without n-Ni is equal to ~5 wt.% (Fig. 6.6a) which is nearly the same as the one observed for its $NaBH_4$-based counterpart (Fig. 6.2a)

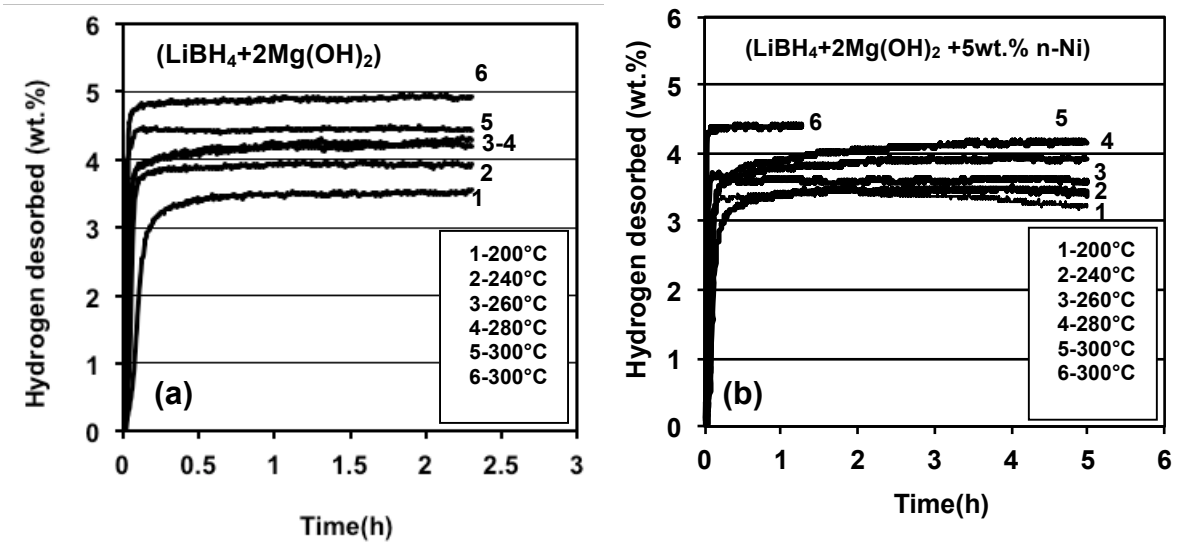

Fig. 6.6 Volumetric hydrogen desorption curves at various temperatures under 1 bar H_2 pressure for ball milled (a) ($LiBH_4$+2$Mg(OH)_2$) and (b) ($LiBH_4$+2$Mg(OH)_2$ +5 wt.% n-Ni) (Adapted from [77]). Ball milled under IMP68-4B R132 15min (Q_{TR}=18.2kJ/g).

Comparison of the amount of H_2 released from ($LiBH_4$+2$Mg(OH)_2$) without and with the n-Ni additive in Fig. 6.6a and b, respectively, shows that at each dehydrogenation temperature the ($LiBH_4$+2$Mg(OH)_2$+5 wt.% n-Ni) composite desorbs ~10% smaller quantity of H_2. This is shown in Fig. 6.7 as a function of dehydrogenation temperature. Using dehydrogenation curves in Fig. 6.6 we estimated the apparent activation energy for the rapid dehydrogenation stage (initial nearly a straight-line portion of the dehydrogenation curve) from the corresponding Arrhenius-type plots shown in Fig. 6.8. We used the dehydrogenation temperature range of 200-280°C to avoid a contribution to the dehydrogenation kinetics from the high temperature endothermic reaction in Fig. 6.5a,b.

It is clearly seen that the apparent activation energies for the $LiBH_4$-based composite without and with the n-Ni additive are quite low being equal to ~47 and 38 kJ/mol, respectively. From the possible error in finding slope from somehow arbitrary selected linear portion of the dehydrogenation curves in Fig. 6.6a,b, which was substituted in Eq. (7.2), the standard error for the apparent activation energy is estimated at about ±7.8 and ±6.2 kJ/mol for the $LiBH_4$-based composite without and with the n-Ni additive, respectively. The apparent activation energy values for the $LiBH_4$-based composite values constitute only about 25-30% of the apparent energy values estimated for the $NaBH_4$-based mixture (Fig. 6.3). Such low apparent activation energy values clearly explain a rapid dehydrogenation rate observed in Fig. 6.6. However, the apparent activation energy for the $LiBH_4$-based composite with n-Ni additive is only slightly lower than that without the additive. Apparently, the n-Ni additive at the content of 5 wt.% does not have a more substantial accelerating effect

on the rate of dehydrogenation. It has been reported that the addition of pure metal catalysts like, for example, Ni [39] and metal chlorides ($FeCl_2$, $CoCl_2$ and $NiCl_2$ [41]), which in principle decomposes to the nanometric elemental metals and salts accelerate the dehydrogenation rate of $LiBH_4$. There are a few hypothetical factors that may be responsible for the fact that a strong catalytic effect of n-Ni on the rate of the first stage of dehydrogenation is not observed in the present work. First, the level of the apparent activation energy for the $LiBH_4$-based composite without the additive is already so low that no catalytic additive could lower it anymore. Second, the content of 5 wt.% n-Ni is still insufficient for being more effective. Third, it is feasible that the presence of $Mg(OH)_2$ hydroxide in the intimately ball milled composite with $LiBH_4$ somehow reduces the catalytic potential of nanometals due to their rapid oxidation which, in turn, may substantially reduce their catalytic activity. All these factors need more investigation.

The phase changes occurring during isothermal dehydrogenation were investigated by XRD of the samples fully dehydrogenated at each prescribed temperature such that the XRD patterns in Figs. 6.9 and 6.10 correspond to the end of dehydrogenation time in Fig. 6.6a,b for ($LiBH_4$+2$Mg(OH)_2$) without and with the n-Ni additive, respectively. For comparison, the XRD patterns of the ($LiBH_4$+2$Mg(OH)_2$) powders just mixed by mortar-and-pestle (Mix) and those after ball milling (BM) are also shown on the corresponding XRD patterns.

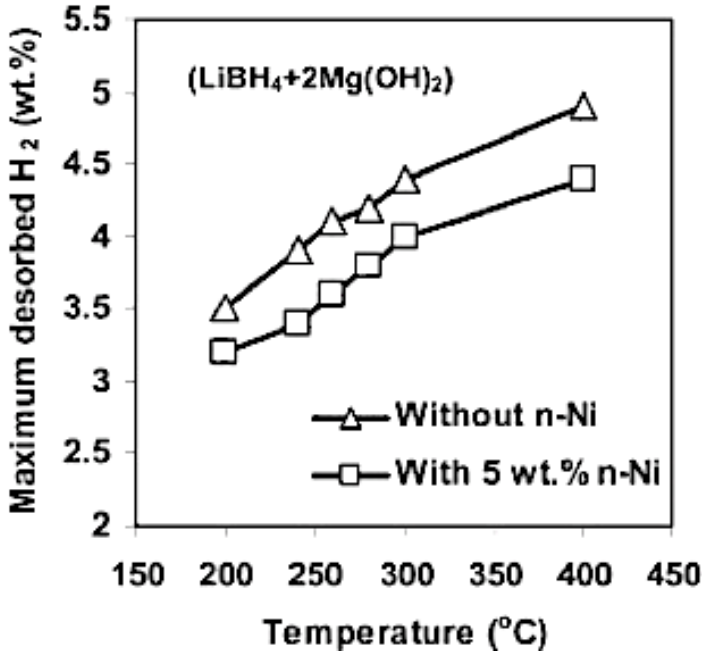

Fig.6.7 Comparison of the maximum hydrogen quantity released for the ($LiBH_4$+2Mg$(OH)_2$) composite without and with n-Ni at various temperatures (Adapted from [77]). Ball milled under IMP68-4B R132 15min milling mode (Q_{TR}=18.2 kJ/g).

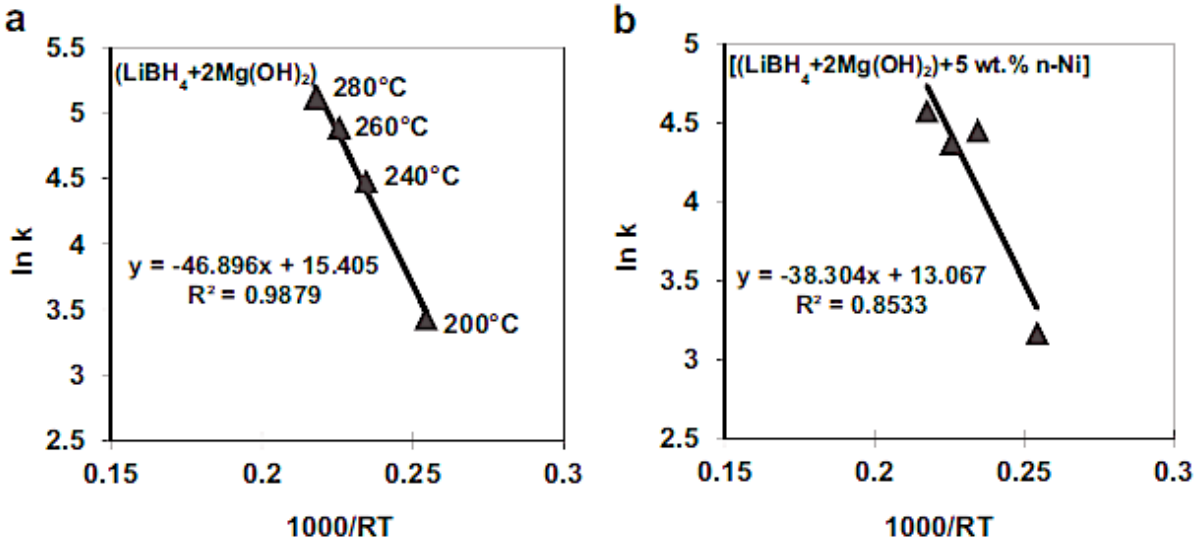

Fig. 6.8 The Arrhenius plots for the estimation of the apparent activation energy for hydrogen desorption for ball milled (a) $LiBH_4$+2Mg$(OH)_2$ and (b) (($LiBH_4$+2Mg$(OH)_2$)+5 wt.% n-Ni).Ball milled under IMP68-4B R132 15min milling mode (Q_{TR}=18.2 kJ/g). (Adapted from [77]).

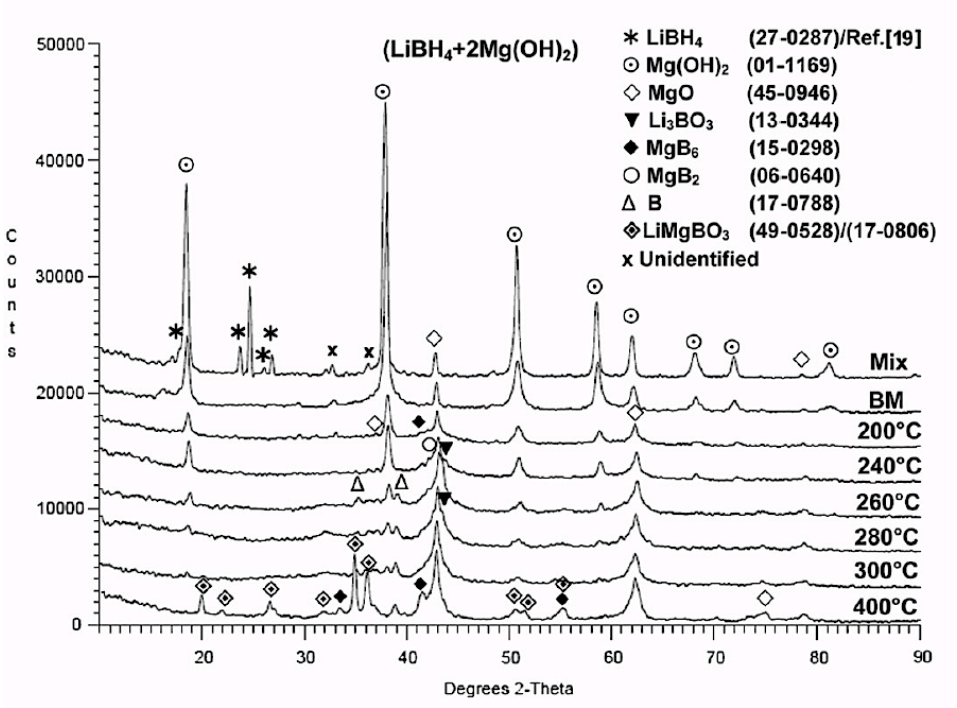

Fig. 6.9 XRD pattern for ($LiBH_4$+2$Mg(OH)_2$) after dehydrogenation at various temperatures (Mix-mixed without milling; BM-ball milled under IMP68-4B R132 15min milling mode (Q_{TR}=18.2 kJ/g). The JCPDS file numbers for phase identification are shown in the legend (Adapted from [77]).

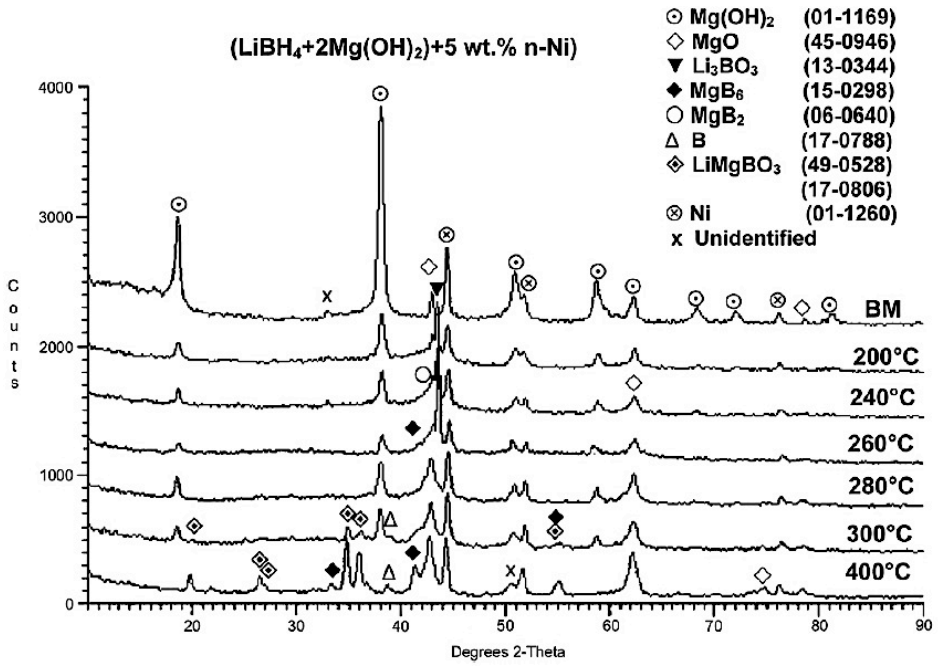

Fig. 6.10 XRD patterns (($LiBH_4$+2$Mg(OH)_2$)+5 wt.% n-Ni) after dehydrogenation at various temperatures as compared to ball milled composites (BM) under IMP68-4B R132 15min milling mode(Q_{TR}=18.2 kJ/g). The JCPDS file numbers for phase identification are shown in the legend (Adapted from [77]).

The XRD pattern for the mortar-and-pestle mixed sample of ($LiBH_4$+2$Mg(OH)_2$) in Fig. 6.9 contains predominantly the Bragg peaks of orthorhombic $LiBH_4$, which were identified using JCPDS #27-0287 and the synchrotron pattern reported in [140], Mg(OH)2 and the MgO inherent impurity. Two unidentified weak peaks are, most likely, due to some impurities retained from the manufacturing process of LiBH4. Ball milling (BM) of the composites brings about a very striking transformation of the respective XRD patterns for both (LiBH+2$Mg(OH)_2$) and (($LiBH_4$+2$Mg(OH)_2$)+5 wt.% n-Ni) in Figs. 6.9 and 10. The diffraction peaks of $LiBH_4$ completely disappear after ball milling while the peaks of $Mg(OH)_2$, the MgO impurity and Ni the latter for the (($LiBH_4$+2$Mg(OH)_2$)+5 wt.% n-Ni) composite, are still well visible. This is a completely different behavior after ball milling than that observed for the $NaBH_4$-based composite (Fig. 6.4). The lack of any new Bragg peaks due to the formation of some new phases, clearly indicates that no reaction between $LiBH_4$ and $Mg(OH)_2$ occurred during ball milling that might have been responsible for a complete depletion of the $LiBH_4$ constituent and the disappearance of its Bragg peaks. It must be assumed that the $LiBH_4$ phase becomes either amorphous or heavily nanostructured after ball milling which either does not give Bragg peaks or the peaks are very weak and completely suppressed by much stronger peaks of the $Mg(OH)_2$ constituent in the composite (Figs. 6.9 and 6.10). On the other hand, ball milled pristine $LiBH_4$ which we tested by XRD shows the Bragg peaks although broadened and weaker but still quite clearly visible (not shown here). However, the amorphization of $LiBH_4$ in the composite with $Mg(OH)_2$ cannot be ruled out of hand because it is unknown how the presence of $Mg(OH)_2$ would affect the ball milling of $LiBH_4$. Therefore, the cause of

the disappearance of the $LiBH_4$ Bragg peaks is not quite clear at the moment. However, it must be strongly pointed out that $LiBH_4$ is definitely present in the composite after ball milling which is supported by a further evolution of XRD patterns with increasing temperature of dehydrogenation indicating that $LiBH_4$ must have reacted with $Mg(OH)_2$ which is also associated with the release of H_2 (Fig. 6.6a,b). A gradual reduction in the intensity of the principal $Mg(OH)_2$ diffraction peaks and an increase in the intensity of the principal MgO peaks are clearly visible in Fig. 6.9for ($LiBH_4$+2$Mg(OH)_2$). In the pattern take after dehydrogenation at a high temperature of 300°C the $Mg(OH)_2$ diffraction peaks are nearly invisible while the MgO peaks are very strong and broad. The XRD pattern of the $LiBH_4$+2$Mg(OH)_2$) sample without and with n-Ni dehydrogenated at 240-300°C (Figs. 6.9 and 6.10) contains the peaks of $Mg(OH)_2$, MgO, and weak peaks of new phases identified as Li_3BO_3, MgB_2 and MgB_6. It is clear that the $LiBH_4$ must have reacted with $Mg(OH)_2$ producing MgO, Li_3BO_3, MgB_2, MgB_6 and H_2 according to the following reaction:

$$12LiBH_4+10Mg(OH)_2 \rightarrow 4Li_3BO_3+8MgO+MgB_2+MgB_6+34H_2 \qquad (6\text{-}2)$$

The theoretical H2 capacity of reaction (6-2) is 8.1 wt.%. Comparing reaction (6-2) with the DSC curve in Fig. 6.5a it is most likely that it corresponds to peak 2 and as such has an exothermic character. The appearance of two new phases B (very small peaks) and $LiMgBO_3$ after dehydrogenation at 300°C and a gradual decrease in the intensity of diffraction peaks of the Li_3BO_3 and MgB_2 phases indicates that another reaction has already started during which Li_3BO_3, $Mg(OH)_2$ and MgB_2 are being

consumed while MgO, MgB_6, B and a new phase $LiMgBO_3$ are being produced. The proposed reaction can be written as follows:

$$Li_3BO_3 + 6MgB_2+8Mg(OH)_2 \rightarrow 3LiMgBO_3 +10MgO+MgB_6+4B+ 8H_2 \quad (6\text{-}3)$$

The theoretical H_2 capacity of reaction (6-3) is only 2.26 wt.%. Comparing reaction (6-3) with the DSC curve in Fig. 6.5a it is most likely that it corresponds to peak 3 and as such has an endothermic character. However, since the DSC curves are obtained at a constant continuous heating rate whereas the dehydrogenation curves are isothermal, it is rather difficult to establish the exact ranges of dehydrogenation temperatures where both reactions can occur. Most likely the temperature ranges of reaction (6-2) and (6-3) superimpose to some extent. On the basis of the phase evolution in Fig. 6.9 it may be estimated that for the ($LiBH_4$+2$Mg(OH)_2$) composite reactions (6-2) and (6-3) occur approximately at the temperature range of 180-260°C and 260-400°C, respectively.

Another important point is that a certain quantity of $Mg(OH)_2$ still exists even after dehydrogenation at 300°C, whose diffraction peaks can be recognized in Figs. 6.9 and 10. For this reason, reaction (6-2) definitely does not proceed to completion. Reaction (6-2) and possibly (6-3) seem to proceed relatively rapidly in the beginning as shown by dehydrogenation curves in Fig. 6.6 but then they saturate and do not go to completion even at such a high temperature as 400°C because the total H_2 capacity dehydrogenated at this temperature from the ($LiBH_4$+2$Mg(OH)_2$) composite is only ~5 wt.% (Fig. 6.6a) as compared to a total theoretical capacity of combined

reaction (6-2) and (6-3) being equal to ~10.4 wt.% H_2 (or ~9.9 wt.% H_2 for taking into account a correction for 95% purity of constituents). More research is required to clarify this problem. The addition of the n-Ni additive does not seem to change the character of reaction (6-2) and (6-3) as can be seen in the XRD patterns in Fig. 6.10. However, since high intensity peaks of the Li_3BO_3 phase clearly appear at 200°C for a composite containing n-Ni vis-a`-vis 240°C for a composite without n-Ni (Fig. 6.9), it seems that reaction (6-2) is slightly accelerated by n- Ni. On the other hand, a lack of clearly visible peaks of B in Fig. 6.10 after dehydrogenation at temperatures 260-280°C may indicate some deceleration of reaction (6.3) by n-Ni. These two opposite factors might be responsible for a lower total quantity of desorbed H_2 from the composite with n-Ni in Fig. 6.6b as opposed to the quantity of H_2 desorbed from the composite without n-Ni in Fig. 6.6a. Finally, it must be pointed out that the investigated composites of ($NaBH_4$+2$Mg(OH)_2$) and ($LiBH_4$+2$Mg(OH)_2$) cannot be considered as potential candidates for hydrogen storage materials for on-road automotive applications for supplying hydrogen to automotive Proton Exchange Membrane (PEM) fuel cells. Both composites seem to have too low desorbed total H_2 capacity, too high dehydrogenation temperature, relatively long dehydrogenation time and most likely they are non reversible due to the occurrence of exothermic reactions during dehydrogenation which do not meet the US Department of Energy (DOE) targets for 2015 [29].

However, their theoretical H_2 capacity is still quite attractive, especially for the one based on $LiBH_4$, and after finding more appropriate catalysts at least the $LiBH_4$-based composite could be considered for applications in stationary power systems (PEM or

solid oxide fuel cells), off-road vehicles (e.g. fork lifts) and disposable H_2 cartridge generators for various portable devices for civilian and military applications.

6.3 Conclusions

The composites of ($NaBH_4$+$_2Mg(OH)_2$) and ($LiBH_4$+$2Mg(OH)_2$) without and with nanometric Ni (n-Ni) were synthesized by high energy ball milling. The DSC test shows that the ball milled $NaBH_4$-based composite dehydrogenates during one exothermic reaction with the peak maximum around 330°C. Phase studies by XRD after volumetric isothermal dehydrogenation tests show that $NaBO_2$ and MgO are the products of the reaction which has a theoretical H_2 capacity of 5.2 wt.%. The estimated apparent activation energy is 152 ± 0.3 and 157 ± 0.3 kJ/mol for the composite without and with the n-Ni additive, respectively. The DSC tests show that the thermal behavior of the ball milled ($LiBH_4$+$2Mg(OH)_2$) is more complicated. It exhibits a principal exothermic reaction with the peak maximum at around 200°C followed by an endothermic reaction with the peak maximum at around 370°C. Phase studies by XRD after volumetric isothermal dehydrogenation tests show that MgO, Li_3BO_3, MgB_2, MgB_6 are the products of the first exothermic reaction which has a theoretical H_2 capacity of 8.1 wt.%.

However, for reasons which are not quite clear the first reaction never goes to full completion even at 300°C releasing ~4.5 wt.% H_2 at this temperature. However, the estimated apparent activation energies for the first rapid reaction are very low being equal to ~47 ± 7.8 and 38 ± 6.2 kJ/mol for composites without and with the n-Ni additive. The products of the second endothermic reaction are MgO, MgB_6, B and $LiMgBO_3$ and the reaction has a theoretical H_2 capacity of only 2.26 wt.%. In general,

the addition of nanometric Ni does not show a positive effect on the dehydrogenation behavior of both $NaBH_4$-and $LiBH_4$-based composites. Moreover, the addition of 5 wt.% of n-Ni to the ($LiBH_4$+2$Mg(OH)_2$) composite causes a 10% decrease in the amount of released hydrogen at each dehydrogenation temperature.

7. Li-Al-H system

7.1 The effect of mechanical ball milling and metallic additives (Fe and Ni)

7.1.1 Morphology and microstructure of iron and milled composite powders

Fig.7.1 shows the morphology of as-received micrometric Fe (m-Fe) and its gradual evolution after 1, 3 and 10 h of milling time. By increasing the milling time, the originally spherical particles (Fig.7.1a) become flattened and, especially after 10 h of milling, start to resemble pancakes (Fig.7.1b-d). This change is accompanied by the formation of a fraction of very fine particles with dimensions approaching 200-600 nm range (Fig.7.1d). Fig.7.2a shows the morphology of as received nanometric Fe (n-Fe).

The corresponding XRD pattern in Fig.7.2b shows that n-Fe also contains Fe_3O_4 in the amount of about 15% as specified by the supplier [141]. The pre-milled m-Fe powders and “as-received” n-Fe powder were added in the amount of 5 wt.% to the $LiAlH_4$ powder; they were further processed into a composite by high energy milling under the high energy impact mode (IMP68-4B-R132 Q_{TR} = 72.6 [kJ/gh]) for 15 min. Fig.7.2c shows the morphology of the ($LiAlH_4$+5 wt.% n-Fe) composite after ball milling. There was evidence of substantial refinement of the processed composite, although some clustering had already occurred. As shown in [142], the “as received” $LiAlH_4$ powder used in the present work has the average ECD (Equivalent Circle Diameter) particle size with a standard deviation (S.D.) equal to 9.9 ± 5.2 μm. The high energy ball milling reduced the ECD to 2.8 ± 2.3 μm. In general, it was noticed that even high energy ball milling is not significantly effective in reducing the average particle size of $LiAlH_4$ to less than 1 μm [74,76,142].

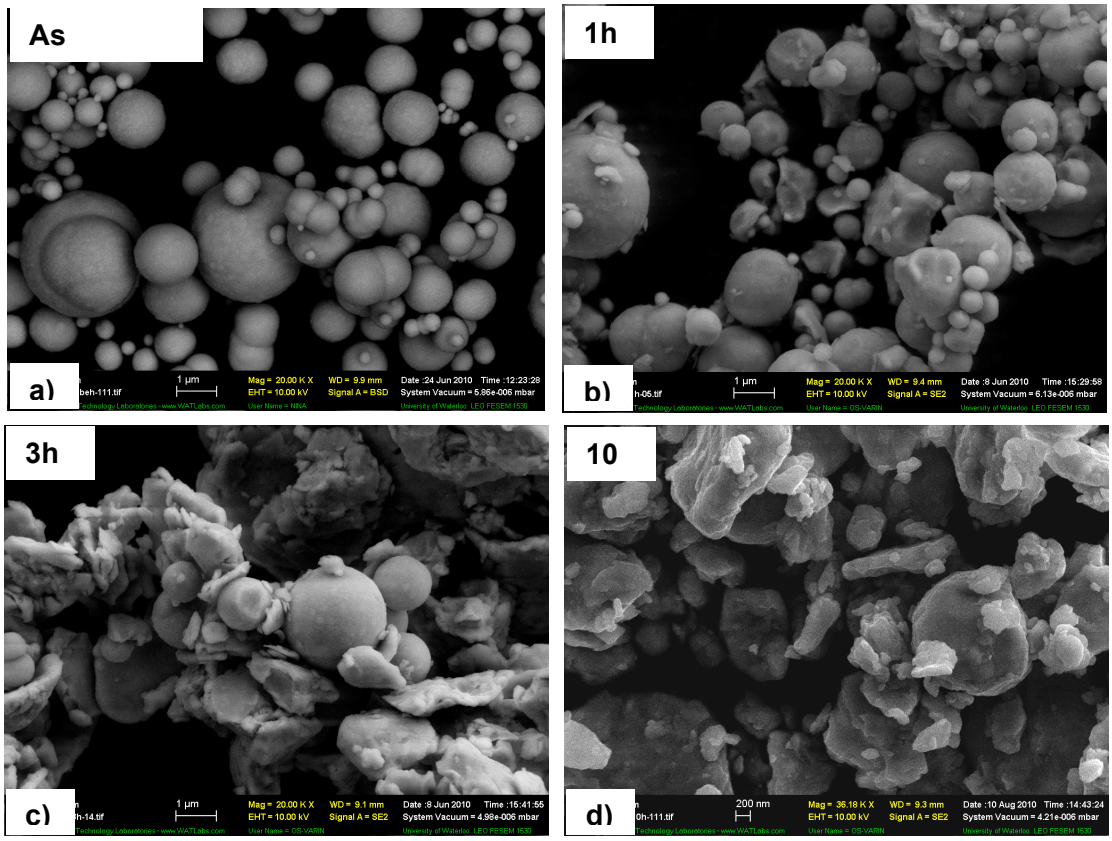

Fig.7.1 Scanning electron micrographs of (a) as received m-Fe (BSD) and the same m-Fe ball milled under IMP68-4B R40 for (b) 1 h (SE), (c) 3 h (SE) and (d) 10 h (SE). BSD-backscattered electrons and SE - secondary electrons mode (Adapted from [42]).

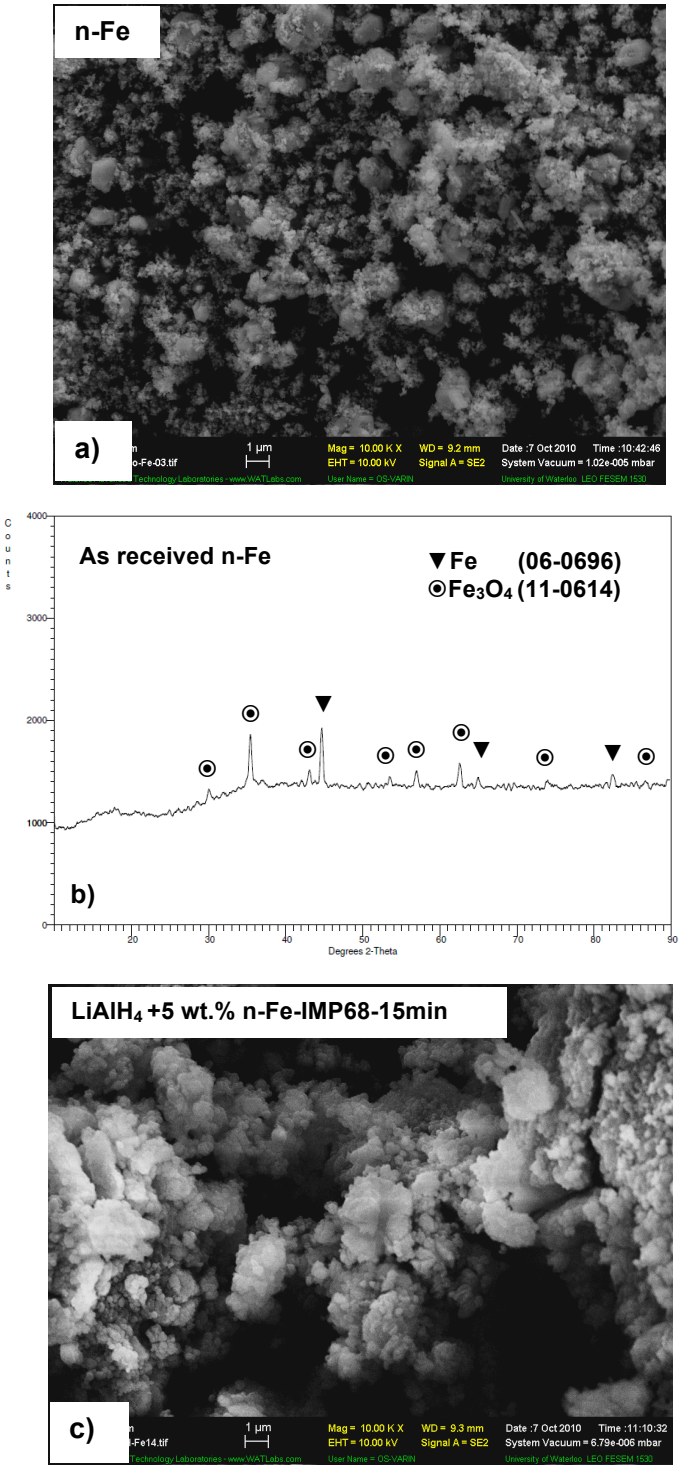

Fig.7.2 (a) Scanning electron micrograph of as received n-Fe (SE), (b) X-ray diffraction pattern of as received n-Fe (ICDD file numbers are shown for peak identification) and (c) scanning electron micrograph of a ball milled composite of (LiAlH4+5 wt.% n-Fe).SE secondary electrons mode (Adapted from [42]).

The H_2 pressure inside the milling vial was monitored throughout the entire milling duration. We noticed that when the $LiAlH_4$ composite with 5 wt.% n-Fe was milled under the high impact energy (IMP68) mode there was a continuous increase in the H_2 pressure inside the vial during milling. When the same composite was milled under the lower energy mode (LES6), the pressure increase was either non-measurable or within the accuracy of the pressure gage. The pressure increase was not observed at all during milling of $LiAlH_4$ with the 5 wt.% m-Fe additive. Obviously, the H_2 pressure increase indicates a gradual desorption of hydrogen from ($LiAlH_4$+5 wt.% n-Fe) milled under a high energy mode. From the H_2 pressure increase, we calculated wt.% H_2 desorbed during milling [6] as a function of milling time (which is plotted in Fig.7.3a [triangles]). In order to confirm that H_2 desorption is reproducible, we performed a second milling experiment and the obtained results are also plotted in Fig.7.3a (solid circles). As illustrated, both results are nearly identical; therefore, it is clear that under the high energy IMP68 milling mode ~3.5 wt.% H_2 is desorbed within 5 h of milling from the ($LiAlH_4$+5 wt.% n-Fe) composite. This behaviour is similar to the one observed when metal chlorides [61,68,70,72] are added to $LiAlH_4$ but has never been reported for the n-Fe additive.

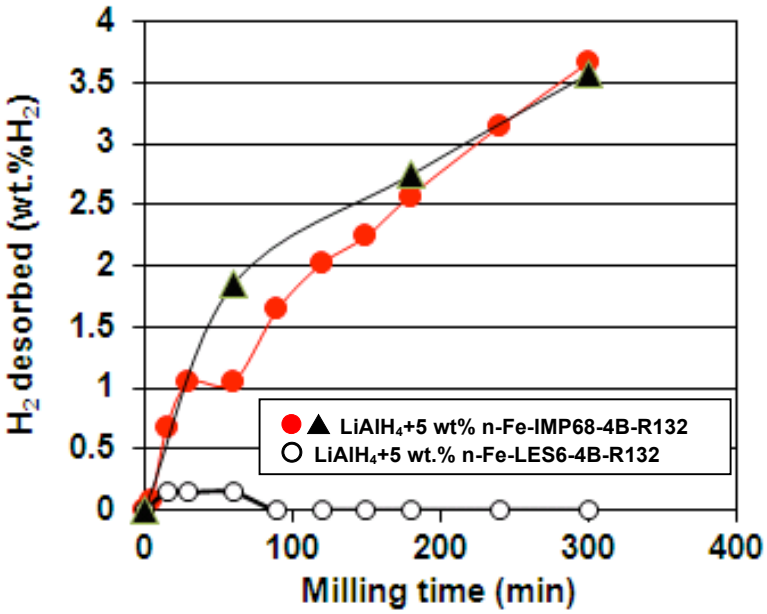

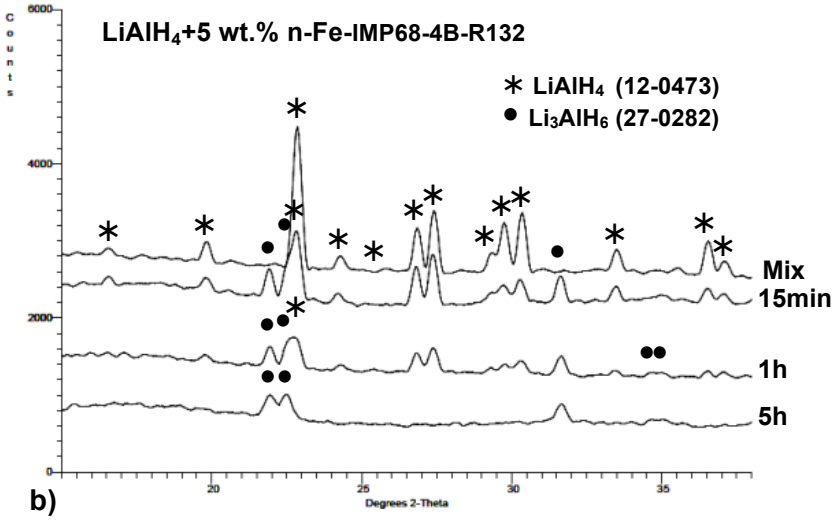

Fig.7.3 a) The quantity of H_2 desorbed during ball milling under the high impact energy (IMP68) mode and the low shearing energy (LES6) mode as a function of milling time. b) XRD patterns after milling under high energy (IMP68) for various times (Adapted from [42])

.

In order to identify the reaction that results in the H_2 desorption during ball milling, the XRD patterns were obtained from the powders milled for 15 min, 1 h and 5 h; these were then compared to the XRD for a mixed powder (in Fig.7.3b). After only 15 min of milling, the diffraction peaks of Li_3AlH_6 are clearly seen, as opposed to the $LiAlH_4$ peaks that are observed for the mixed powders. The intensity of the Li_3AlH_6 peaks increased after 1 and 5 h of milling, accompanied by a gradual disappearance of the $LiAlH_4$ peaks (which is accompanied by more H_2 desorbed as can be seen in Fig.7.3a). During the high energy milling, it is obvious that there is a gradual decomposition of $LiAlH_4$ in its solid state according to reactions (5-9) and (5-10). As mentioned before, reaction (5-9) has a maximum theoretical H_2 capacity of 5.3 wt.% and about 4.9 wt.% if both the purity and the presence of 5 wt.% n-Fe are taken into account. Therefore, Fig.7.3a shows that nearly 71-82% of the purity-corrected H_2 capacity of reaction (5-9) can be desorbed during milling up to 5 h. The upward trend of the desorption curve in Fig.7.3a strongly suggests that further milling under IMP68-4B R132 (Q_{TR132}=72.8kJ/gh) mode for a duration longer than 5 h would most likely result in a nearly total H_2 desorption from the catalyzed composite.

In order to shed some light on the mechanisms by means of which the n-Fe additive accelerates H_2 desorption during milling, we investigated the variations of the crystallographic lattice parameters and unit cell volume of $LiAlH_4$ as a function of the type of Fe additive (micrometric or nanometric). This could only be done for powders milled for the time duration after which the diffraction peaks for $LiAlH_4$ can be still discerned in the XRD patterns. For comparison, we also used 5 wt.% of the micrometric and nanometric Ni additives (m-Ni and n-Ni), which were milled with

$LiAlH_4$ under similar conditions as those for the Fe additive. The m-Ni and n-Ni additives were obtained from Vale Ltd. Canada and their specific surface areas (SSA) were measured by the BET (Brunauer, Emmett and Teller) method in the Vale Ltd. laboratories. Three different powders, each with different SSA (9.5, 17.9 and 85 m^2/g), were used in this research. Table 7.1 shows the obtained values of the lattice parameters/unit cell volume and Fig.7.4 shows the correlation of the LiAlH4 volumetric lattice expansion with milling mode, the particle size of additives, and the event of H_2 desorption during milling.

It is significant to note, for this research, we used three batches of "as received" $LiAlH_4$ that was ordered at various time periods. These powders are designated in Table 7.1 as (1), (2) and (3). The lattice constant measurements show that the unit cell volume (V_0) of these batches varies from one batch to the other. Therefore, the volumetric lattice expansion ($\Delta V/V_0$) for ball milled composite was calculated with respect to the unit cell volume of the $LiAlH_4$ batch that was used for compositing with the Fe or Ni additive. This is an important finding and should be taken as a precaution by other researchers: the same unit cell volume should not be used for calculations if different batches of $LiAlH_4$ were used in due course of experiments.

Table 7.1. The lattice parameters and unit cell volume for $LiAlH_4$ after milling under various milling modes/energy and for varying milling durations and with the addition of either pre-milled μ-Fe or n-Fe. For all samples milling was carried out with R132 and 4 balls in the vial (4B).

Additive/processing mode	Lattice parameters $LiAlH_4$				Unit cell volume, V_0 ($Å^3$)	Unit cell volume, V ($Å^3$)	($\triangle V/V_o$) (%)
	a (Å)	b (Å)	c (Å)	β (deg)			
As received $LiAlH_4$ (1)	9.6706	7.8437	7.9020	112.56	553.5285	-	-
As received $LiAlH_4$ (2)	9.6803	7.8783	7.9092	112.34	557.9170	-	-
As received $LiAlH_4$ (3)	9.6520	7.8567	7.8703	111.73	554.4134	-	-
n-Fe-LES6-15min	9.7292	7.8282	7.8738	112.39	553.5285	554.4766	0.171
n-Fe-LES6-1h	9.6697	7.8230	7.9303	112.26	553.5285	555.1884	0.300
n-Fe-LES6-5h	9.6479	7.8583	7.9194	111.53	557.9170	558.5241	0.1088
μ-Fe(1h)-IMP68-15min	9.6481	7.8770	7.9028	111.64	553.5285	558.2671	0.856
μ-Fe(3h)-IMP68-15min	9.6376	7.8873	7.9033	111.57	553.5285	558.6943	0.933
μ-Fe(10h)-IMP68-15min	9.6779	7.8587	7.9171	112.27	553.5285	557.2260	0.668
n-Fe-IMP68-2B-15min	9.6513	7.8612	7.8989	111.92	553.5285	555.9704	0.441
n-Fe-IMP68-5min	9.6760	7.8797	7.9197	111.87	554.4134	560.3648	1.0735
n-Fe-IMP68-15min	9.8600	7.7170	7.9106	111.15	553.5285	561.3690	1.416
n-Fe-IMP68-1h	9.6590	7.8961	7.9194	112.04	553.5285	559.8611	1.144
μ-Ni-IMP68-15min (Ni123)	9.6810	7.8435	7.8888	112.22	554.4134	554.5356	0.0221
n-Ni-IMP68-15min (SSA 9.5 g/m^2)	9.6629	7.8293	7.9279	111.37	557.9170	558.5388	0.1115
n-Ni-IMP68-15min (SSA 17.9 g/m^2)	9.7665	7.8478	7.9771	113.45	557.9170	560.9086	0.5362
n-Ni-IMP68-15min (SSA 17.9 g/m^2)	9.7470	7.8410	7.9791	114.24	554.4134	556.0476	0.2948

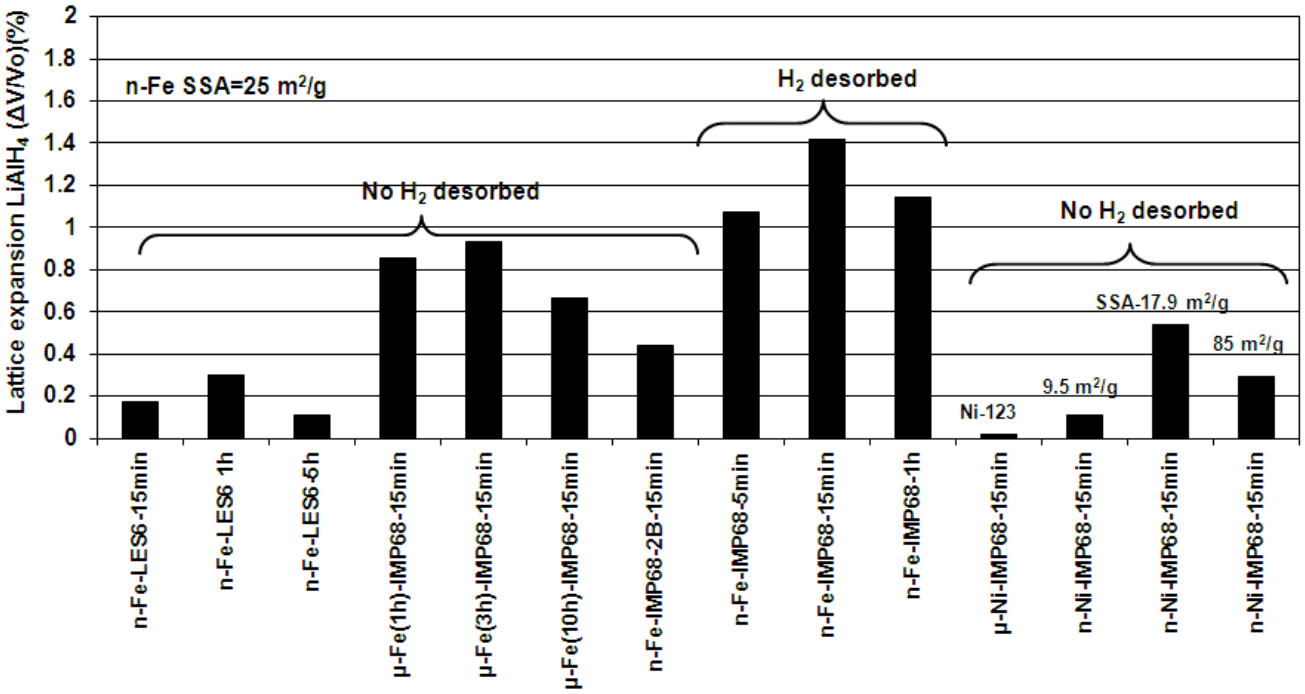

Fig.7.4 The correlation of the volumetric lattice expansion for $LiAlH_4$ with the type of Fe additive (m-Fe n-and Fe), milling mode and observed hydrogen desorption event during milling. For comparison, the results for m-Ni and n-Ni are also shown. Milling with four balls (4B) in the vial for the indicated time duration except one case with two balls (2B). SSA-specific surface area. (Adapted from [42]).

It is clear that each mode of milling/energy results in the crystal volume expansion of which its magnitude depends on the energy of milling, the type of additive, and its particle size. For example, a low energy shearing mode (LES) of the composite with n-Fe results in a relatively small lattice expansion. An important finding is that high energy milling of $LiAlH_4$/n-Fe results in H_2 desorption during milling when the volumetric lattice expansion increases above 1%.

We put forward the following hypothesis. We postulate that the Fe and Ni ions are able to dissolve in the lattice of $LiAlH_4$, replacing Al and forming Fe or Ni substitutional solid solutions of either the $LiAl_{1-x}Fe_xH_4$ or $LiAl_{1-x}Ni_xH_4$ type. This is

similar to a well-known mechanical alloying phenomenon. Since the ionic radius of 77 pm for Fe is much larger than 53 pm for Al [28], the lattice expansion increases. In contrast, the ionic radius of Ni is 69 pm [28] and the volumetric lattice expansion is smaller (Fig.7.4). In general, the amount of ions dissolved in the $LiAlH_4$ lattice grows with the increasing total energy of milling per unit mass of powder generated within a prescribed milling time. The diffusivity of various types of ions during ball milling (e.g., Fe vs. Ni), however, also seems to affect the amount of dissolved ions; we observed a smaller lattice expansion for n-Ni as compared to n-Fe in Fig.7.4 for the same amount of total energy of milling.

Particle size (micrometric vs. nanometric) is also a factor because both m-Fe and m-Ni result in a smaller expansion than their nanometric counterparts for the same total energy of milling (Fig.7.4). The most effective is n-Fe, for which the largest volume expansion of 1.4% is observed just after 15 min under high energy milling (Table 7.1 and Fig.7.4). For the same amount of total milling energy, the m-Fe additive leads to a lattice expansion < 1% and the n-Ni additive to 0.1-0.5% (Table 7.1 and Fig.12. 4). At a certain critical lattice expansion of $LiAlH_4$, most likely close to 1% (as can be seen in Fig.7.4), the decomposition of $LiAlH_4$ according to reaction (5-9) is triggered. It should be noted that the mechanism of accelerated decomposition of $LiAlH_4$ seems not to be a typical catalytic mechanism (in which a catalyst is supposed to boost the surface formation of molecular H_2 from the atomic hydrogen escaping from the bulk). Although Xiao et al. [127] reported a lattice expansion for $NaAlH_4$ co-doped with Ti and Zr (both having much larger ionic radii than Al [143]), so far, the formation of Fe

solid solution in $LiAlH_4$, and the resulting lattice expansion followed by its accelerated decomposition into Li_3AlH_6 during ball milling, has not been reported in the literature.

7.1.2. Thermal events and microstructural evolution during continuous heating in DSC

Fig. 12 5a–e show the evolution of DSC curves with either μ-Fe or n-Fe additive and ball milling energy for the ($LiAlH_4$+5 wt.% μ-Fe/n-Fe) nanocomposite. The DSC curves for the nanocomposites ball milled with the μ-Fe pre-milled for 1, 3 and 10h clearly exhibit five thermal peaks (where peaks designated 1 and 3 are exothermic and 2, 4 and 5 are endothermic). As discussed in Chapter 5, exothermic peak 1 is most likely formed due to the reaction of the surface aluminum-hydroxyl groups as first reported by Block and Gray [144].

Endothermic peak 2 is due to the melting of $LiAlH_4$. Regarding exothermic peak 3, it was reported in [74] that, in reality, it is a superposition of three events: (a) the decomposition of molten $LiAlH_4$, (b) initial decomposition of Li_3AlH_6 according to the reaction (1-13) and (c) solidification of Li_3AlH_6. The broad endothermic peak 4 is due to the final decomposition of remaining Li_3AlH_6 in solid state according to reaction (1-13). Finally, the endothermic peak 5 at around 400°C is usually ascribed to the decomposition of LiH, which was formed as a result of decomposition of Li_3AlH_6 in reaction (1-13). As argued in [75], and as will be shown later, peak 5 can alternatively be related to the formation of intermetallic compounds. If the decomposition of LiH occurs around peak 5, however, it has no practical value since the temperature is too high. An important finding in Fig.7.5a-c is that the addition of

μ-Fe does not eliminate the initial melting of $LiAlH_4$ and the initial decomposition reactions, like (5-10), occur through a partially molten state.

The situation changes, however, if 5 wt.% n-Fe is added to $LiAlH_4$ (as can be seen in Fig.7.5d for the nanocomposite ball milled under high energy mode IMP68-4B-R132 15min (Q_{TR}=18.2 kJ/g). As illustrated, the melting peak 2 disappears; peaks 1 and 3 merge into one exothermic peak, 1/3, the peak temperature of which is shifted to lower temperature of 132.1°C as compared to Fig. 5a-c. Peak 4 still remains visible, but its peak temperature is also shifted to a lower temperature of 203.2°C. It must be pointed out that the ball milling of ($LiAlH_4$+5 wt.% n-Fe) under this amount of injected milling energy (Q_{TR}=18.2 kJ/g) leads to the release of a small quantity of H_2 due to a partial decomposition of $LiAlH_4$ into Li_3AlH_6 (as shown in Fig.7.3a and b, respectively). In order to check if that decomposition affects the DSC thermal behavior, we also investigated a sample ball milled under low energy mode LES6-4B-15 min (Q_{TR}=6.125 kJ/g); this sample did not release hydrogen and its DSC curve is shown in Fig.7.5e. It is clearly seen that this curve is quite similar to the one in Fig.7.5d for high energy ball milling, with the exception that the weak traces of peaks 2 and 3 can still be recognized, indicating a presence of a negligibly small melting event.

Apparently, high energy ball milling of $LiAlH_4$ containing a nanometric Fe additive—which results in a heavy nanostructuring and an intimate contact between the hydride and additive phases—is really needed for the complete elimination of melting of $LiAlH_4$ in DSC thermal studies. It must also be indicated that the DSC thermal behavior in Fig.7.5d for n-Fe is nearly identical to the one observed for the n-Ni additive in [72,75]. Apparently, both Fe and Ni nanometric metallic additives, ball

milled with $LiAlH_4$ under high energy mode, modify its DSC thermal behavior in exactly the same way by completely eliminating melting of $LiAlH_4$ and merging peaks 1 and 3.

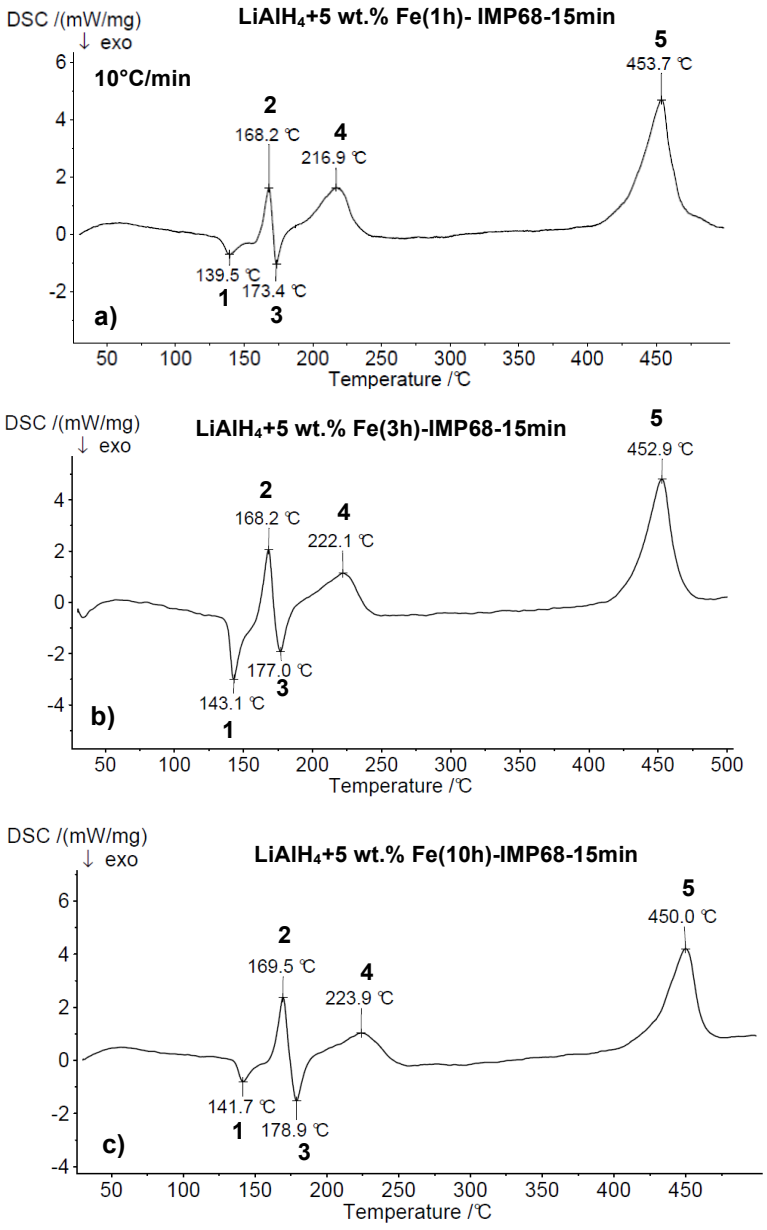

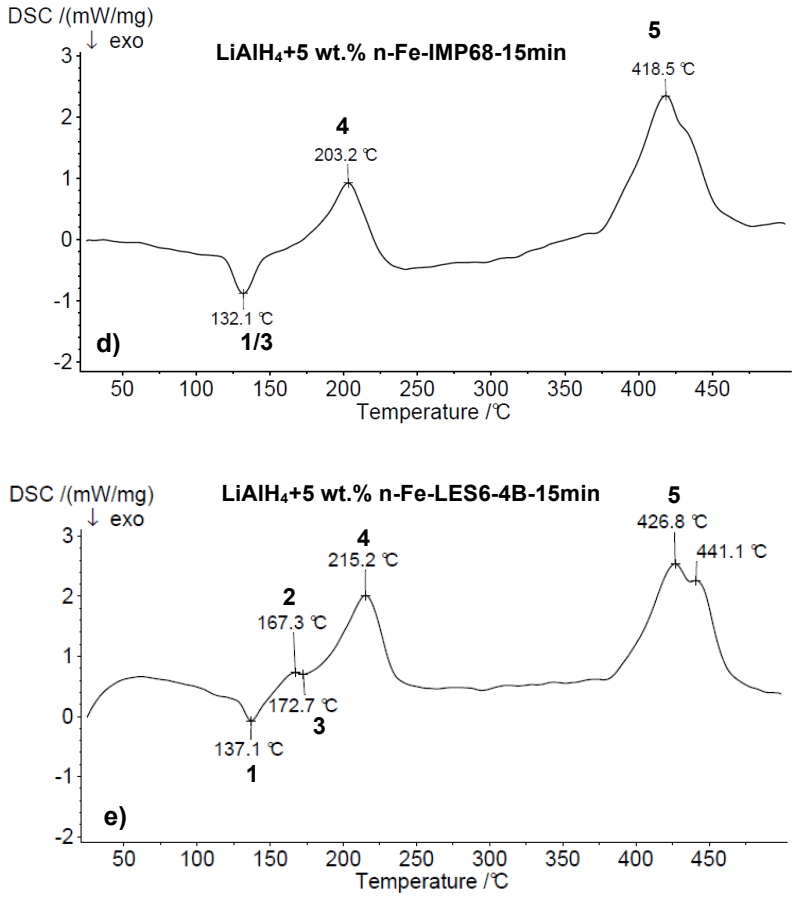

Fig.7.5 DSC curves after ball milling under (IMP68-4B R132) for 15 min (Q_{TR}=18.2 kJ/g) for $LiAlH_4$ containing (a) 5 wt.% m-Fe pre-milled for 1 h (m-Fe (1 h)), (b) 3 h (m-Fe (3 h)) and (c) 10 h (m-Fe (10 h)), (d) 5 wt.% n-Fe and milling modes for 15 min and (e) 5 wt.% n-Fe milled under LES6 mode with four steel balls (4B) (Q_{TR}=6.13 kJ/g). Heating rate in DSC was 10°C/min (Adapted from [42]).

In order to shed more light on the nature of the reactions occurring during a DSC test, the high energy ball milled ($LiAlH_4$+5 wt.% n-Fe) nanocomposite was subjected to a thermal sectioning in DSC at pre-determined temperatures following the procedure outlined in [72,74,75]. As shown in Fig.7.6a, each DSC heating test was stopped at a temperature of 100, 140, 210, 300, 415 and 500°C, respectively. After stopping the

test, the powder sample was immediately extracted from a crucible for an XRD test. The corresponding XRD patterns are shown in Fig.7.6b.

The microstructure of powder stopped at 100°C before peak 1/3 (Fig.7.6 a) consists of a principal phase $LiAlH_4$, and secondary phases such as: Li_3AlH_6 (from reaction (5-10) during ball milling); Al (as received impurity [72,74,75] and possibly coming from reaction [5-10] during ball milling); $LiOH \cdot H_2O$ (as received impurity); and Fe (additive). The microstructure of powder stopped at 140°C just after peak 1 consists of a principal phase Li_3AlH_6 (from reaction [5-10] during heating), as well as a secondary phase Al and the Fe additive. This latter phase composition clearly indicates that peak 1/3 in Fig.11.6a corresponds to a total decomposition of $LiAlH_4$ into Li_3AlH_6, Al and H_2 according to reaction (1-12). The microstructure of powder stopped at 210 and 300°C, just after peak 4 and in the mid of the DSC plateau, consists of a principal phase Al and secondary phases LiOH and LiCl. LiOH may form as a result of hydrolysis/oxidation of a fraction of LiH because, as mentioned in the Experimental section, the milled powder was transported to a DSC instrument in a glass vial filled with Ar and then quickly loaded into a DSC Al_2O_3 crucible. Usually this operation takes a short while and, for that period of time, the powder could be in contact with air. Alternatively, LiOH could be formed due to decomposition of the $LiOH \cdot H_2O$ impurity. Most likely, though, LiCl “as received” has an impurity arising from the industrial synthesis of $LiAlH_4$ [30]. It is clear that the endothermic peak 4 corresponds to the decomposition of Li_3AlH_6 as described by reaction (1.12). At 415 and 500°C, just before and after peak 5, an intermetallic compound LiAl appears in

the microstructure, which indicates that the reaction (1-14) can be assigned to peak 5 as already discussed in Chapter 1.

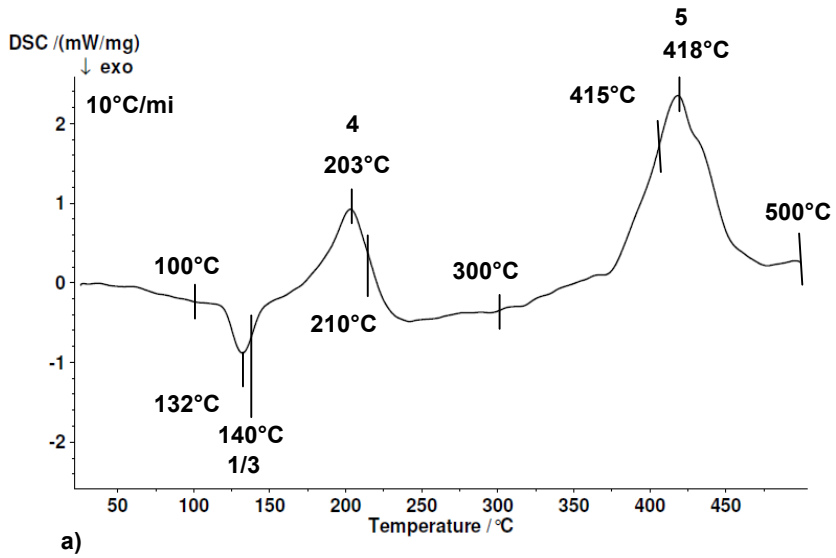

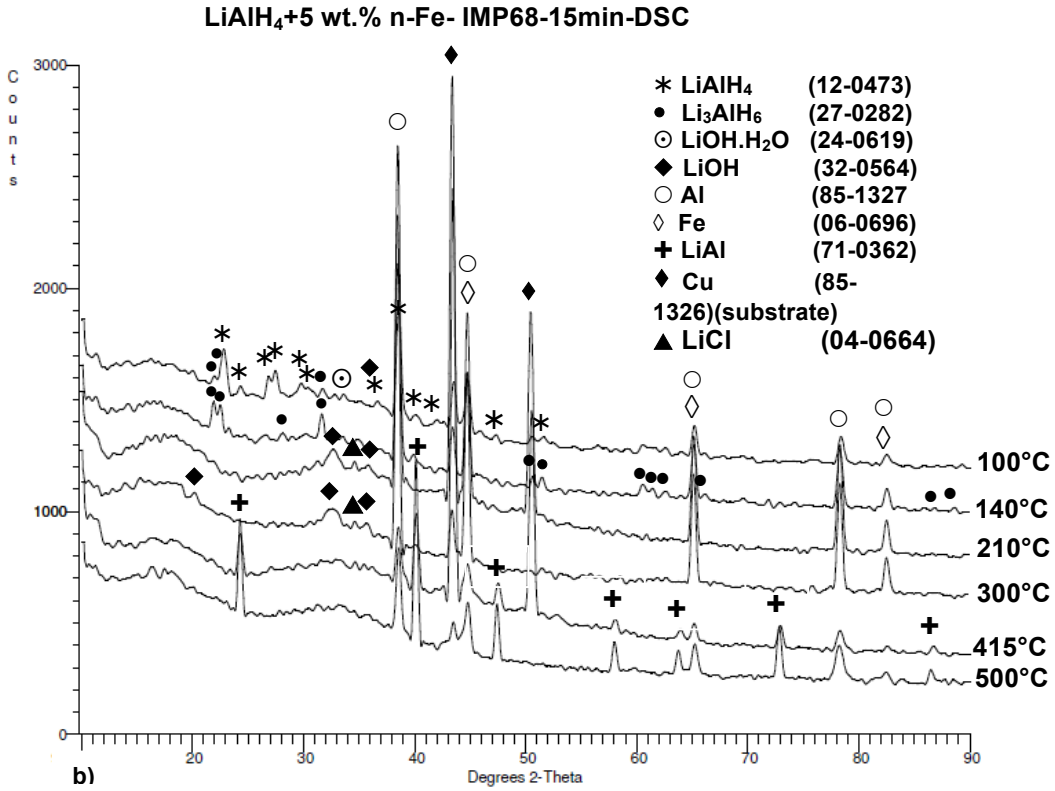

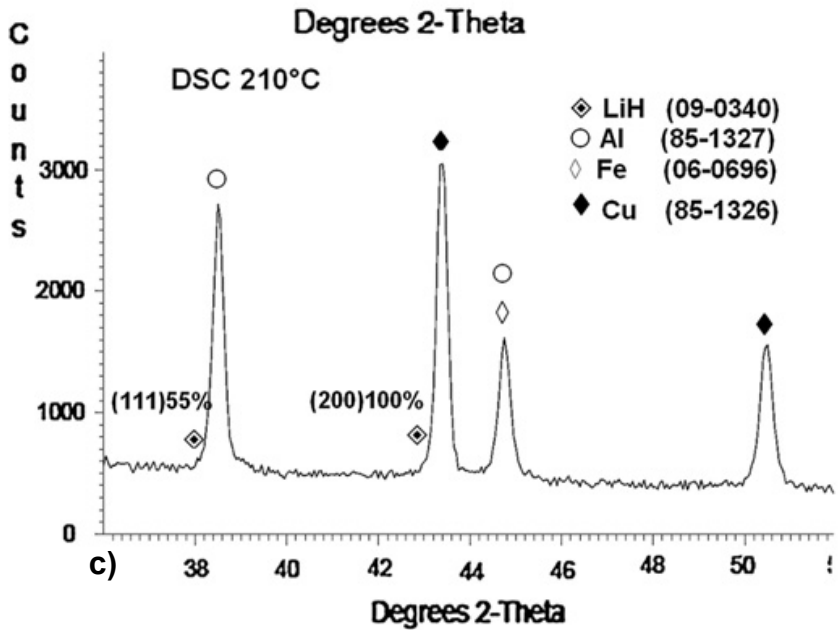

Fig.7.6 (a) DSC curve for ($LiAlH_4$+5 wt.% n-Fe) ball milled under (IMP68-4B R132) for 15 min (Q_{TR}=18.2 kJ/g). Vertical lines indicate the temperatures where the test was stopped and samples were taken for XRD studies. (b) XRD patterns corresponding to temperatures in (a). (c) Enlargement of the section of the XRD pattern section obtained after DSC performed up to 210°C. ICDD file numbers are shown for peak identification (Adapted from [42]).

7.1.3. Isothermal dehydrogenation

The ($LiAlH_4$+5 wt.% μ-Fe/n-Fe) composites were dehydrogenated isothermally at 100, 110, 130, 160 and 200°C at 1 bar H_2 pressure in a Sieverts-type apparatus. Their dehydrogenation curves are shown in Fig.7.7. The composite with 5 wt.% μ-Fe (10h) ball milled under high energy IMP68-4B-R132 mode for 15 min desorbs a full H_2 capacity of ~ 7.6 wt.% at 200°C (Fig.7.7a), which clearly indicates that no measurable hydrogen desorption occurred during ball milling. The composite with 5 wt.% n-Fe ball milled under high energy IMP68 mode for 15 min desorbs ~7 wt.% H_2 at 200°C (Fig.7.7b), which indicates that a small quantity of H_2 was already desorbed during ball milling. The same composite ball milled for 1h desorbs barely 6 wt.% H_2

at 200°C (Fig.7.7c), confirming a substantial H_2 desorption that occurred during ball milling. A change of the milling mode to a low energy LES6-4B R132 mode, however, allows the composite with 5 wt.% n-Fe to desorb a full capacity of ~7.6 wt.%H_2 (Fig.7.7d). Therefore, the dehydrogenation curves in Fig.7.7 confirm the following facts: (a) the additive of micrometric size Fe (m-Fe) does not induce an H_2 desorption during milling even under a high energy mode; and (b), the additive of nanometric Fe (n-Fe) triggers a substantial mechanical dehydrogenation (while no dehydrogenation occurs during milling under a low energy milling mode). The results shown in Fig.7.7 are in good agreement with the H_2 desorption plot in Fig.7.3a and the volume expansion changes in Fig.7.4.

After dehydrogenation of the 5 wt.% n-Ni composite ball milled under IMP68 mode at each pertinent temperature (Fig.7.7b), the powder was taken for XRD tests and the corresponding XRD patterns are shown in Fig.7.8. The easily seen diffraction peaks of Li_3AlH_6 confirm that, at the lower temperature range of 100 and 110°C within 25h (Fig.7.7), the H_2 desorption occurs by decomposition of $LiAlH_4$ into Li_3AlH_6 and Al in a full accord with reaction (1-12). At the temperature range 130-200°C, reaction (1.13) is accelerated, which allows desorbing a full H_2 capacity at 200°C.

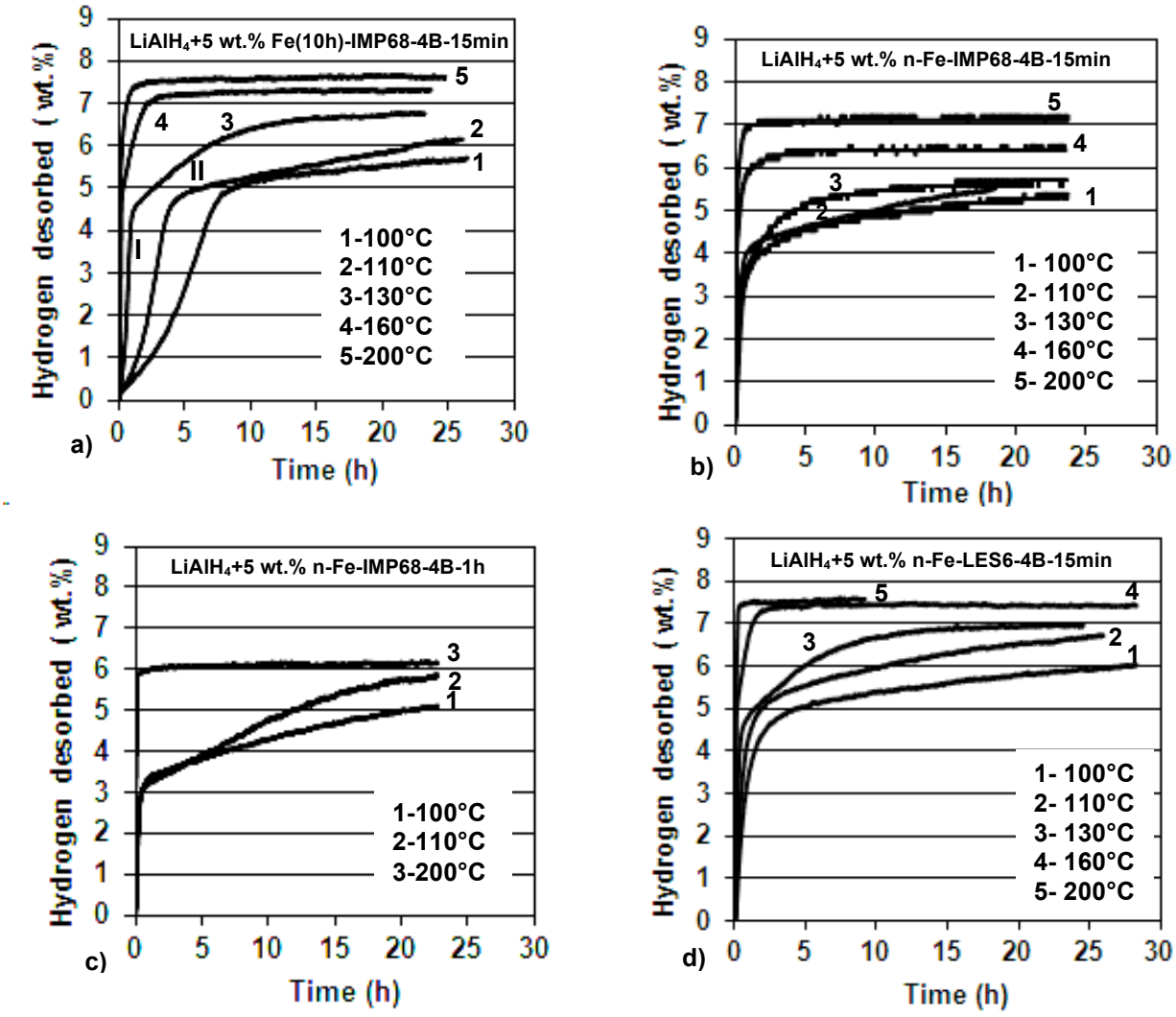

Fig.7.7 Volumetric dehydrogenation curves at varying temperatures after ball milling under the high energy IMP68-4B R132 mode for $LiAlH_4$ containing (a) 5 wt.% m-Fe (10 h) milled for 15 min (Q_{TR}=18.2 kJ/g), (b) 5 wt.% n-Fe milled for 15 min, (c) 5 wt.% n-Fe milled for 1 h (Q_{TR}= 72.8 kJ/g), and (d) 5 wt.% n-Fe milled under the LES6-4B R132 15min (Q_{TR}=6.13 kJ/g). mode (Adapted from [42]).

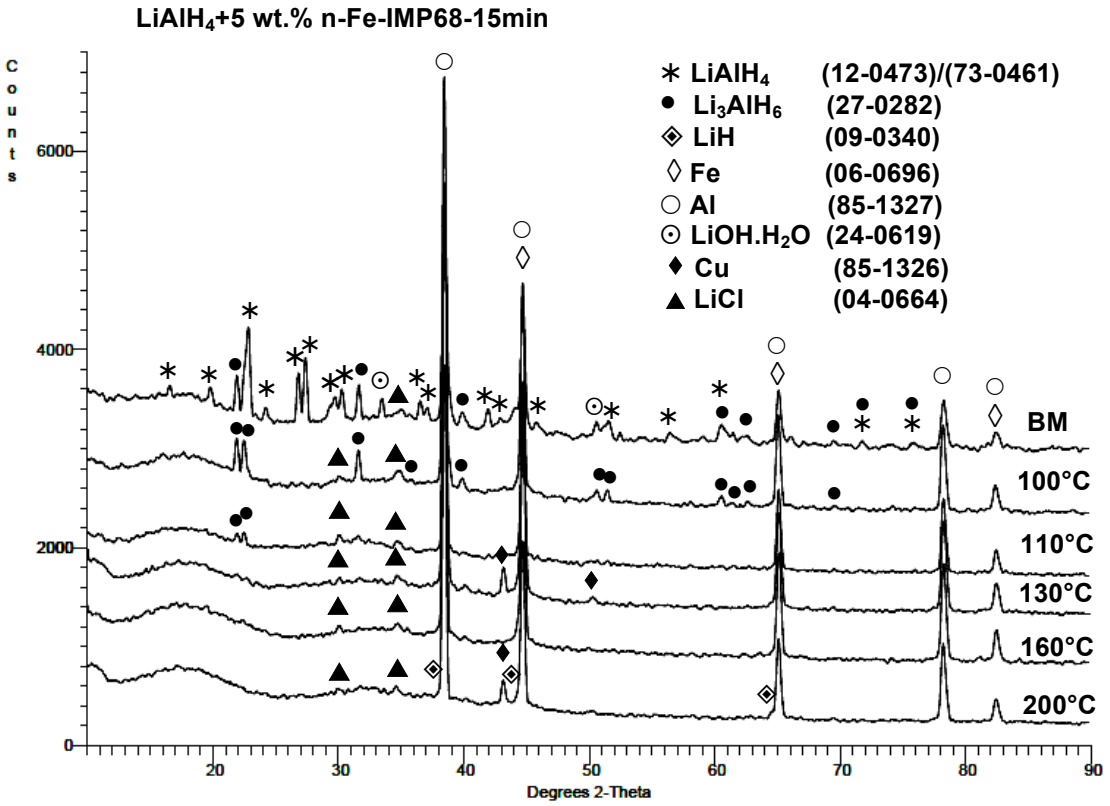

Fig.7.8 XRD patterns after dehydrogenation at varying temperatures corresponding to Fig.7.7b for $LiAlH_4$ containing 5 wt.% n-Fe ball milled under (IMP68-4B R132) for 15 min (Q_{TR}=18.2 kJ/g). ICDD file numbers are shown for peak identification (Adapted from [42]).

From the slopes of dehydrogenation curves, such as those in Fig.7 7, the apparent activation energy was calculated for Stage I and II dehydrogenation as designated in Fig.7.7a. Stage I and II correspond to the dehydrogenation according to reaction (1-12) and (1-13), respectively. The Arrhenius-type plots of the rate constant k in Eq. (7.2) vs. temperature are shown in Fig.7.9 for dehydrogenation in Stage I and II. It is evident that the experimental fit to Eq. (7.2) is excellent as reflected in the values of the fit coefficient R^2 (which are much greater than 0.9). The obtained values of the apparent activation energies are listed in Table 7.2. Fig. 7.10 shows a bar graph

comparison of the obtained apparent activation energies for dehydrogenation in Stage I (Fig. 7.10a) and Stage II (Fig.7.10b).

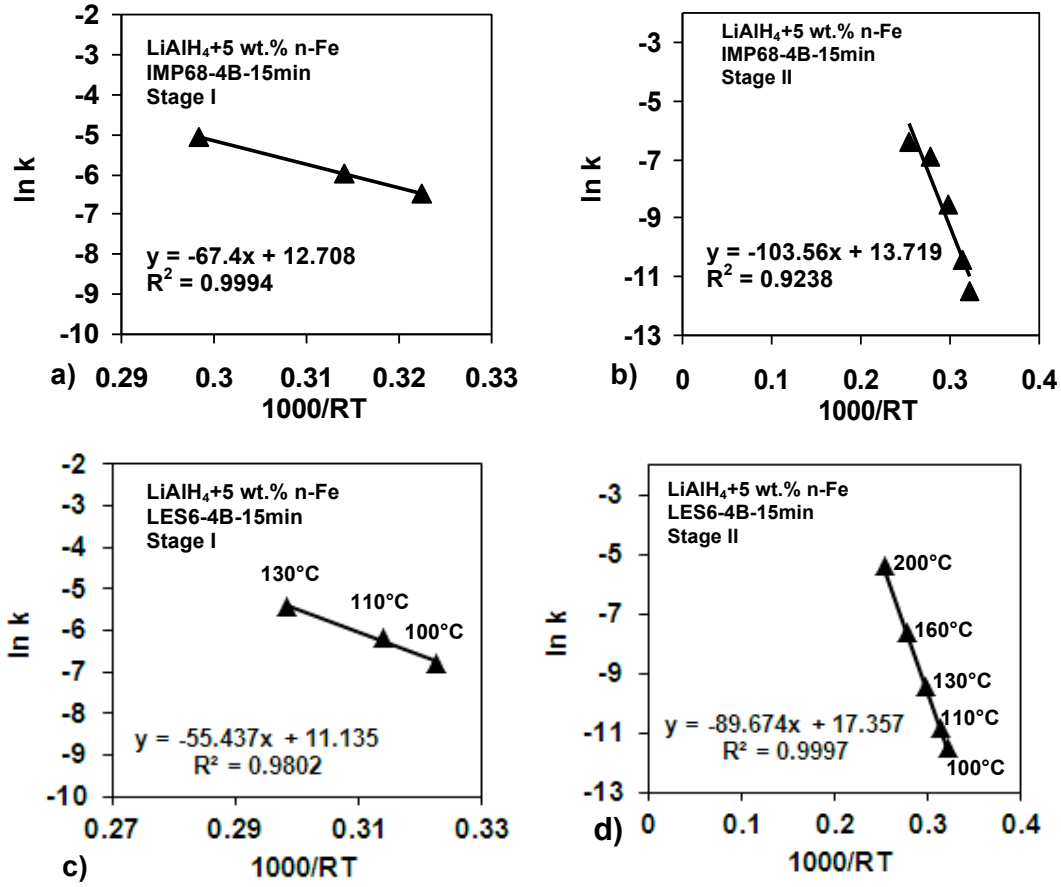

Fig.7.9 The Arrhenius plots of the rate constant k vs. temperature for estimation of the apparent activation energy of hydrogen desorption for ($LiAlH_4$+5 wt.% n-Fe) ball milled for 15 min under the high energy (IMP68-4B R132 (Q_{TR}=18.2 kJ/g).) mode for (a) Stage I and (b) Stage II desorption as well as ball milled under the low energy (LES6-4B) mode for 15 min (Q_{TR}=6.13 kJ/g). for (c) Stage I and (d) Stage II desorption (Adapted from [42]).

Table 7.2. Apparent activation energies of dehydrogenation for $LiAlH_4$ with the m-Fe and n-Fe additive ball milled under high energy (IMP68) and low energy (LES6) milling modes .

Additive/milling mode	Apparent activation energy ± standard error (kJ/mol)	
	Stage I	Stage II
m-Fe(1h)/IMP68-4B	76.2±5.7	85.1±15.0
m-Fe(3h)/IMP68-4B	95.6±16.8	93.5±0.2
m-Fe(10h)/IMP68-4B	87.9±0.2	84.8±0.0
n-Fe/IMP68-4B	67.4.5±8.0	76.6 ±3.2
n-Fe/LES6-4B	55.4±4.0	89.7±9.8

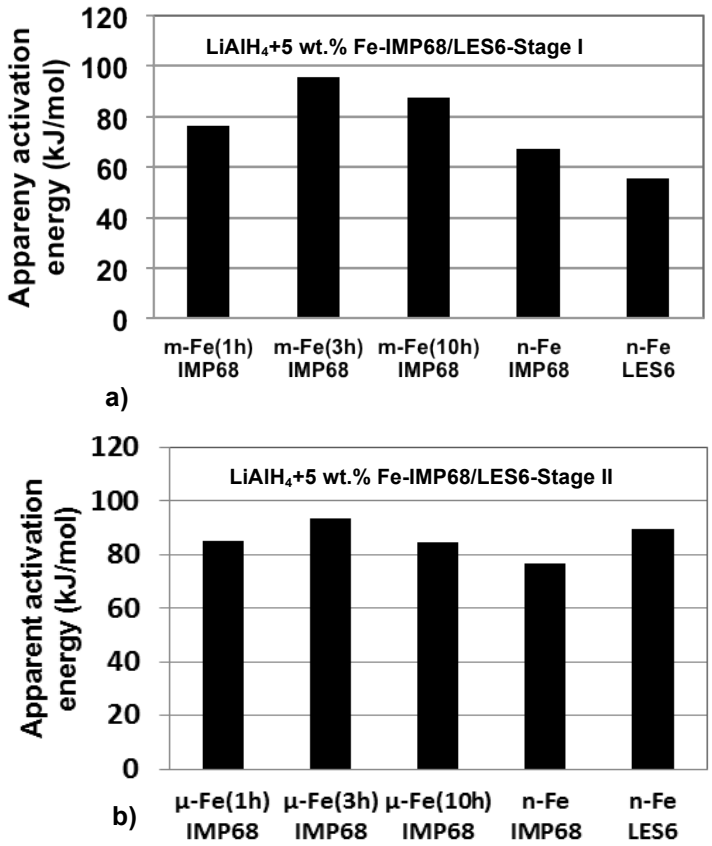

Fig. 7.10 Bar graph comparison of the apparent activation energies for ($LiAlH_4$+5 wt.% n-Fe/n-Fe) ball milled for 15 min under (IMP68-4B R132 (Q_{TR}=18.2 kJ/g)) and (LES6-4B R132 (Q_{TR}=6.13 kJ/g).) milling modes for (a) Stage I and (b) Stage II (as designated in Fig.7 7a) (Adapted from [42]).

It is clear from Table 7.2 that the μ-Fe additive, regardless of its pre-milling time in Stage I renders the average apparent activation energy within the range of 76-96 kJ/mol. However, the n-Fe additive renders a drastically smaller energy at the order of 67 kJ/mol. It is interesting to note that, within the experimental error, there is no great difference between the activation energy for the composite milled under high energy mode IMP68-4B-15 min (which resulted in some H_2 desorption during milling) and the one milled under low energy LES6-4B-15 min (which did not desorb H_2 during milling).

For Stage II dehydrogenation, within the experimental error, the average apparent activation energy seems to fall within the range 85-90 kJ/mol, regardless of the Fe particle size (μ-Fe or n-Fe) and milling energy (IMP68 or LES6 mode). For the first time, this clearly shows that, for $LiAlH_4$, the catalytic additive is able to strongly reduce the apparent activation energy of Stage I dehydrogenation (reaction [5-10]), but does not affect substantially the Stage II dehydrogenation (reaction [1-13]). This behaviour is a good indicator that most efforts should be devoted to the acceleration of the dehydrogenation rate in Stage II (reaction [1-13]).

Figure 7.11 shows a comparison of the effect of 5 wt.% of nanometric Fe (n-Fe) and milling mode obtained in this work with the nanometric Ni (n-Ni) on the dehydrogenation behavior at 100°C (which is a maximum temperature limit suitable for a PEM fuel cell stack). It is observed that, at such a low temperature, the dehydrogenation curves (2 results) for the composite containing n-Fe milled under a low energy mode (LES6-4B) exhibit a slightly lower rate of H_2 dehydrogenation in both Stage I and II than their counterpart milled under higher energy mode (IMP68-

2B). This effect is possibly related to a better structural refinement obtained under higher milling energy. It must be pointed out that, under both modes, there was no desorption of H_2 during milling and the volumetric lattice expansion is much less than 1% (see Fig.7.4). Also, it is observed in Fig. 7.11 that the dehydrogenation curves for both additives n-Fe and n-Ni are very close to one another, indicating that at 100°C both nanometric additives provide nearly identical enhancement of dehydrogenation rate.

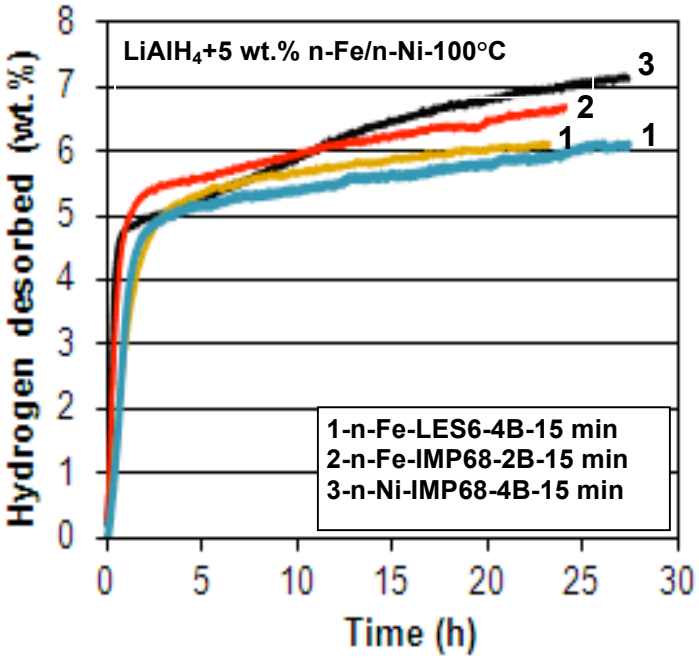

Fig. 7.11 A comparison of volumetric dehydrogenation curves at 100°C for $LiAlH_4$ containing 5 wt.% n-Fe ball milled for 15 min under the low (LES6-4B R132 (Q_{TR}=6.13 kJ/g)) and higher energy (IMP68-2B R132 (Q_{TR}=9.15 kJ/g)) mode as compared to the dehydrogenation curve for the 5 wt.% n-Ni additive (Adapted from [42]).

Ball milled ($LiAlH_4$+5 wt.% n-Fe) is slowly able to self-discharge large quantities of H_2 during storage at room temperature (RT), 40 and 80°C, as shown in Fig. 7.12 (in comparison to the data for n-Ni extracted from [75]). The ball milled nanocomposite

powders were stored in Ar filled and sealed glass vials. Small samples were extracted from the vial after a pre-determined time of storage; the quantity of H_2 desorbed was measured from a dehydrogenation curves at 250°C as shown in Fig. 7.12. Fig. 7.13 shows the XRD patterns obtained from samples stored for 20 days at room temperature (RT) and 40°C. For both temperatures, a mixture of $LiAlH_4$ and Li_3AlH_6 hydride phases is clearly observed. A 100% intensity peak of $LiAlH_4$ at $2\theta=22.83°$ has a lower intensity after storage at 40°C than its counterpart after storage at RT. Conversely, the nearby 100% twin peaks of Li_3AlH_6 (at $2\theta=21.92$ and 22.53°) have higher intensities after storage at 40°C than their counterparts after storage at RT. The diffraction patterns clearly indicate that, during long-term storage, there is a slow H_2 discharge through a solid state decomposition of $LiAlH_4$ through reaction (5-10) as similarly observed for the n-Ni additive in [75]. When the storage temperature increases to 80°C (Fig. 12.12c), the H_2 quantity discharged from ball milled ($LiAlH_4$+5 wt.% n-Fe) reaches about 6 wt.% after 15 days (which must have involved reaction (1.13)). It is interesting that both nanometric catalysts n-Fe and n-Ni give nearly identical quantities of slowly discharged H_2. Sandrock et al. [121] note the practical significance of such a behaviour for long-duration, low-demand devices that use H_2 (such as low-power remote fuel cells or portable gas analyzers). These materials can also be used in a number of chemical processes where a continuously reducing atmosphere is needed for a completion of the process. As well, they can have an application in the military sector for long-term cartridges that supply hydrogen to portable devices for use by soldiers on a mission.

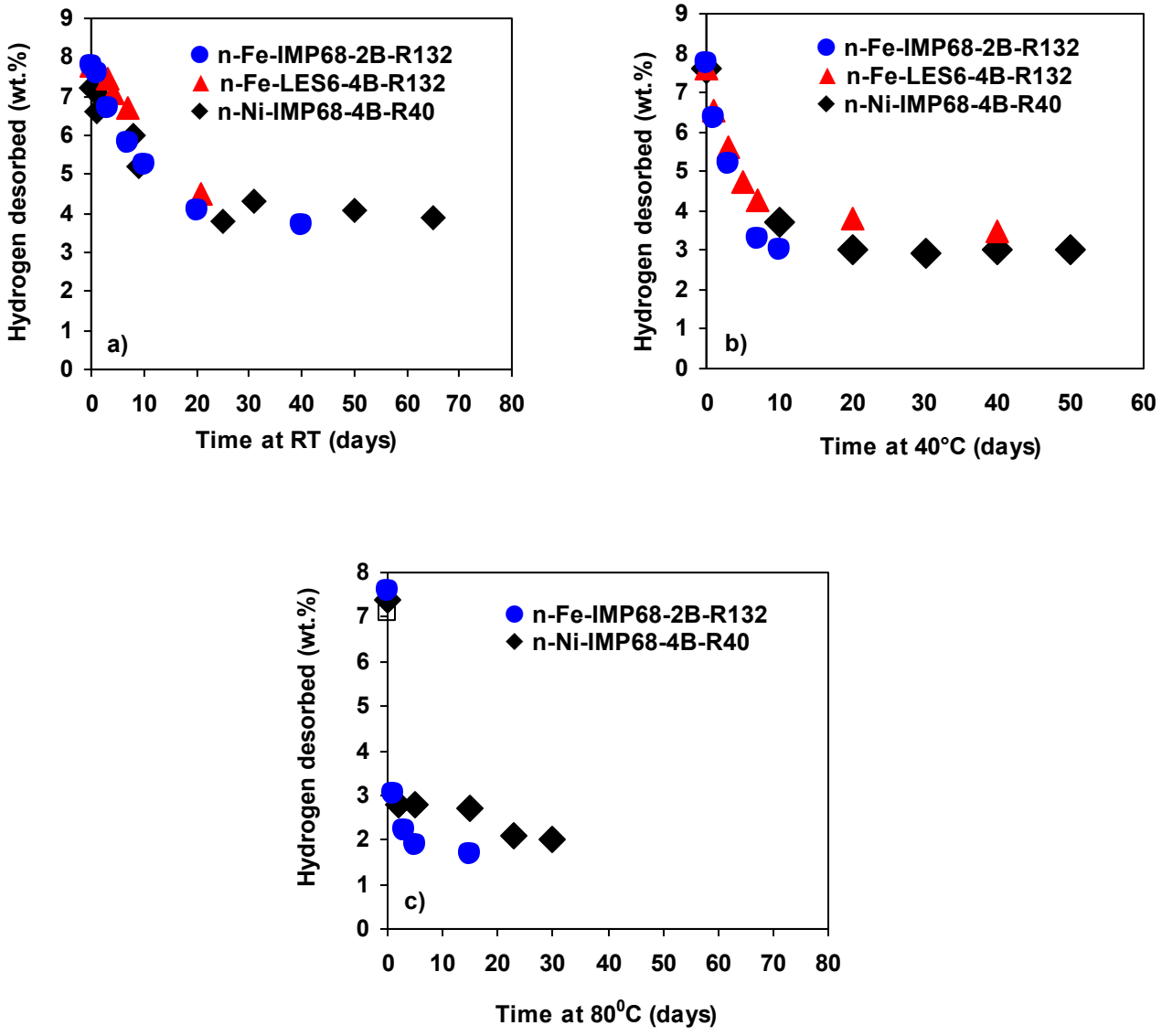

Fig. 7.12 Plots of hydrogen desorbed vs. storage time in days for ball milled $LiAlH_4$ containing 5 wt.% n-Fe compared with the data for the 5 wt.% n-Ni additive extracted from [75]. (a) Stored at room temperature (RT) under Ar subsequently desorbed at 250°C for n-Fe and 140°C for n-Ni. (b) Stored at 40°C under Ar; subsequently desorbed at 250°C for n-Fe and 170°C for n-Ni. (c) Stored at 80°C under Ar; subsequently desorbed at 250°C for n-Fe and 170°C for n-Ni. All dehydrogenations carried out at 1 bar H_2 pressure (Adapted from [42]).

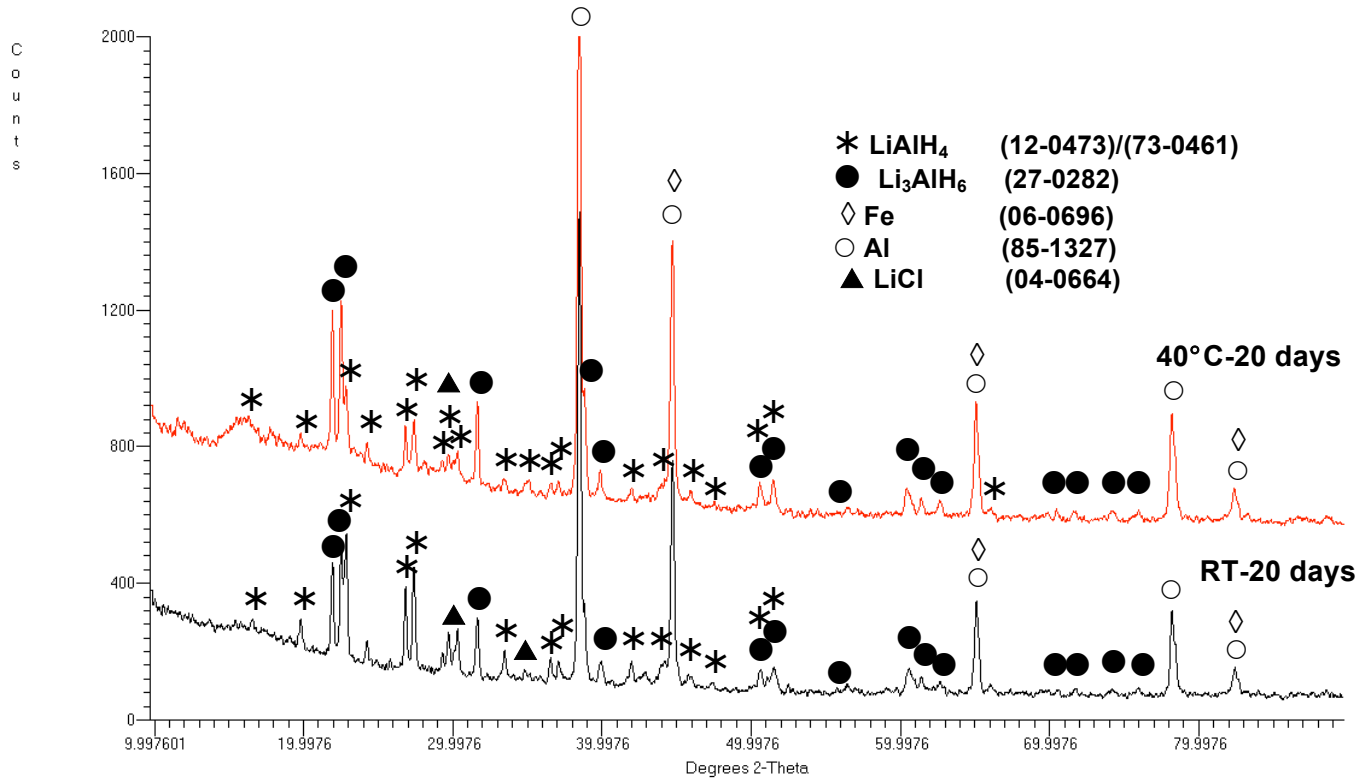

Fig. 7.13 XRD patterns obtained for a ($LiAlH_4$+5 wt.% n-Fe) composite ball milled under the low energy mode (LES6-4B R132) for 15 min (Q_{TR}=6.13 kJ/g)and subsequently stored for 20 days under Ar at room temperature (RT) and 40°C. ICDD file numbers are shown for peak identification (Adapted from [42]).

7.1.4. Rehydrogenation

In order to study the feasibility of rehydrogenation, first the sample was fully dehydrogenated at 200°C at 1 bar H_2 pressure. This was followed by a rehydrogenation step at 160°C at 100 bar H_2 pressure for 24h as shown in Fig. 7.14a. These dehydrogenation-rehydrogenation steps were repeated 3 times in order to determine the reproducibility of the results. Fig. 7.14a shows the reproducibility of both steps as excellent. It is clearly observed that after each dehydrogenation step,

the amount of desorbed H_2 is equal to 0.5 wt.%. The XRD pattern after rehydrogenation in Fig. 7.14b visibly shows the presence of a small diffraction peak whose 2θ position corresponds to the 2θ position of the (111) 100% intensity Li_3AlH_6 peak (JCPDS # 27-0282). This confirms that, indeed, a partial rehydrogenation from a mixture of LiH and Al into Li_3AlH_6 (inverse reaction (1.13) occurred during the rehydrogenation step, which, in the following dehydrogenation step, is able to desorb about 0.5 wt.% H_2. Apparently, a partial rehydrogenation for the ($LiAlH_4$+5 wt.% n-Fe) nanocomposite is difficult but not impossible.

In general, there have been a number of rehydrogenation attempts for $LiAlH_4$ ball milled with various catalytic precursors. Some of the trials, for such catalytic precursors as $TiCl_3$ (125°C/~80 bar H_2/16h) [34], TiF_3 (20-200°C/95 bar H_2/6h) [60], NbF_5 (170°C/75 bar H_2/2.5h) [11] and n-Ni (55-250°C/2-100 bar H_2/2-64h) [72], were reported to be unsuccessful. Other researchers, however, have reported a partial dehydrogenation/rehydrogenation according to reaction (1.13) for such catalytic precursors as $TiCl_3 \cdot 1/3AlCl_3$ (175°C/40 bar H_2/13h)[49], VCl_3/carbon nanofibers (110°C/20 bar H_2/6h) [145] and TiC (165°C/95 bar H_2/3h) [49].

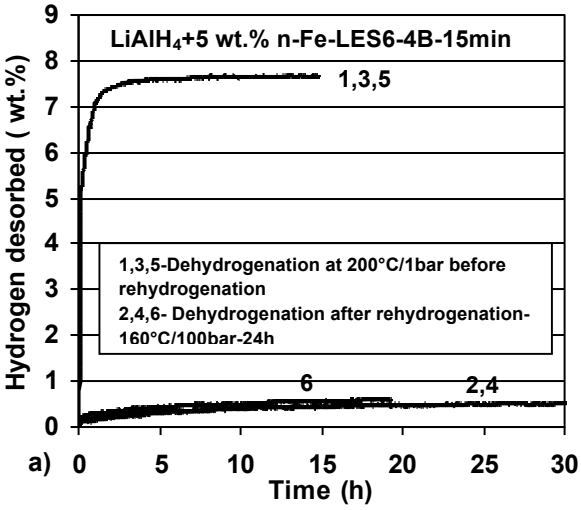

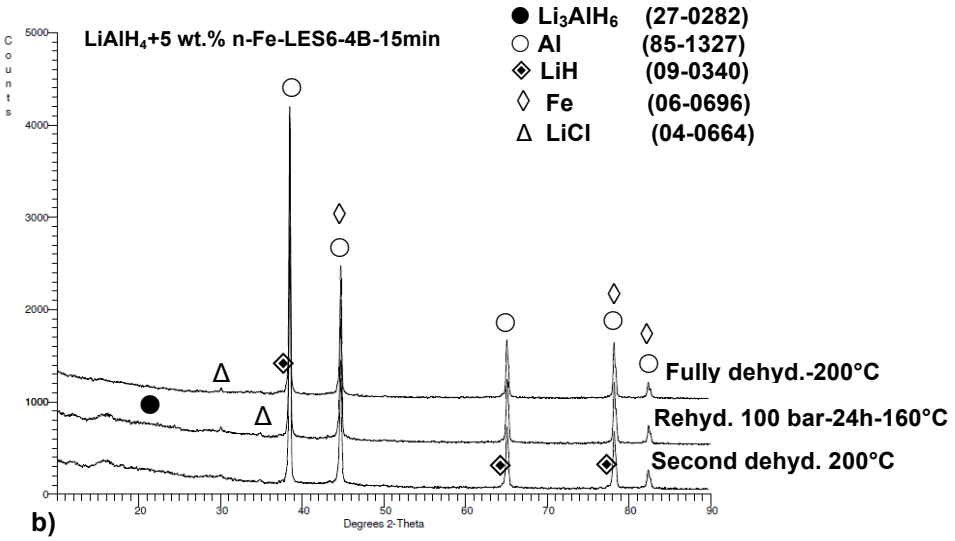

Fig.7.14 (a) Volumetric dehydrogenation/rehydrogenation curves for $LiAlH_4$ containing 5 wt.% n-Fe ball milled under the low energy (LES6-4B R132 15 min (Q_{TR}=6.13 kJ/g)) mode without H_2 desorption during milling. (b) Corresponding XRD patterns after first dehydrogenation and second dehydrogenation after rehydrogenation. ICDD file numbers are shown for peak identification (Adapted from [42]).

The successful cases of rehydrogenation report the recovered H_2 capacities of 1.8 wt.% [49], 1.9 wt.% [65] and 3.9 wt.% [145]. The result of 3.9 wt.% H_2 reported in [145] seems to be grossly overestimated since the theoretical H_2 capacity of reaction (1.13), which might be reversible, is only 2.6 wt.% H_2 [65]. Nevertheless, the recovered values of 1.8-1.9 wt.% H_2 reported in [49,65] seem to be quite reasonable.

In the present work, we followed the rehydrogenation temperature/pressure conditions reported in [65] for a nanometric TiC additive. Our result of 0.5 wt.% H_2 rehydrogenated is much smaller than that reported in [65], but does confirm that reaction (1-13) is, indeed, reversible. It also shows that there is no universal temperature/pressure/time window for rehydrogenation for all catalytic additives/precursors. Successful rehydrogenation parameters seem to depend on the type of catalytic additive/precursor used and they vary from one to another. It is possible that the rehydrogenation conditions of temperature/pressure/time for the n-Fe additive are still different than those for a nanometric TiC additive. In the next phase of research, we tried to optimize the temperature/pressure/time window for a number of nanometric catalytic additives.

7.1.5. Conclusions

This work represents the first systematic study of the effect of the micrometric (μ-Fe) and nanometric Fe (n-Fe) additives in comparison to micrometric and nanometric Ni additives (μ-Ni and n-Ni) on the reversible hydrogen storage properties of $LiAlH_4$. It has a specific focus on dehydrogenation/hydrogenation behaviour and hydrogen capacity, and is the first paper to investigate the effect of ball-milling energy on the behavior of $LiAlH_4$ containing both μ-Fe and n-Fe additives. In addition, this is also

the first study to employ the isothermal Arrhenius analysis over a wide range of temperature (100–200°C) for two dehydrogenation stages, Stage I (reaction 1.12) and Stage II (reaction 1.13). The main conclusions of this research are summarized as follows:

1. During high energy milling of the ($LiAlH_4$+5 wt.% n-Fe) nanocomposite, a continuous desorption of H_2 is observed reaching ~3.5 wt.% H_2 after 5h of milling. In contrast there is no H_2 desorption during high energy milling of $LiAlH_4$ containing the micrometric Fe (μ-Fe), micrometric Ni (μ-Ni) and nanometric Ni (n-Ni) additives, as well as during the low energy milling of $LiAlH_4$ containing n-Fe.

2. XRD shows that, during high energy milling of $LiAlH_4$ containing n-Fe, there occurs a gradual decomposition of $LiAlH_4$ in solid state according to a well-known reaction: $LiAlH_4$ (solid)$\rightarrow 1/3Li_3AlH_6+2/3Al+H_2$

3. $LiAlH_4$ containing n-Fe is destabilized as a result of a lattice expansion occurring during high energy ball milling; and the lattice expansion of at least 1% and larger results in H_2 desorption during milling.

4. High energy ball milling of $LiAlH_4$ containing μ-Fe, μ-Ni and n-Ni additives, as well as low energy milling of $LiAlH_4$ containing n-Fe ball, results in a smaller volumetric lattice expansion; and there is no H_2 desorption observed during milling.

5. We postulate that both the Fe and Ni ions are able to dissolve in the lattice of $LiAlH_4$, replacing Al and forming a substitutional solid solution of either $LiAl_{1-x}Fe_xH_4$ or $LiAl_{1-x}Ni_xH_4$ type that leads to a various degree of volumetric lattice expansion of $LiAlH_4$ and its destabilization.

6. The amount of dissolved additive ions depends primarily on the amount of milling energy per unit mass of powder generated within a prescribed milling time, the type of additive ions, and the particle size of the metal additive. Since the ionic radius of 77 pm for Fe [120] is much larger than that of Al (which equals 53 pm and is substituted by Fe), the lattice expansion increases. In contrast, the ionic radius of Ni is 69 pm [120] and the volumetric lattice expansion is smaller.

7. During isothermal dehydrogenation at 100°C, the n-Fe and n-Ni additive (the latter used for comparison) provide nearly identical enhancement of dehydrogenation rate.

8. In Stage I, the μ-Fe additive, regardless of its pre-milling time, renders the average apparent activation energy within the range of 76-96 kJ/mol, whereas the n-Fe additive renders drastically smaller energy on the order of 67 kJ/mol.

9. For Stage II dehydrogenation, the average apparent activation energy is within the range 85-103 kJ/mol, regardless of the particle size of the Fe additive (m-Fe vs. n-Fe) and the energy of milling.

10. Apparently, for $LiAlH_4$, the n-Fe catalytic additive is able to strongly reduce the apparent activation energy of Stage I dehydrogenation, but does not substantially affect the apparent activation energy of Stage II dehydrogenation.

11. Ball milled ($LiAlH_4$+5 wt.% n-Fe) is able slowly to self-discharge large quantities of H_2 up to ~5 wt.% during storage at RT, 40 and 80°C.

12. Fully dehydrogenated ($LiAlH_4$+5 wt.% n-Fe) was partially rehydrogenated up to 0.5 wt.% H_2 under 100 bar/160°C/24h; however, the rehydrogenation parameters are not yet optimized.

7.2 The effect of mechanical ball milling and interstitial compound additives (TiC, TiN and ZrC)

7.2.1 Microstructure of ball milled composites

As shown before, the $LiAlH_4$ mixtures containing metallic additives, such as n-Fe and n-Ni, can decompose during highly energetic ball milling and desorb different amounts of hydrogen. In order to find out if the mixtures of $LiAlH_4$ with 5 wt.% n-TiC, n-TiN and n-ZrC exhibit similar behaviour, the pressure change in the milling vial was continuously monitored during the entire length of the process and then converted to wt.% H_2 as explained earlier. Fig. 7.15 shows a trend of increasing the amount of desorbed H_2 during ball milling. The amount of H_2 desorbed during 15 min (Q_{TR}=18.2 kJ/g) of ball milling is zero. When the milling duration was extended to 15 h, however, the H_2 desorption was more substantive, reaching about 4, 1.9 and 0.7 wt.% for n-TiN, n-TiC and n-ZrC respectively. Therefore, the mechanical dehydrogenation curves in Fig. 7.15 confirm that the mechanical dehydrogenation rate (Stage I) of the doped samples increases noticeably during high energy ball milling in the order of TiN > TiC > ZrC, while no H_2 desorption occurs during milling under a low energy milling mode. It can be concluded that the activation energy for mechanical dehydrogenation would most likely have the lowest value for n-TiN additive and the highest value for n-ZrC.

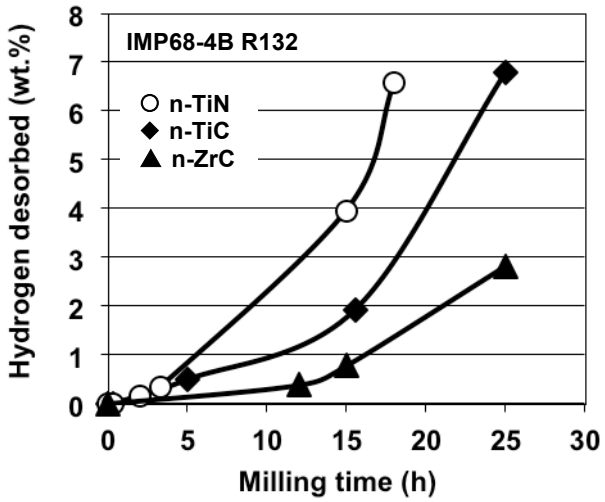

Fig.7.15 The quantity of H_2 desorbed during ball milling (mechanical dehydrogenation) under IMP68-4B R132 (Q_{TR132}=72.8 kJ/gh) milling mode as a function of milling time.

For the purpose of identifying the reactions, which result in the H_2 desorption during ball milling, the XRD patterns were taken from ($LiAlH_4$ + 5 wt.% n-TiC) milled for 15 min, 15 h and 25 h (Fig. 7.16). As evident, after 15 min of ball milling (Q_{TR}=18.2 kJ/g) there is no evidence of the existence of Li_3AlH_6. The diffraction peaks of Li_3AlH_6 appear after 15 h of milling (Q_{TR}=1092 kJ/g), accompanied by decreasing intensity of the $LiAlH_4$ peaks and more H_2 desorption. This trend continues to the complete removal of $LiAlH_4$ and Li_3AlH_6 peaks after 25 h ball milling (Q_{TR}=1820 kJ/g). It is obvious that during high energy milling (Q_{TR132}=72.8 kJ/gh), there is a gradual decomposition of $LiAlH_4$ in solid state according to reactions (1.12) and (1.13).

Reactions (1.12) and (1.13) have a maximum theoretical capacity of 7.9 wt. % H_2 (5.3 and 2.6 wt.% H_2 for Stages I and II, respectively). This capacity will be ~7.4 wt.% (4.9 and 2.4 wt.%H_2) if both the purity and the presence of 5 wt.% of additive are taken into account. Fig. 7.15 shows that nearly 100% of the maximum purity-corrected H_2

capacity of $LiAlH_4$+5 wt.% n-TiN mixture can be desorbed during milling up to 20 h, while the mixture with 5 wt.% n-TiC and n-ZrC releases nearly 57% and 26% of its maximum capacity at the same time.

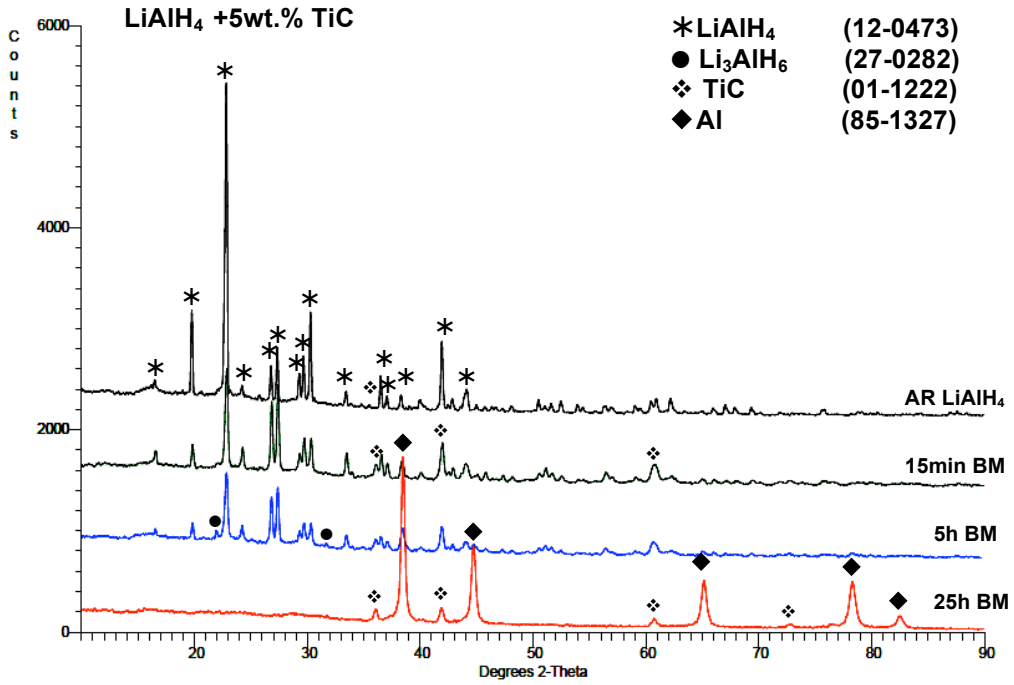

Fig.7.16. XRD patterns after milling of $LiAlH_4$+5 wt.% n-TiC under IMP68-4B R132 milling mode (Q_{TR132}=72.8 kJ/gh) for various times.

7.2.2. Isothermal dehydrogenation

The ($LiAlH_4$+5 wt.% n-TiN/n-TiC/n-ZrC) nanocomposites were dehydrogenated isothermally at 100, 110, 125 and 165°C at 1 bar H_2 pressure in a Sieverts-type apparatus. Their dehydrogenation curves are shown in Fig.7.17. All the composites (ball milled under high energy IMP68-4B R132 mode for 15 min (Q_{TR}=18.2 kJ/g) desorbs a full H_2 capacity of ~ 7.4 wt.% at 165°C (Fig.7.17), clearly indicating that no measurable hydrogen desorption occurred during ball milling.

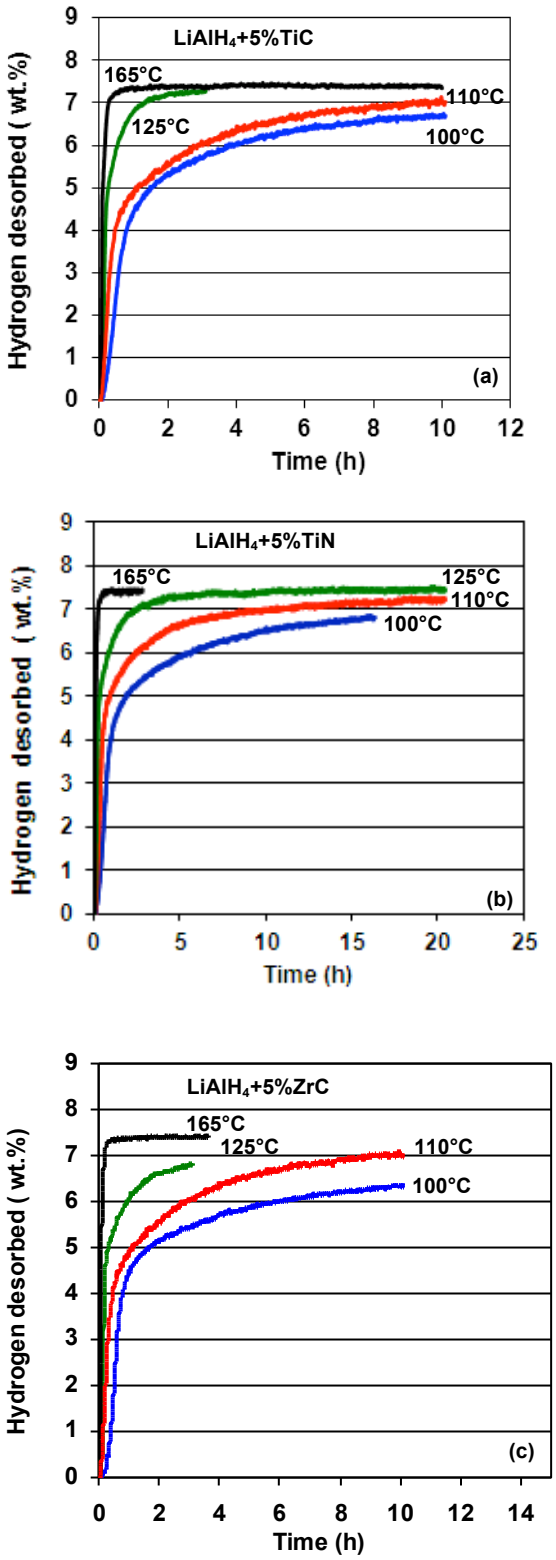

Fig.7.17. Volumetric dehydrogenation curves at varying temperatures after ball milling of $LiAlH_4$ under IMP68-4B R132 15min (Q_{TR}=18.2 kJ/g) containing (a) 5 wt.% n-TiC, (b) 5 wt.% n-TiN, (c) 5 wt.% n-ZrC.

After the dehydrogenation of ball milled composites at each relevant temperature (Fig.7.17 a-c), the powders were taken for XRD tests. The corresponding XRD patterns for maximum and minimum desorption temperatures are shown in Fig. 7.18a-c. The visible diffraction peaks of Li_3AlH_6 in the composites with n-TiC and n-ZrC confirm that, at the lower temperature range of (100°C), the H_2 desorption occurs by decomposition of $LiAlH_4$ into Li_3AlH_6 and Al in a full accord with reaction (1.12). However, these peaks are not observed in the composite containing n-TiN at 100^{o}C. As it can be seen in Fig 7.18b the new phase of LiAl is formed at this temperature. We put forward a hypothesis that the addition of n-TiN eliminates reaction (1.12) and as a results $LiAlH_4$ directly decomposes into LiAl, Al and H_2 according to reaction (1.14). Confirmation of this hypothesis needs more investigation. At the higher temperatures reaction (1.13) is accelerated, which allows for desorbing over 7 wt. % H_2 at 165°C for the samples containing n-TiC and n-ZrC.

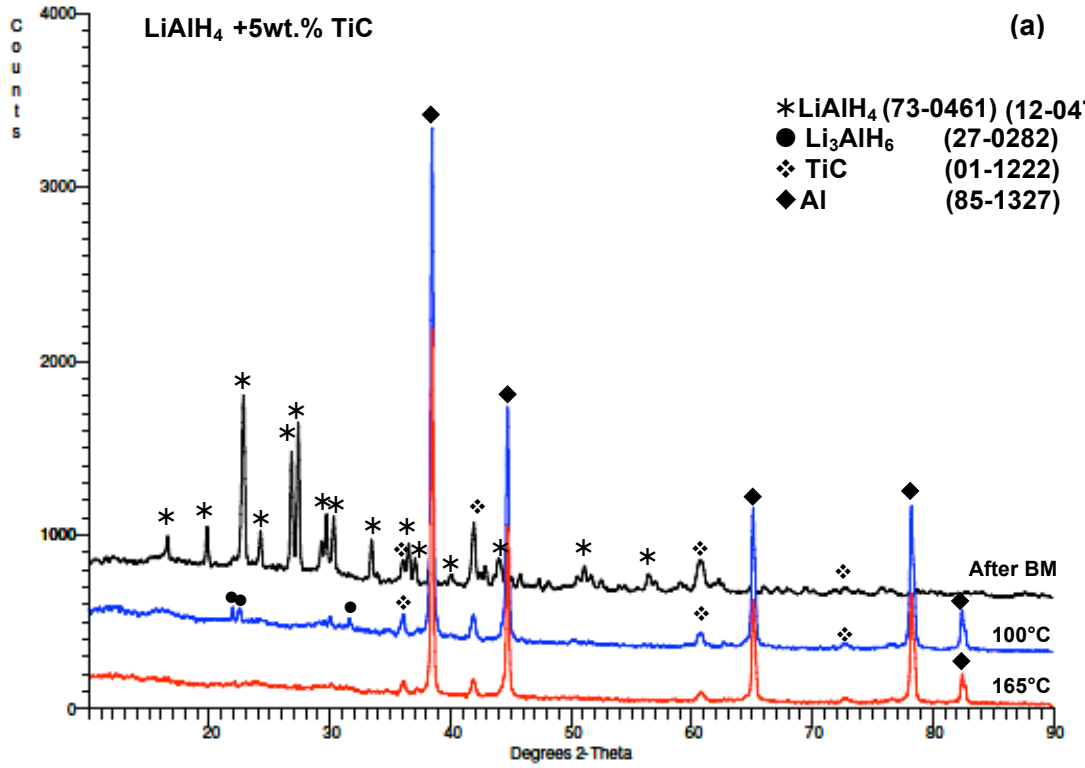
LiAlH4 +5wt.% TiC
(a)
∗LiAlH4 (73-0461) (12-0473)
● Li3AlH6 (27-0282)
❖ TiC (01-1222)
◆ Al (85-1327)
After BM
100°C
165°C
Counts
Degrees 2-Theta

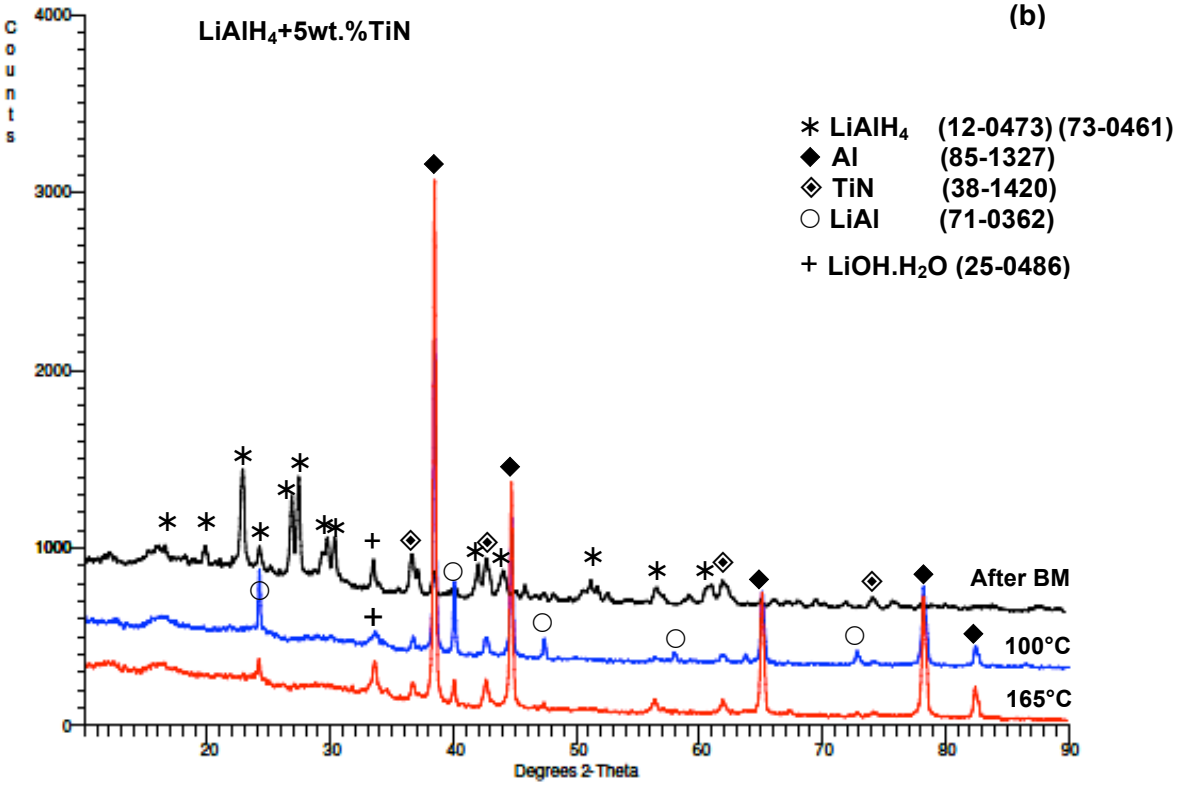
LiAlH4+5wt.%TiN
(b)
∗ LiAlH4 (12-0473) (73-0461)
◆ Al (85-1327)
◈ TiN (38-1420)
○ LiAl (71-0362)
+ LiOH.H2O (25-0486)
After BM
100°C
165°C
Counts
Degrees 2-Theta

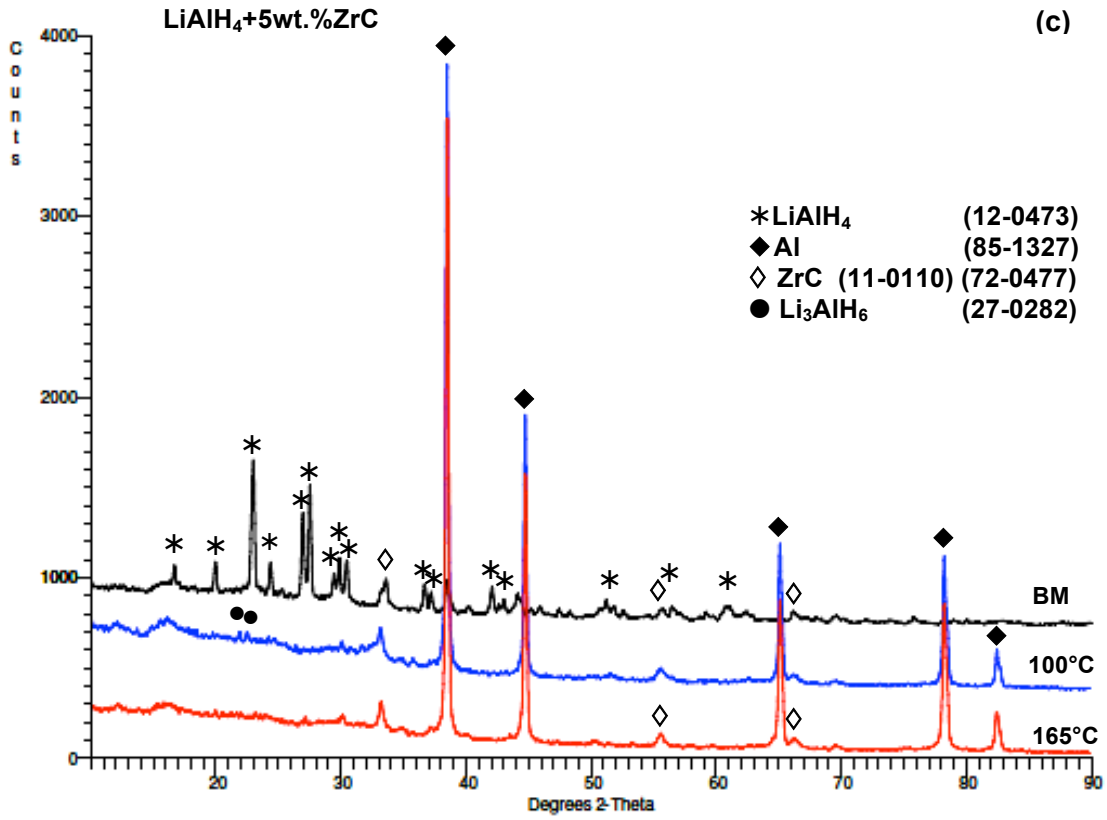

Fig.7.18 XRD patterns after dehydrogenation at varying temperatures corresponding to Fig. 12.17a-c. ICDD file numbers are shown for peak identification a) n-TiN b) n-TiC c) n-ZrC. Ball milled under IMP68-4B R132 15min (Q_{TR}=18.2 kJ/g).

The apparent activation energies of Stage I and II were calculated from the slopes of dehydrogenation curves (such as those in Fig. 7.17 a-c). An example of the Arrhenius-type plots of the rate constant k in Eq. (7.2) vs. temperature for ball milled ($LiAlH_4$+5 wt.% n-TiC) is shown in Fig. 7.19 a-b for dehydrogenation in Stage I and II. The high value of R^2 (0.99) confirms the excellent experimental fit to Eq.(3.2). The calculated apparent activation energies of all composites are listed in Table 7.3.

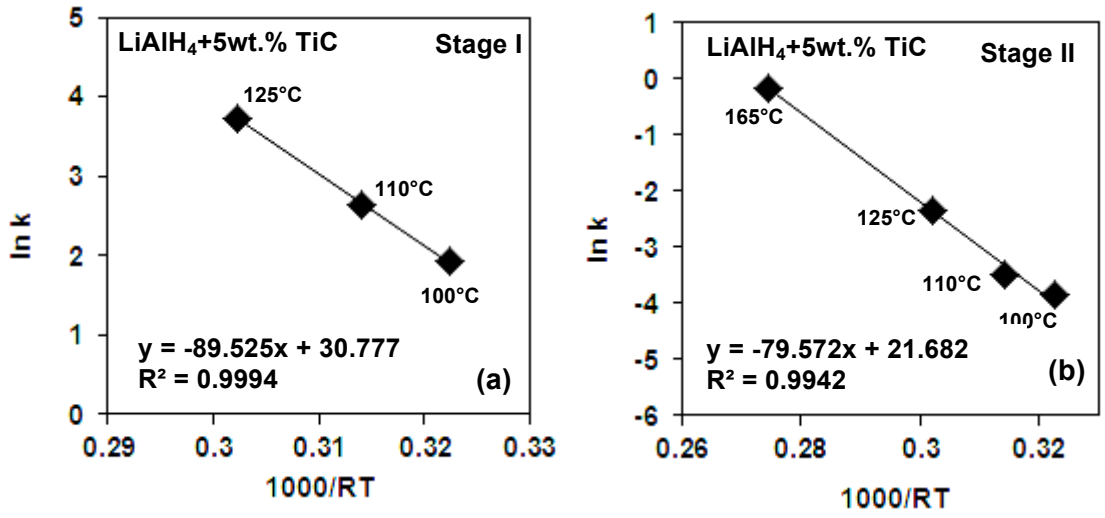

Fig.7.19 The Arrhenius plots of the rate constant k in Eq. (7.2) vs. temperature for estimation of the apparent activation energy of hydrogen desorption for ($LiAlH_4$+5wt.% n-TiC) (a) Stage I (b) Stage II desorption. Ball milled under IMP68-4B R132 15min (Q_{TR}=18.2 kJ/g) .

Table 7.3 Apparent activation energies of dehydrogenation for LiAlH4 with the n-TiC and n-TiN and n-ZrC in compare with n-Fe and n-Ni additives.

System	Apparent activation energy (kJ/mol)	
	I	II
Pure LiAlH4 [8]	92.6	92
$LiAlH_4$+5wt.%n-Ni [6]	58.2	96.62
$LiAlH_4$+5 wt.%n-Fe [4]	67.4	76.6±3.2
$LiAlH_4$+5 wt.%n-TiC	89.5±1.2	79.6±1.9
$LiAlH_4$+5 wt.% n-TiN	87.7±0.9	76.6±1.3
$LiAlH_4$+5 wt.% n-ZrC	96.4±3.5	63.4±5.1

This table shows that the apparent activation energies of decomposition reactions of $LiAlH_4$ with 5 wt.% of n-TiC, n-TiN and n-ZrC compared with nanometric Ni and Fe (which were ball milled under the same milling energy (Q_{TR}=18.2 kJ/g)). It is clear

that the average apparent activation energy for Stage I is in the range of 87-96kJ/mol and n-TiN and n-TiC result in lower apparent activation energies than n-ZrC. These results are in a full accord with the mechanical desorption rate shown in Fig.7.3. Rafe et al. [146], however, have reported better desorption/ absorption for n-TiC compared to n-TiN. The n-Fe/Ni additives show drastically smaller activation energy on the order of 58-67 kJ/mol for Stage I dehydrogenation. The average apparent activation energy for Stage II seems to fall within the range of 63-80 kJ/mol for the nanocomposites with interstitial compounds in the order of ZrC<TiN<TiC, while the n-Fe/Ni show much higher values (100-104 kJ/mol). Table 12.3 illustrates that n-TiC, n-TiN and n-ZrC additives are able to strongly reduce the apparent activation energy of Stage II dehydrogenation (reaction (1-13)), but they do not meaningfully affect the Stage I (reaction (1-12)). However metallic additives, such as n-Fe and n-Ni, do significantly reduce the apparent activation energy of Stage I but have no effect on Stage II (as we can see in section 7.1). The values of activation energies for the n-TiC additive achieved in this work are different, particularly in Stage I, from what was reported by Rafi-ud-din et al. and Li et al. [10,11]; this may be accounted for by having originated from different methods of calculation and different amount of additive.

Fig.7.20 illustrates a comparison of the effect of 5 wt. % of interstitial compounds (n-TiC, n-TiN and n-ZrC) with metallic additives (n-Ni and n-Fe) on the dehydrogenation behavior at 100 °C, which is the maximum temperature for a PEM fuel cell stack. It should be pointed out that the sample with n-Fe released almost 0.7 wt.% H_2 during

15min ball milling, while the remaining counterparts did not desorb hydrogen at the same milling condition.

At such a low temperature, then, the dehydrogenation curves for the nanocomposites containing interstitial additives show slightly lower rate of H_2 dehydrogenation in Stage I than their counterpart with metallic additives. It was shown that both the Fe and Ni ions are able to dissolve in the lattice of $LiAlH_4$, replacing Al and forming a "substitutional solid solution" of either $LiAl_{1-x}Fe_xH_4$ or $LiAl_{1-x}Ni_xH_4$ type, which leads to a various degree of volumetric lattice expansion of $LiAlH_4$ and its destabilization. Table 7.4 shows the results of lattice expansion of $LiAlH_4$ with 5 wt.%, n-TiC, n-TiN and n-ZrC milled with different energy. There are no evident changes in unit cell volume of $LiAlH_4$ after ball milling, which could be another factor that confirms the stability of interstitial characteristics of these additives. This result is in disagreement with the suggestion of Li et al. [147] about destabilization of $LiAlH_4$ structure by TiN.

It may be argued that the metallic additives can improve desorption rate in two ways: (1) destabilization of the $LiAlH_4$ lattice and (2) the catalytic effect while the interstitial compounds exert only a catalytic effect in reactions. Lattice destabilization shows its effect on the first step of desorption, right after ball milling. The addition of n-Fe and n-Ni results in the lower activation energy in Stage I (compared to the interstitial compounds.

Table7.4 The lattice parameters and unit cell volume for LiAlH4 after milling with various milling energies (milling durations) and with the addition of nanometric TiC, TiN and ZrC.

Additive	Milling energy (kJ/g)	Lattice Parameters $LiAlH_4$					
		a(A^o)	b(A^o)	c(A^o)	γ°	$V(A^o)^3$	(ΔV/V) (%)
$LiAlH_4$+5 wt. % n-TiC	0	9.664	7.830	7.913	111.55	556.914	0
	18.2	9.685	7.850	7.915	112.23	557.092	0.0319
	364	9.677	7.868	7.908	112.25	557.348	0.0780
$LiAlH_4$+5 wt.% n-TiN	18.2	9.674	7.841	7.904	111.70	557.166	0.0452
	218.4	9.660	7.845	7.900	111.54	556.936	0.0039
$LiAlH_4$+5 wt. % n-ZrC	18.2	9.667	7.838	7.912	111.70	557.007	0.0167
	218.4	9.660	7.836	7.915	111.57	557.174	0.0466

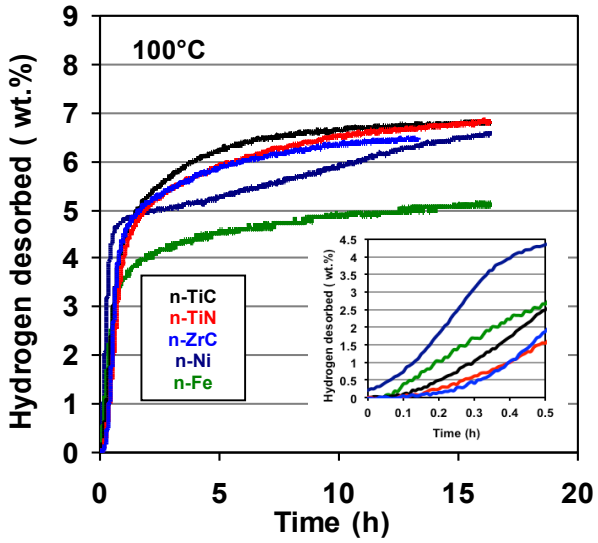

Fig.11.20 A comparison of volumetric dehydrogenation curves at 100°C for LiAlH4 containing 5 wt.% nanometric size TiC, TiN, ZrC and the counterparts containing 5 wt.% n-Ni and n-Fe additive reported in [4,6]. Ball milled under IMP68-4B-R132 15min (Q_{TR}=18.2 kJ/g).

Ball milled ($LiAlH_4$+5 wt.% n-TiC/TiN/ZrC) are able to self-discharge a significant amount of H_2 during storage at room temperature (RT) and 40°C (as shown in

Fig.7.21 a and b). The ball milled nanocomposite powders were stored in Ar filled and sealed glass vials in a glove box (RT) and oven (40°C). Small samples were extracted from the vial after a predetermined time of storage and the amount of H_2 desorbed was measured from a dehydrogenation curves at 200°C (as shown in Fig.7.21 a and b).

It is interesting that all nanometric catalysts n-TiC, n-TiN and n-ZrC produce nearly identical quantities of slowly discharged H_2. The amount of discharged hydrogen are minimal at room temperature (Fig.7.21.a) after 15 days (~1 wt.%) in comparison to the data for n-Ni and n-Fe (~4 wt.%). When the storage temperature increases to 40°C (Fig.7.21b), the quantity of H_2 discharged from ball milled $LiAlH_4$ with interstitial additives reaches about 5-6 wt.% after 15 days, and this is comparable with $LiAlH_4$+5 wt.% n-Ni/n-Fe (5 wt.%).

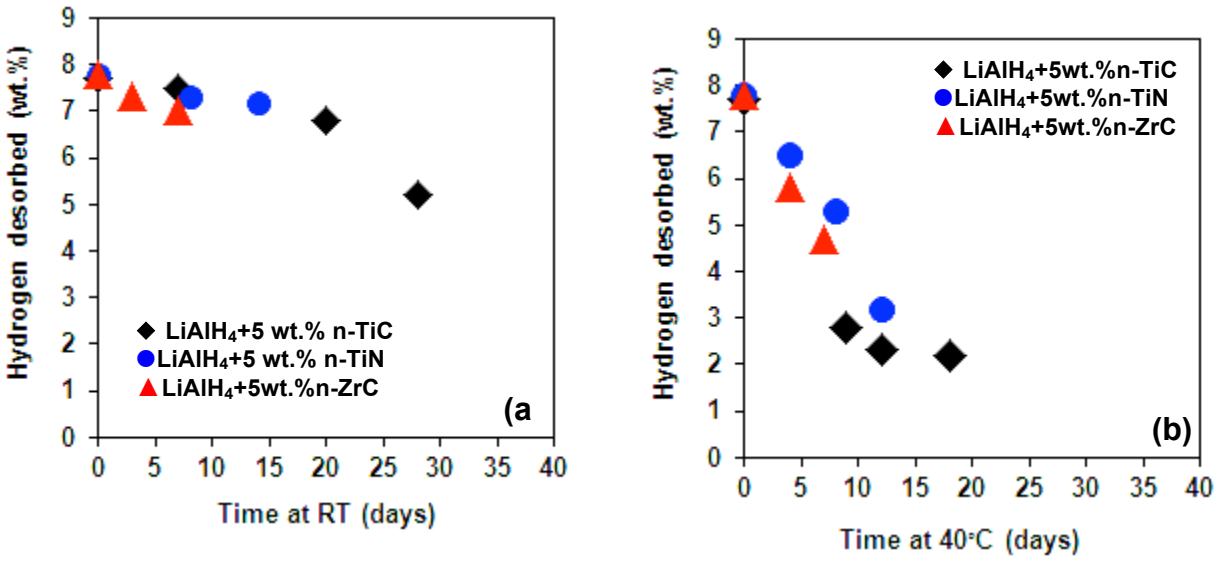

Fig.7.21 Plots of hydrogen desorbed vs. storage time in days for ball milled $LiAlH_4$ containing 5 wt.% nanosized TiC, TiN and ZrC (a) Stored at room temperature (RT) under Ar, then desorbed at 165°C. (b) Stored at 40°C under Ar, then desorbed at 165°C. All dehydrogenations carried out at 1 bar H_2 pressure. Ball milled under IMP68-4B-R132 15min (Q_{TR}=18.2 kJ/g).

Given the presented results, it does appear that $LiAlH_4$ could be used as a near-commercial solid state H_2 storage material in a number of applications other than automotive. With both metallic and interstitial compounds additives, it can slowly self-discharge large quantities of H_2 during long-term storage under the influence of argon. This phenomenon has two aspects worthy of attention. One is purely scientific and requires that the properties of $LiAlH_4$ with these additives be investigated immediately after completion of ball milling (because a longer storage may lead to erroneous results as the compound would be partially desorbed). The other is the practical significance of such a behaviour for long-duration, low-demand devices that use H_2 (such as low-power remote fuel cells or portable gas analyzers). These composites can also be used in a number of chemical processes where a continuously reducing atmosphere is needed.

7.2.3. Rehydrogenation

To study the possibility of rehydrogenation in the first step, the samples were fully dehydrogenated at 165°C at 1 bar H_2 pressure. Fig.7.22a illustrates the rehydrogenation (at 165°C under 95bar of H_2) and subsequent dehydrogenation (at 165°C) curves of $LiAlH_4$ doped with 5 wt.% n-TiC.

It is noticeable that, after each dehydrogenation step, the amount of desorbed H_2 is equal to 0.17 wt.% (which is almost in the range of the Sieverts apparatus error). The XRD pattern after rehydrogenation in Fig.7.22 b clearly shows the lack of diffraction peaks of Li_3AlH_6. The results of rehydrogenation of the LiAlH4 doped with 5 wt.% n-TiN and n-ZrC show almost the same results (0.13 and 0.15 wt.% H_2). Rafi-ud-din et al. [65] and Li et al. [146] demonstrated that by increasing the amount of n-TiC and n-

TiN in the mixture, the amount of hydrogen desorption and absorption was improved. The discrepancies between the results can be traced to the significant difference between the amounts of additives used in both works as well. Successful rehydrogenation parameters seem to depend on the type of catalytic additive/precursor used and they vary from one to another. It is possible that the rehydrogenation conditions of temperature/pressure/time for metallic additive are still different than those for nanometric interstitial compounds.

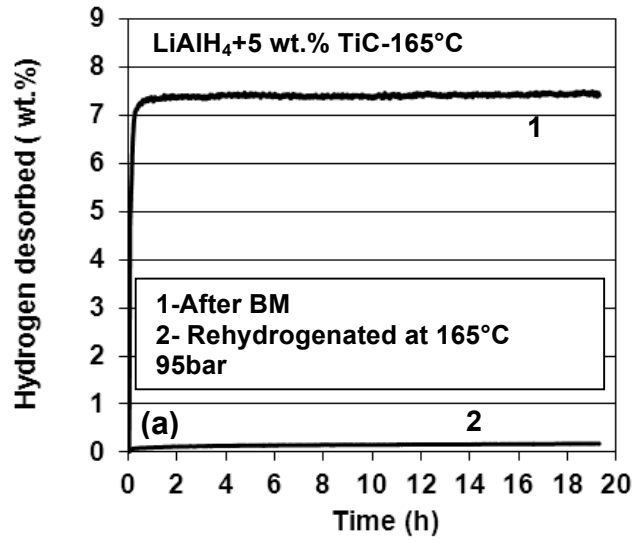

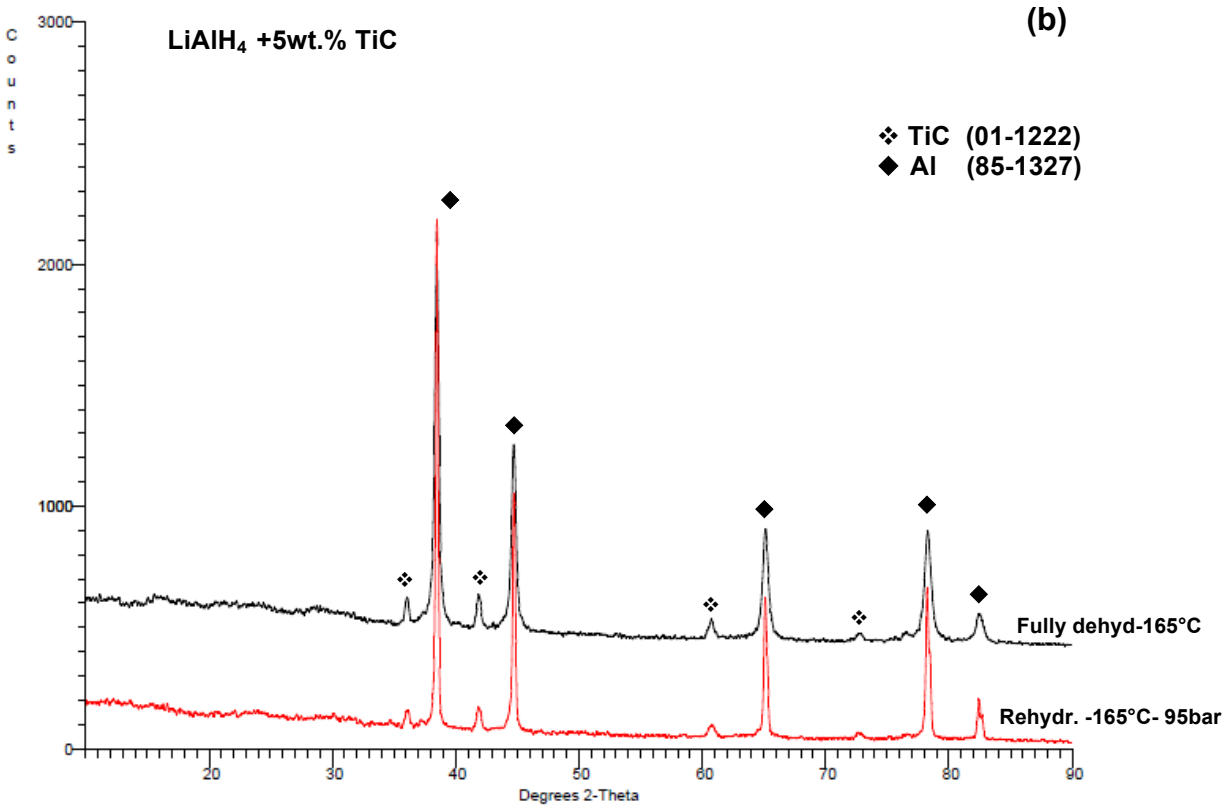

Fig.7-22 a)Volumetric dehydrogenation/rehydrogenation curves for $LiAlH_4$ containing 5 wt.% n-TiC b) Corresponding XRD patterns after first dehydrogenation and second dehydrogenation after rehydrogenation. ICDD file numbers are shown for peak identification. Ball milled under IMP68-4B-R132 15min (Q_{TR}=18.2 kJ/g).

7.2.5. Conclusions

These results explain the influence of the addition of 5 wt.% nanosized "interstitial compound" (n-TiC, n-TiN and n-ZrC) on the stability and dehydrogenation properties of lithium alanate. The main conclusions can be summarized as follows:

1. The mechanical dehydrogenation occurs during high energy ball milling of the $LiAlH_4$ nanocomposites. A continuous desorption of H_2 is observed reaching 4 wt.% H_2 after 25 h of milling (Q_{TR}=1820 kJ/g). In contrast there is no H_2 desorption during low energy ball milling of $LiAlH_4$ (Q_{TR}=18.2 kJ/g).

2. XRD shows that during high energy ball milling of nanocomposites there occurs a gradual decomposition of $LiAlH_4$ to Li_3AlH_6 and Al.

3. Mechanical dehydrogenation rate of the systems with interstitial compounds additives, increases noticeably in the order of TiN > TiC > ZrC.

4. For Stage I, the interstitial additives result in the average apparent activation energy within the range of 87-96 kJ/mol, whereas the nanometal additives (n-Fe, n-Ni) show drastically smaller the average apparent activation energy on the order of 58-67 kJ/mol most likely due to observed lattice expansion.

5. For the interstitial compounds additives the average apparent activation energy for Stage I is within the range of 87-96kJ/mol in the order of TiN < TiC < ZrC, which is much lower than that for the nanometal additives. These results are in a full accord with the mechanical dehydrogenation rate.

6. For Stage II dehydrogenation, the average apparent activation energy is within the range of 63-80 kJ/mol for interstitial additives, while metallic dopants (n-Fe, n-Ni) do not show significant effect on this stage (76-97 kJ/mol).

7. Ball milled $LiAlH_4$ with 5 wt.% n-TiC, n-TiN and n-ZrC is able to slowly self-discharge large quantities of H_2 up to 3 and 5-6 wt.% during storage at room temperature and 40ºC, respectively.

8. The results of the rehydrogenation at 165 ºC under 95 bar for 5 h indicate that $LiAlH_4$ doped with interstitial compounds show only about 0.3 wt.% rehydrogenated hydrogen quantity.

8. Summary and recommendations

The fundamental understanding of the des/absorption behavior of selected complex hydrides and their composite systems was investigated in this work.

Unfortunately, no breakthrough has been made that would identify a complex hydride system as a storage medium for automotive. None of these hydrides can be considered a potential candidate because they have lower practical gravimetric capacities than the targeted ~10 wt% H_2 for a storage material (5.5 wt% H_2 for a storage system) regarding the DOE targets for automotive.

However the catalyzed lithium alanat ($LiAlH_4$) with nanometric metal and interstitial compounds additives (5-6 wt% H_2 within 5 h at 100ºC) may be close near-commercialization for applications in disposable H_2 storage cartridges for long-duration, low-demand devices that use H_2. Most interestingly, its ability for a slow self-discharge at RT, 40, and 80 ºC makes it an attractive candidate for usage in commercial disposable cartridges. Obviously, insufficient H_2 discharge capacity at 100ºC and irreversibility at reasonable combination of temperature and pressure are severe drawbacks for on-road automotive applications of $LiAlH_4$. However, it can be imagined that by using larger disposable cartridges with catalyzed $LiAlH_4$, it would be feasible to power fuel cells in the off-road vehicles that do not require a substantial driving range and/or on-board reversibility.

In the group of lithium amides, the catalyzed ($LiNH_2$+$nMgH_2$) system with KH is able to dehydrogenate about 1 wt% H_2 at 125ºC in 5h , which is rather inadequate quantity for any practical application at that temperature. However, it can be fully rehydrogenated at 200ºC and 50 bar pressure. This system is still unable to desorb

larger quantities of H_2 at low temperatures. This is either a thermodynamic constraint indicating that a further reduction of the reaction enthalpy change is needed or a kinetic constraint indicating that more effective catalysts must be sought for improving the hydrogen storage properties of this particular system.

References

[1] E. David, , Journal of Materials Processing Technology 162 (2005) 169–177.

[2] Intergovernmental Panel on Climate Change. “Climate Change 2007: Synthesis Report”, Geneva,Switzerland. IPCC (2007).

[3] L. Schlapbach, A. Züttel, Nature 414 (2001) 353-358.

[4] R. Westerwaal, W. Haije, Evaluation, Energieonderzoek Centrum Nederland publisher (ECN), E043 (April 2008).

[5] B. Sakintuna, F. Darkrim, M. Hirscher, International Journal of Hydrogen Energy 32 (2007) 1121-1140.

[6] R.A. Varin, T. Czujko, Z. Wronski, Springer, 233 Spring Street, New York, NY 10013, USA, 2009 .

[7] L. Zhou, Renewable and Sustainable Energy Reviews 9 (2005) 395-408.

[8] J. Gross, K. Russell Carrington, Steven Barcelo, Recommended Best Practices for the Characterization of Storage Properties of Hydrogen Storage Materials, 3 34 (2012) 1-570

[9] C. S. Wang, H. Wang, Q. Lei, P. Chen, Q. D. Wang, Int. J. Hydrogen Energy 21 (1996) 471-478.

[10] M. Martin, G. Gommel, C. Borkhardt, E. Fromm, J. Alloys Comps. 238 (1996) 193-201.

[11] R. Schulz, J. Huot, G. Liang, S. Boily , G. Lalande, Mater Sci Eng A (1999) 267-240.

[12] J. J. Vajo, G. L. Olsen, Scripta Materialia 56 (2007) 829-834.

[13] L. Shaw, R. Ren, J. Hu, J. Kwak, Z. Yang, JOM Vol 61 4, April (2009) 45- 57.

[14] L. Zaluski, A. Zaluska, J. Stom-Olsen, J Alloys Compds 253-254 (1997) 70-79 .

[15] R. Baer, Y. Zeiri, R. Kosloff, Phys. Rev. B 55 16 (1997) 952–74.

[16] R. Holtz, M. Imam, J Mater Sci 34 (1999) 55–63.

[17] C. Jensen, D. Sun, S. Raman, K. Murphy, NREL/CP-610-32405 (2002).

[18] Anton, D.L., *J. Alloys and Compounds*, 400 (2003) 356-357.

[19] S. H. Joo, S. J. Choi, I. Oh, et al., Nature 412 (2001) 169–172

[20] M. U. Niemann, S. S. Srinivasan, A. R. Phani, A. Kumar, D. Y. Goswami, E. K. Stefanakos, J. Nanomaterials, Review article (2008) 1-9

[21] K. Franc, A. Zinsou, Energy & Environmental Science, 3 5 (2010) 497-676.

[22] F. Pinkerton, G. Meisner, M. Meyer, M. Balogh, M. Kundrat, J. Phys. Chem. B 109 (2005) 6-8.

[23] Y. Nakamori, S. Orimo, J. Alloys Compd. 370 (2004) 271-275.

[24-18] J. Vajo, F. Mertens, Phys. Chem. B 108 (2004) 13977-13983.

[25] V. Alapati, J. Karl Johnson, S. Shol, J. Phys. Chem. C 111 (2007) 1584-1591.

[26] J. Vajo, L. Skeitha, F. Mertensb, S. Jorgensen, Journal of Alloys and Compounds 390 (2005) 55–61.

[27] H. Gleiter. Z. Metallkd. 86 (1995) 78-83

[28] W. Osborn, T. Markmaitree, L. Shaw, R. Ren, Journal of Alloys and Compounds 448 (2008) 263–271.

[29] S. Dillich, Hydrogen Storage, 2009 DOE Hydrogen Program & Vehicle Technologies Program, 19 May 2009.

[30] A. Andreasen, T. Veggea, A. Pedersen, Journal of Solid State Chemistry 178 (2005) 3672–3678.

[31] Wolf, D., Philosophical Magazine, B, 59 6 (1989) 667-680.

[32] V.Berube, G. Radtke, Dresselhaus, M., Chen, G., Int. J. Energy Res., 31 (2007) 637-663.

[33] A. Zaluska, L. Zaluski, J.O. Stro¨m-Olsen, Journal of Alloys and Compounds 298 (2000) 125–134.

[34] R. Walters, J. Scogin, Journal of Alloys and Compounds 421 (2006) 54–56.

[35] A. Zu¨ttel, S. Rentsch, P.Fischer, J Alloys Compd 356-357 (2003) 515-520.

[36] S.Orimo, Y.Nakamori, G.Kitahara, J Alloys Compd 404 (2005) 427-430.

[37] H. Li, Y. Yan, S. Orimo, A. Zu¨ttel, Energies 4 (2011)185-214.

[38] H. Schlesinger, H. Brown, J Am Chem Soc, 62 (1940) 3429-3435.

[39] Xia GL, Guo YH, Wu Z, Yu XB., J Alloys Compd 479 (2009) 545-548.

[40] M.Wellons, P. Berset, R. Zidan, Nanotechnology 20 (2009) 204-212.

[41] B. Zhang, B. Liu, Int J Hydrogen Energy 35 (2010) 7288-7294.

[42] R. Varin, R. Parviz,international journal of hydrogen energy 37 (2012)1584-1593.

[43] A. Züttel, A. Borgschulte, S. Orimo, materials Scr. Mater 56 (2007) 823-830.

[44] A. Finholt, A. Bond, H. Schlesinger, Journal of the American Chemical Society 69 (1947) 1199 – 1203.

[45] O. M.Løvvik, S. Opalka, H. Brinks, Physical Review B 69 (2004) 117-134.

[46] http://en.wikipedia.org/wiki/Lithium aluminium hydride

[47] A. Andreasen, Journal of Alloys and Compounds 419 (2006) 40–44.

[48] W. Osborn, T. Markmaitree, JOM 61 4 (2009) 45- 53.

[49] J. Chen, N. Kuriyama, Q. Xu, H. Takeshita, T. Sakai, J. Phys. Chem. B 105 (2001) 11214-11220.

[50] J. Wook, J. Shimb, Y. Chob, B. Lee, Journal of Alloys and Compounds, 420 (2006) 286 –290.

[51] Y. Kojima, Y. Kawai, T. Hagab, M. Matsumoto, A. Koiwai, Journal of Alloys and Compounds 441 (2007) 189–191.

[52] H. Brinks, A. Fossdal, Journal of Alloys and Compounds 397 (2005) 291–295.

[53] J.J. Reilly, Scripta Materialia 56 (2007) 835-839.

[54] J.R. Ares, K-F. Aguey-Zinsou, M. Porcu, J.M. Sykes, M. Dornheim, T. Klassen, R. Bormann. Mater Res Bulletin 43 (2008) 1263-1275.

[55] S. Orimo, Y. Nakamori, J. R. Eliseo, A. Züttel, C.M. Jensen, Chem Rev 107 (2007) 4111-4132.

[56] J. Block, A.P. Gray, Inorg Chem 4 (1965) 304-305.

[57] F. Mulana, N. Nishimiya, J Alloys Compd 413 (2006) 273-280

[58] X. Ke X, C. Chen, Phys Rev B 76 (2007) 112-117.

[59] J.W. Jang, J.H. Shim, YW Cho, B.J. Lee, J Alloys Compd 420 (2006) 286-290.

[60] J.R. Ares Fernandez, K.F. Aguey-Zinsou, M. Elsaesser, X.Z. Ma, M. Dornheim, T. Klassen, R. Bormann, Int J Hydrogen Energy 32 (2007) 1033-1040.

[61] S.S. Liu, L.X. Sun, Y. Zhang, F. Xu, J. Zhang, H.L. Chu, M.Q. Fan, T. Zhang, X.Y. Song, J.P. Grolier, Int J Hydrogen Energy 34 (2009) 8079-8085.

[62] M. Ismail, Y. Zhao, X.B. Yu, S.X. Dou, Int J Hydrogen Energy 35 (2010) 2361-2367.

[63] J. Wang, D. Ebner, J. Ritter, J. Am. Chem. Soc. 128 (2006) 5949-5954.

[64] X. Liu, G. McGrady, W. Langmi, AM. CHEM. SOC. 131 (2009) 5032–5033

[65] Rafi-ud-din, Z. Lin, P. Li, X. Qu, J Alloys Compd 508 (2010) 119-128

[66] X.F. Liu, H.W. Langmi, S.D. Beattie, F.F. Azenwi, G. Sean McGrady, C.M. Jensen, J Am Chem Soc 133 (2011) 15593-15597.

[67] F.F. Azenwi, H.W. Langmi, G. Sean McGrady, J Alloys Compd 3 (2012) 160-165.

[68] V.P. Kojima, J.W. Wiench, K.W. Dennis, M. Pruski, V.K. Pecharsky, J Alloys Compd 329 (2001)108-114.

[69] V.P. Balema, V.K. Pecharsky, K.W. Dennis, J Alloys Compd 313 (2000) 69-74.

[70] T. Sun, C.K. Huang, H. Wang, L.X. Sun, M. Zhu, Int J Hydrogen Energy 33 (2008) 6216-6221.

[71] M. Resan, M.D. Hampton, J.K. Lomness, D.K. Slattery, Int J Hydrogen Energy 30 (2005)1413-1416.

[72] Y. Kojima, Y. Kawai, M. Masumoto, T. Haga, J Alloys Compd 462 (2008) 275-278.

[73] X. Zheng, P. Li, F. An, G. Wang, X. Qu, Rare Met Mater &Eng 37 (2008) 400-403.

[74] R.A. Varin, L. Zbroniec, J Alloys Compd 504 (2010) 89-101.

[75] R.A. Varin, L. Zbroniec, J Alloys Compd 506 (2010) 928-939.

[76] R.A. Varin, L. Zbroniec, T. Czujko, Z.S. Wronski, Int J Hydrogen Energy 36 (2011) 1167-1176.

[77] R.A. Varin, R. Parviz, Int J Hydrogen Energy 37 (2012) 9088-9102.

[78] P. Chen, Z. Xiong, J. Luo, J. Lin, K.L. Tan, Nature 420 (2002) 302.

[79] J. Hu, G. Wu, Y. Liu, J Phys Chem B 110 (2006)14688-14692.

[80] Y. H. Hu, E. Ruckenstein, Ind. Eng. Chem. Res. 42 (2003) 5135–5139

[81] T. Ichikawa, N. Hanada, S. Isobe, H. Leng, H. Fujii, J. Phys. Chem. B 108 (2004) 7887–7892

[82] S. Orimo, Y. Nakamori, G. Kitahara, K. Miwa, N. Ohba, T. Noritake, S. Towata, Appl. Phys. A 79 (2004) 1765–1767

[83] T. Ichikawa, N. Hanada, S. Isobe, H. Leng, H. Fujii, Mater. Trans. 46 (2005) 1–14

[84] H. Y. Leng, T. Ichikawa, S. Isobe, S. Hino, N. Hanada, H. Fujii, J. Alloys Compd. 404– 406 (2005) 443–447

[85] G. P. Meisner, F. E. Pinkerton, M. S. Meyer, M. P. Balogh, M. D. Kundrat, J. Alloys Compd. 404–406 (2005) 24–26

[86] S. Isobe, T. Ichikawa, N. Hanada, H. Y. Leng, M. Fichtner, O. Fuhr, H. Fujii, J. Alloys Compd. 404–406 (2005) 439–442

[87] Y. Kojima, Y. Kawai, Chem. Commun., 19 (2004), 2210-2211

[88] T. Ichikawa, S. Isobe, N. Hanada, H. Fujii, J. Alloys Compd. 365 (2004) 271-276

[89] J. H. Yao, C. Shang, K.F. Aguey-Zinsou, Z.X. Guo, J. Alloys Compd. 432 (2007) 277- 282

[90] J. Lu, Z.Z. Fang, H.Y. Sohn, Inorg. Chem. 45 (2006) 8749-8754

[91] W. I. F. David, M. O. Jones, D. H. Gregory, C. M. Jewell, S. R. Johnson, A. Walton, P. P. Edward, J. Am. Chem. Soc., 129 (2007) 1594-1601

[92] H. Y. Leng, T. Ichikawa, S. Hino, N. Hanada, S. Isobe, H. Fujii, J. Phys. Chem. B 108 (2004) 8763–8765.

[93] Y. Nakamori, G. Kitahara, S. Orimo, J. Power Sources 138 (2004) 309–312

[94] Z. Xiong, G. Wu, J. Hu, P. Chen, Adv. Mater. 16 (2004) 1522–1525

[95] Z. Xiong, J. Hu, G. Wu, P. Chen, W. Luo, K. Gross, J. Wang, J. Alloys Compd. 398 (2005) 235–239

[96] Z. Xiong, G. Wu, J. Hu, P. Chen, W. Luo, J. Wang, J. Alloys Compd. 417 (2006) 190-194

[97] W. Luo, J Alloys Compd 385 (2004) 316-320.

[98] L. Xie, J. Zheng, Y. Liu, Y. Li, X. Li, Chem. Mater. 20 (2008) 282-286.

[99] Y. Nakamori, G. Kitahara, K. Miwa, S. Towata, S. Orimo, Appl. Phys. A 80 (2005) 1–3

[100] W. Luo, E. Rönnebro, J Alloys Compd 404-406 (2005) 392-395.

[101] W. Luo, S. Sickafoose, J Alloys Compd 407 (2006) 274-281.

[102] T. Ichikawa, H.Y. Leng, S. Isobe, N. Hanada, H. Fujii, J Power Sources 159 (2006) 126-131.

[103] Y. Chen, P. Wang, C. Liu, H-M. Cheng, Int J Hydrogen Energy 32 (2007) 1262-1268.

[104] J. Lu, Z.Z. Fang, Y.J. Choi, H.Y. Sohn, J Phys Chem C 111 (2007) 12129-12134.

[105] R.R. Shahi, T.P. Yadav, M.A. Shaz, O.N. Srivastava, Int J Hydrogen Energy 33 (2008) 6188-6194.

[106] C. Liang, Y. Liu, K. Luo, B. Li, M. Gao, H. Pan, Q. Wang, Chem Eur J 16 (2010) 693-702.

[107] O. Dolotko, N. Paulson, V.K. Pecharsky, Int J Hydrogen Energy 35 (2010) 4562-4568.

[108] D. Pottmaier, F. Dolci, M. Orlova, G. Vaughan, M. Fichtner, W. Lohstroh, M. Baricco, J Alloys Compd 509 (2011) 719-723.

[109] C. Price, J. Gray, R. Lascola Jr., D. L. Anton, 37 (2012) 2742-2749.

[110] T. Durojaiye, A. Goudy, Int J Hydrogen Energy 37 (2012) 3298-3304.

[111] W. Luo, V. Stavila, L.E. Klebanoff, Int J Hydrogen Energy 37 (2012) 6646-6652.

[112] Y. Chen, C. Z. Wu, P. Wang, H. M. Cheng, Int. J. Hydrogen Energy 31 (2006) 1236– 1240

[113] H. Y. Leng, T. Ichikawa, H. Fujii, J. Phys. Chem. B 110 (2006) 12964–12968

[114] S.V. Alapati, J. K. Johnson, D.S. Sholl, Chem Phys 9 (2007) 1438–1452.

[115] A. R. Akbarzadeh, V. Ozolins, C. Wolverton, Adv. Mater. 19 (2007) 3233 – 3239.

[116] W. Osborn, T. Markmaitree, L. L. Shaw, J. Power Sources 172 (2007) 376 – 378.

[117] Y. Liu, K. Zhong, M. Gao, J. Wang, H. Pan, Q. Wang, Chem. Mater. 20 (2008) 3521– 3527

[118] V. Drozd, S. Saxena, V. Garimella, A. Durygin, Int J Hydrogen Energy 32 (2007) 370-375

[119] H. P. Klug, L. Alexander, John Wiley & Sons, New York, 1974, pp. 618–708

[120] www.materialsdata.com.

[121] G. Sandrock, K. Gross, G. Thomas, J Alloys Compd 330-332 (2002) 696-701.

[122] Basu B, Vleugels J, Kalin M., Mat Sci Eng A 2003; 359: 228-236.

[123] B. Prakash, S. Bandyopadhyay, J Am Ceram Soc 82 8 (1999) 2255–2256.

[124] Y. He, A. Winnubst, D. Schipper, Wear 184 (1995) 33-43.

[125] B.Venkata, W. Kima, S. Honga, H. Baeb, Mat Sci Eng A 527 (2010) 474–479.

[126] http://www.matweb.com

[127] D.R. Gaskell, New York, McGraw Hill, 1973.

[128] J. Bloch, J. Alloys Comps. 312 (2000) 135-153

[129] RA. Varin, M. Jang, M. Polanski, J Alloys Compd 491 (2010) 658-667.

[130] W. Lohstroh, M. Fichtner, J Alloys and Compd 446-447(2007) 332-335.

[131] J. Hu, Y. Liu, G. Wu, Z. Xiong, P. Chen, J Phys Chem C 111 (2007) 18439-18443.

[132] J. Hu, Z. Xiong, G. Wu, J Power Sources 159 (2006) 120-125.

[133] L. M, H. Dai, Z. Fang, J Phys Chem 113 (2009) 9944-9949.

[134] RR. Shahi, T. Yadav, M. Shaz, ON. Srivastava, Int J Hydrogen Energy 35 (2010) 238-246.

[135] C. Liang, Y. Liu, Z. Wei, Int J Hydrogen Energy 36 (2011) 2137-2144.

[136] T. Markmaitree, W. Osborn W, Int J Hydrogen Energy 2008; 33: 3915-3924.

[137] E. Klebanoff, W. Luo, V.Stavila, Int. J Hydrogen Energy, 37 8 (2012) 6646-6652

[138] R. Varin, Ch. Chiu, J Alloys Compd 397 (2005) 276-281.

[139] L. Mosegaard , B. Møller , J. Jørgensen, J Alloys Compd 446-447 (2007) 301-305.

[140] J. Soulie, G.Renaudin, J Alloys Compd 346 (2002) 200-205.

[141] www.nanoiron.cz.

[142] X.Xiao, L.Chen, X.Wang, S.Li, C. Chen, Q.Wang, Int J Hydrogen Energy 33 (2008) 64-73

[143] http://webelements.com.

[144] J. Block, A.P. Gray, Inorg Chem 4 (1965) 304-305

[145] J.Wang, A. Ebner, JA. Ritter, Adsorption 2005;11: 811e6.

[146] Rafi-ud-dina,c,, Q.Xuanhuia, L. Pinga, A. Mashkoor, L.Zhang, Rare Metals, 30 (2011) 28-34.

[147] L.Li, F.Qiu, Y. Wang, Y. Xu, C.An, G.Liu, L. Jiao, H.Yuan, int. j of hydrogen energy xxx (2013) 1 -7 (in press).

[148] V. P. Balema, J. W. Wiench, K. W. Dennis, ,J. Alloys Compd. 329 (2001) 108−114.

[149] A. Dunand, H. D. Flack, and K. Yvon, Physical Review B, 31 (1985) 2299-2315.

[150] R.Parviz, R,A.Varin, International Journal of Hydrogen Energy, 38 20 (2013) 8313-8327

Appendices

A.1. Hydrogen storage capacity estimated by pressure variations during milling using a volumetric method

Assuming hydrogen behave as ideal gas, one can estimate the mass of absorbed hydrogen from:

$\Delta P V_{eff} = (m/M_H)RT$ (A-1)

where ΔP is the total pressure change of H_2 in a milling period

V_{eff} is the effective volume of the vial (m^3) (V_{eff} = absolute volume – volume of balls – volume of the material)

m is weight of absorbed H_2 (g)

M_H is molar mass of H_2 (g/mol)

T is the temperature (K)

R is the gas constant (8.314J $(mol)^{-1}K^{-1}$

and **hydrogen capacity (wt.% H_2) = $m/M_p \times 100\%$** (A-2)

where M_p is the initial total powder mass (g) (includes additives)

A-2 Kinetic curves determination by volumetric method in a Sieverts-type Apparatus

The Sieverts-type apparatus consist of: a calibrated volume determined physically, a reactor whose temperature is controlled by the temperature control system and the

cooling system, a vacuum system, a pressure monitoring system, valves and source of hydrogen and argon delivery. The quantity of desorbed hydrogen (number of moles) is calculated using ideal gas low:

$$PV = nRT \quad \text{(A-3)}$$

where P–gas pressure, V–gas volume, n–number of moles of gas, T–absolute temperature of gas, R–the universal gas constant. The value and units of R depend on the units used in determining P, V, n and T

- o The quantity of gas, n, is normally expressed in moles
- o The units chosen for pressure and volume are typically atmospheres (atm) and liters (L), however, other units may be chosen

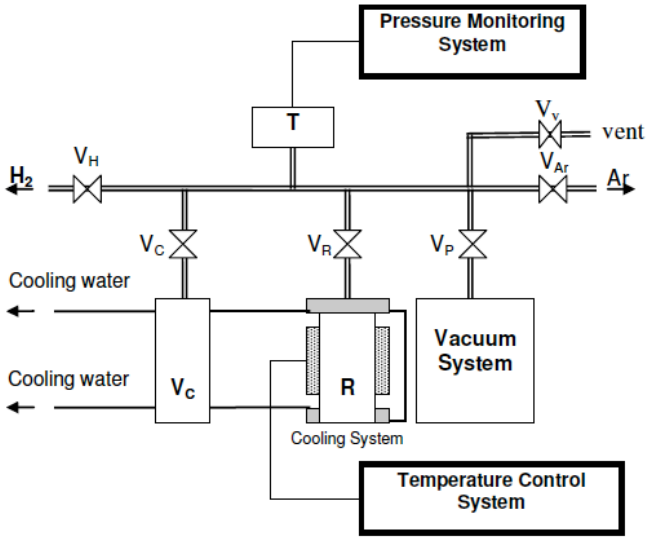

Fig. A.1 Scheme of a Sieverts-type apparatus where: T- transducer, V_H – hydrogen cut off valve, V_{Ar}–argon cut off valve, V_P–vacuum system cut off valve, V_R–reactor cut off valve, V_C–calibrated volume and its cut off valve, V_v-vent valve, R–the reactor.

Therefore, R can be expressed for example in L.atm/mol.K where R=0.08206. Let us assume that we can treat hydrogen as an ideal gas. Before beginning of absorption or desorption the relation between pressure of hydrogen in a system and number of moles of hydrogen at temperature T of the analyzed process can by described by:

$$P_1V=n_1RT \quad \text{(A-4)}$$

After desorption or absorption we have:

$$P_2V=n_2RT \quad \text{(A-5)}$$

where $P_1 > P_2$ for absorption and $P_1 < P_2$ for desorption

Rearranging Eq. A-4 and A-5, we obtain:

$$n_1 = P_1V/RT \qquad n_2 = P_2V/RT \quad \text{(A-6)}$$

Therefore, the difference between number of moles of hydrogen in the system resulting from absorption or desorption is:

$$\Delta n=n_1-n_2 = \Delta PV/RT$$

Where $\Delta P=P_1-P_2$

The mass of absorbed or desorbed hydrogen can be calculated using number of moles of gas and molecular mass of hydrogen: $mH_2 = 2.016\times\Delta n$ which finally gives us:

$$mH_2 = 2.016\ \Delta PV/RT \quad \text{(A-7)}$$

When change in hydrogen mass is known using Eq. A-7, we can easily calculate hydrogen capacity using Eq. A-2.

A-3 Volumetric desorption curves and corresponding XRD and reaction of the system ($LiNH_2$+0.5MgH)+5wt.% additive

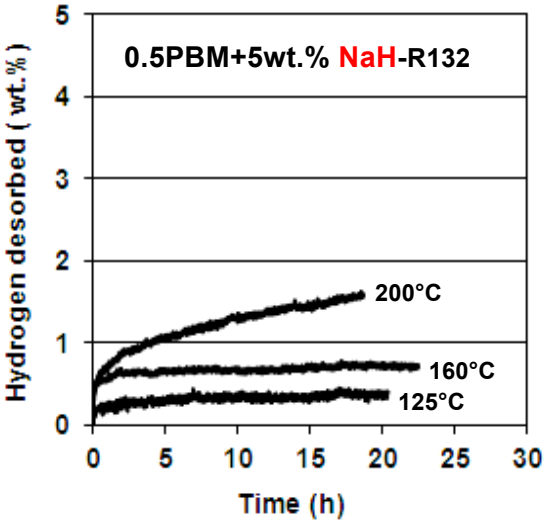
0.5PBM+5wt.% NaH-R132
Hydrogen desorbed (wt.%)
Time (h)
200°C
160°C
125°C
0
1
2
3
4
5
0
5
10
15
20
25
30

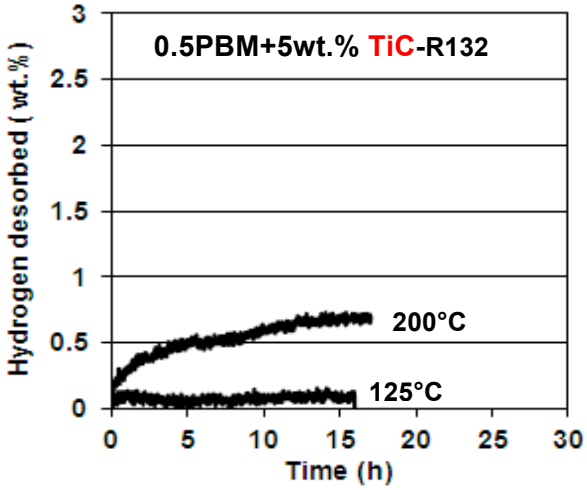
0.5PBM+5wt.% TiC-R132
Hydrogen desorbed (wt.%)
Time (h)
200°C
125°C
0
0.5
1
1.5
2
2.5
3
0
5
10
15
20
25
30

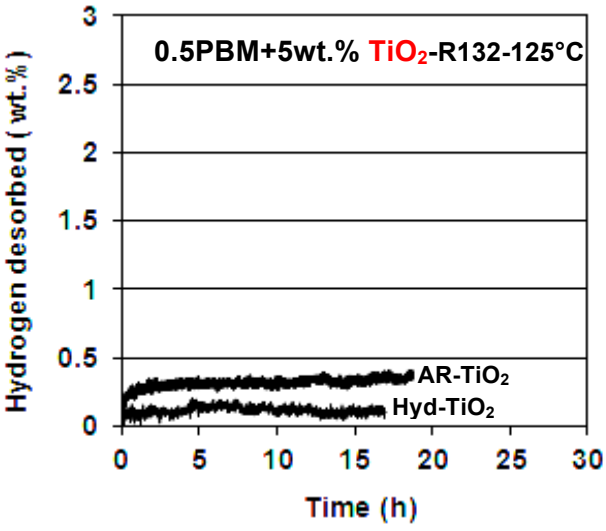
0.5PBM+5wt.% TiO2-R132-125°C
Hydrogen desorbed (wt.%)
Time (h)
AR-TiO2
Hyd-TiO2
0
0.5
1
1.5
2
2.5
3
0
5
10
15
20
25
30

Fig.A.2. volumetric dehydrogenation curves for (PBM(LiNH2+0.5MgH_2)) with 5 wt.% additives at various desorption temperature

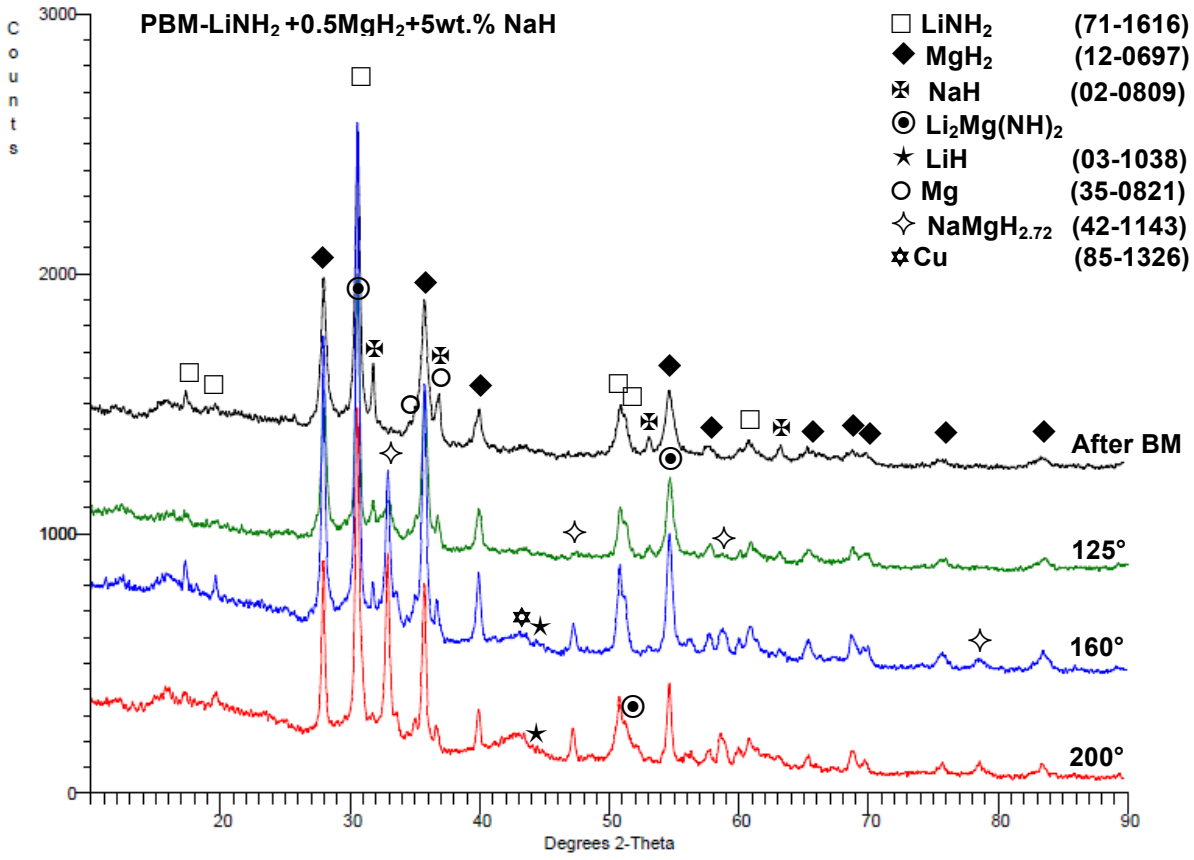

Fig. A.3. The XRD patterns after dehydrogenation at varying temperatures for (PBM($LiNH_2$+0.5MgH_2)+ 5 wt.% NaH) system. ICDD file numbers are shown for peak identification. Ball milled under LES6-4B-R132 15min milling mode.

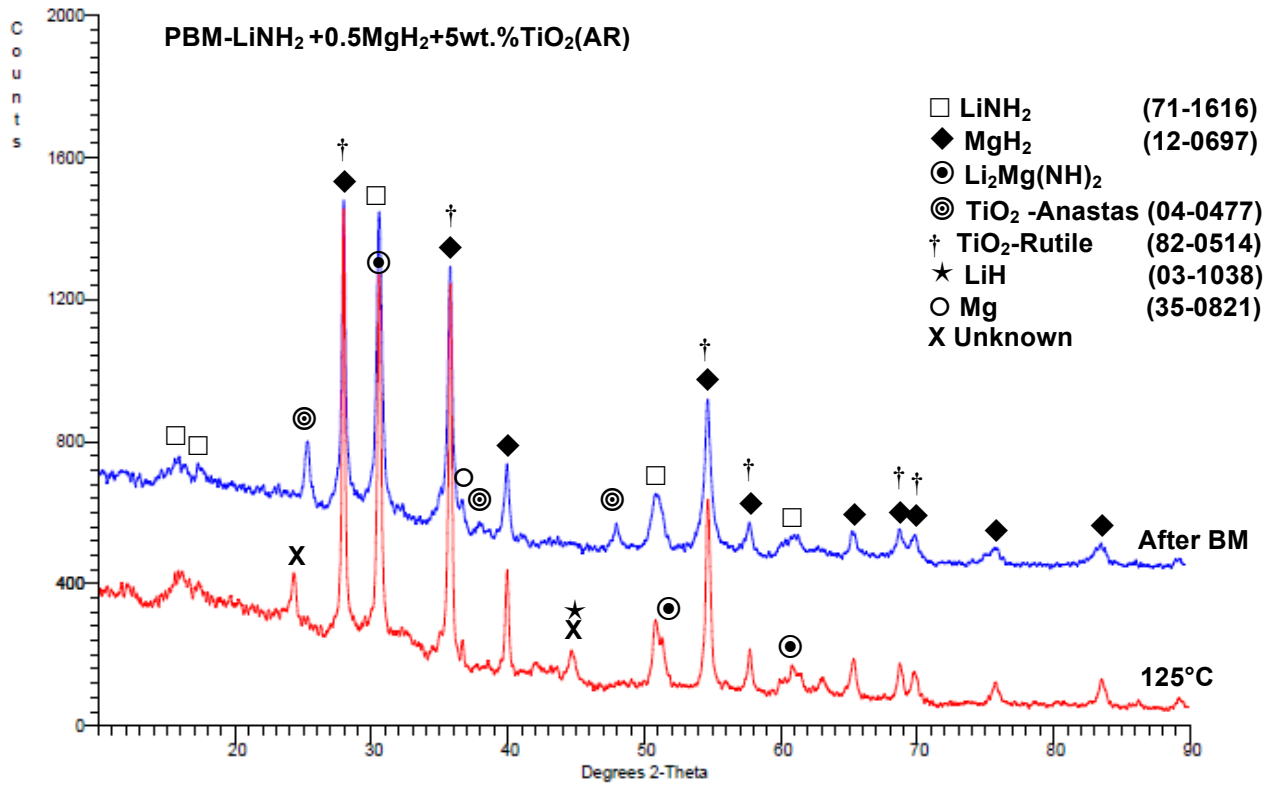

Fig. A.4. The XRD patterns after dehydrogenation at varying temperatures for (PBM($LiNH_2$+0.5MgH_2)+ 5 wt.% TiO_2) system. ICDD file numbers are shown for peak identification. Ball milled under LES6-4B- R132 15min milling mode.

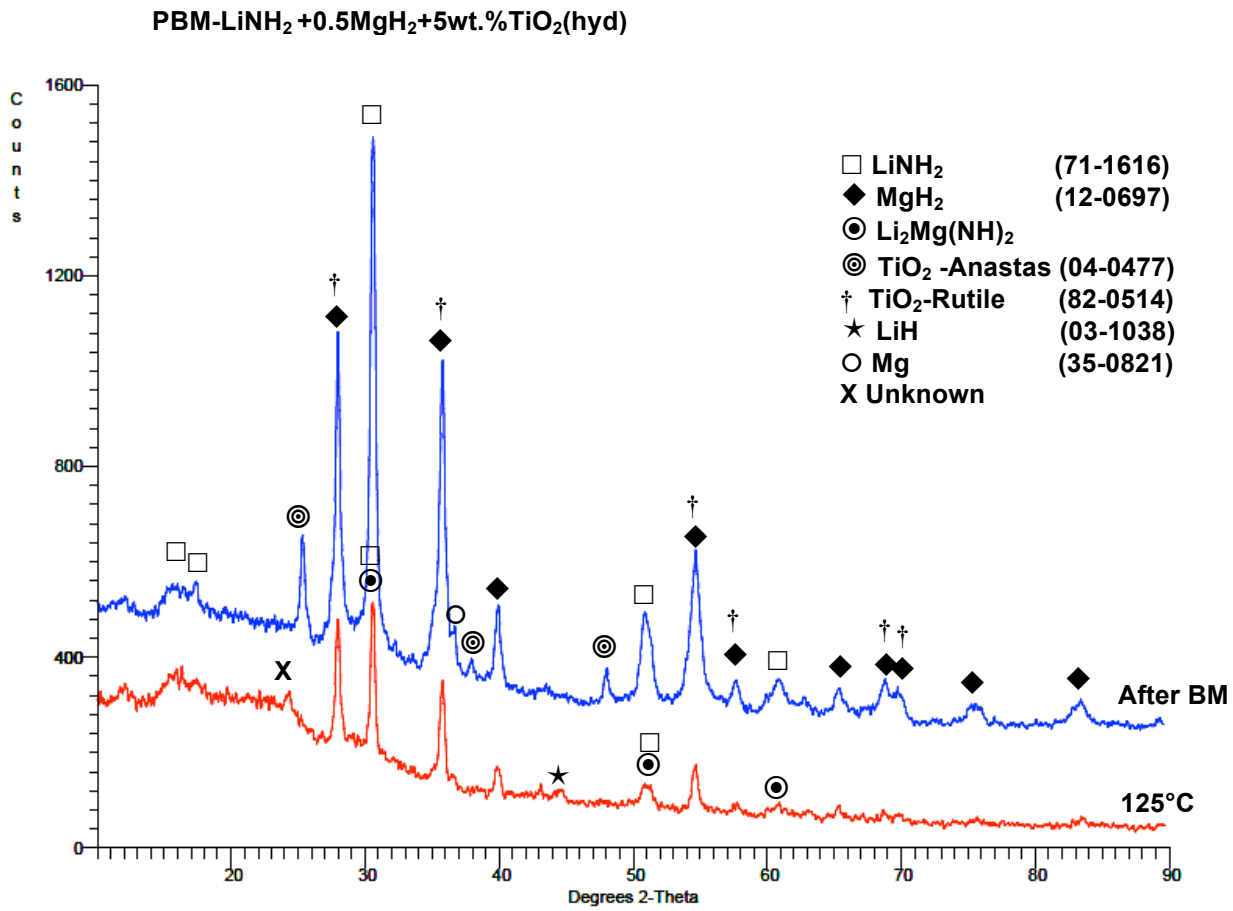

Fig. A.5. The XRD patterns after dehydrogenation at varying temperatures for (PBM($LiNH_2$+0.5MgH_2)+5 wt.% hydrogenated TiO_2) system. ICDD file numbers are shown for peak identification. Ball milled under LES6-4B- R132 15min milling mode.

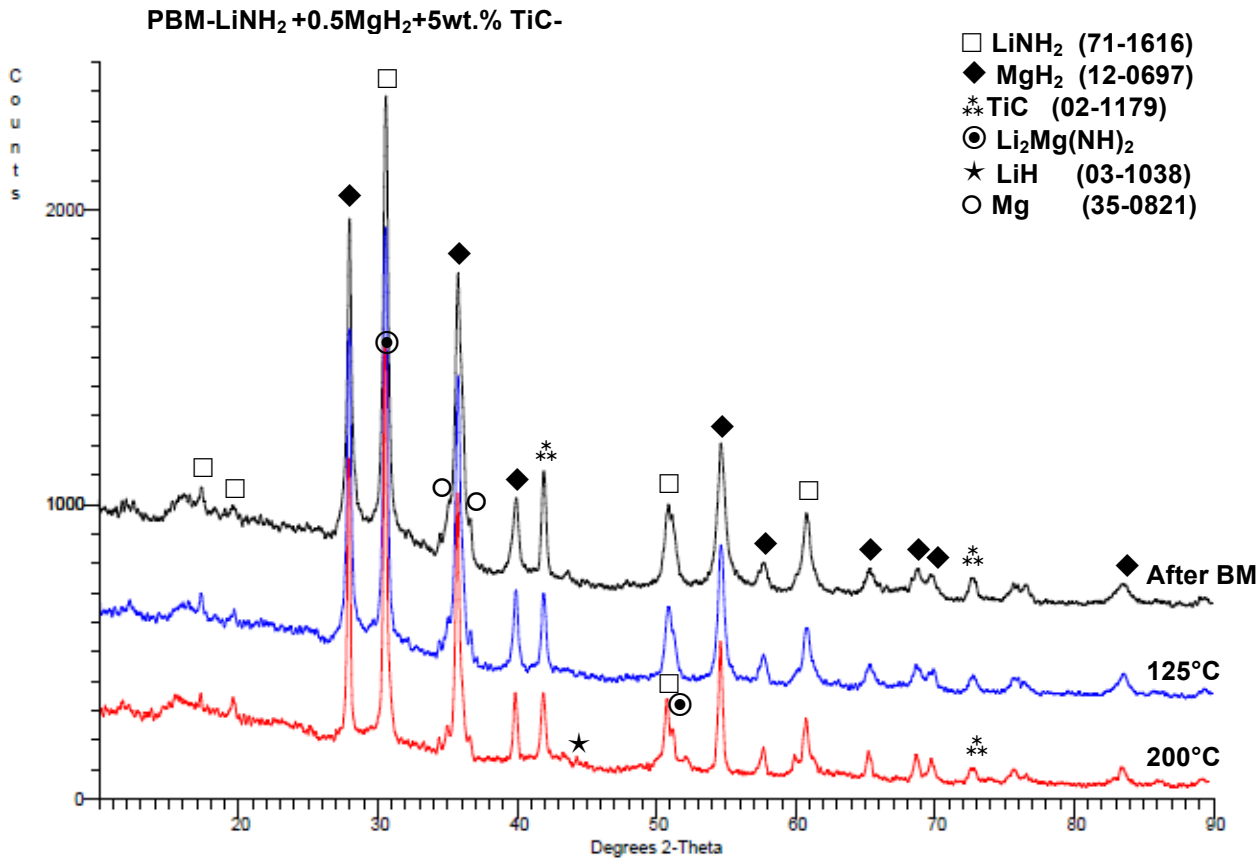

Fig. A.6. The XRD patterns after dehydrogenation at varying temperatures for (PBM($LiNH_2$+0.5MgH_2)+ 5 wt.% TiC) system. ICDD file numbers are shown for peak identification. Ball milled under LES6-4B- R132 15min milling mode.

List of Publications

- R.Parviz, R.A.Varin, Combined effects of molar ratio and ball milling energy on the phase transformations and mechanical dehydrogenation in the lithium amide-magnesium hydride ($LiNH_2$+$nMgH_2$)(n=0.5-2.0) nanocomposites, International Journal of Hydrogen Energy, 38 20 (2013) 8313-8327

- R.A.Varin, R.Parviz, Hydrogen generation from the ball milled composites of sodium and lithium borohydride ($NaBH_4$/$LiBH_4$) and magnesium hydroxide ($Mg(OH)_2$) without and with the nanometric nickel (Ni) additive, International Journal of Hydrogen Energy, 37 (2012) 1584-1593.

- R.Parviz, R,A.Varin, The effects of the micrometric and nanometric iron (Fe) additives on the mechanical and thermal dehydrogenation of lithium alanate (LiAlH4), its self-discharge at low temperatures and rehydrogenation, International Journal of Hydrogen Energy 37 (2012) 9088-9102.

- T.Leshuk, R.Parviz, P.Everett, H.Krishnakumar, R.A.Varin, F.Gu, Photocatalytic Activity of Hydrogenated TiO_2, ACS Appl. Mater. Interfaces, 56 (2013) 1892–1895

- R.A. Varin, R. Parviz, L. Zbroniec, Z. S. Wronski, Fundamental aspects of mechanical dehydrogenation of Li-based complex hydride nanocomposites and their self-discharge at low temperatures, Energy Procedia 2011.

- R.Parviz, R.A.Varin, Dehydrogenation of ball milled lithium alanate ($LiAlH_4$) catalyzed with nanometric TiC, TiN and ZrC as compared to nanometric nickel and iron catalyst, International Journal of hydrogen energy (submitted)

- R.Parviz, R.A.Varin, The effect of KH and NaH on dehydrogenation properties of $LiNH_2$, International Journal of hydrogen energy (submitted).